

Applications of Biogenic Silica Nanostructures from Diatoms

by

Kai-Chun Lin

A Dissertation Presented in Partial Fulfillment
of the Requirements for the Degree
Doctor of Philosophy

Approved November 2014 by the
Graduate Supervisory Committee:

B.L. Ramakrishna, Co-Chair
Michael Goryll, Co-Chair
Shalini Prasad
Sandwip Dey

ARIZONA STATE UNIVERSITY

December 2014

ABSTRACT

Biogenic silica nanostructures, derived from diatoms, possess highly ordered porous hierarchical nanostructures and afford flexibility in design in large part due to the availability of a great variety of shapes, sizes, and symmetries. These advantages have been exploited for study of transport phenomena of ions and molecules towards the goal of developing ultrasensitive and selective filters and biosensors. Diatom frustules give researchers many inspiration and ideas for the design and production of novel nanostructured materials. In this doctoral research will focus on the following three aspects of biogenic silica: 1) Using diatom frustule as protein sensor. 2) Using diatom nanostructures as template to fabricate nano metal materials. 3) Using diatom nanostructures to fabricate hybrid platform.

Nanoscale confinement biogenetic silica template-based electrical biosensor assay offers the user the ability to detect and quantify the biomolecules. Diatoms have been demonstrated as part of a sensor. The sensor works on the principle of electrochemical impedance spectroscopy. When specific protein biomarkers from a test sample bind to corresponding antibodies conjugated to the surface of the gold surface at the base of each nanowell, a perturbation of electrical double layer occurs resulting in a change in the impedance.

Diatoms are also a new source of inspiration for the design and fabrication of nanostructured materials. Template-directed deposition within cylindrical nanopores of a

porous membrane represents an attractive and reproducible approach for preparing metal nanopatterns or nanorods of a variety of aspect ratios. The nanopatterns fabricated from diatom have the potential of the metal-enhanced fluorescence to detect dye-conjugated molecules.

Another approach presents a platform integrating biogenic silica nanostructures with micromachined silicon substrates in a micro/nano hybrid device. In this study, one can take advantages of the unique properties of a marine diatom that exhibits nanopores on the order of 40 nm in diameter and a hierarchical structure. This device can be used to several applications, such as nano particles separation and detection. This platform is also a good substrate to study cell growth that one can observe the reaction of cell growing on the nanostructure of frustule.

DEDICATION

I dedicate this dissertation to my God and my family, especially...

to My wife, Tin-Kiong, for her patience and understanding;

to My Dad and Mom for the support, prayer, and encouragement;

to My daughter, Chloe and Natalie. I love you.

ACKNOWLEDGMENTS

Over the past eight years I have received support and encouragement from a great number of individuals. The completion of a doctorate is by no means a one can achieve alone. I must begin by thanking my advisor Dr. B. Ramakrishna for being a great mentor and professor. His guidance has made this a thoughtful and rewarding journey. Along with Dr. Ramakrishna, Dr. Michael Goryll also played a pivotal role in helping me grow into a PhD student. He has been a good mentor, colleague, and a good friend. I am also grateful for my dissertation committee members, Dr. Sandwip Dey, and Dr. Shalini Prasad, for their support over the past years. I must extend a special thanks to Dr. Kaushal Rege for providing his lab and resources for me, as well as his guidance and advice.

Most importantly I must thank my parents for supporting my education and always encouraging and praying for me. Without their support, I can't finish my degree. Also, I must thank Tin-Kiong, my wife, for her unconditional love and her endless support.

TABLE OF CONTENTS

| | Page |
|---|------|
| LIST OF TABLES..... | ix |
| LIST OF FIGURES..... | x |
| CHAPTER | |
| 1 INTRODUCTION | 1 |
| 1.1 Introduction To Diatoms | 1 |
| 1.1.1 Structure Of Diatoms..... | 3 |
| 1.1.2 Mechanical Properties Of Diatoms..... | 8 |
| 1.1.3 Chemical Properties Of Diatoms..... | 8 |
| 1.1.4 Diatom Culturing..... | 10 |
| 1.2 Potential Diatom Applications | 13 |
| 1.3 Aim Of This Dissertation | 15 |
| 1.3.1 Using Diatom Frustule As Protein Sensor..... | 16 |
| 1.3.2 Using Diatom Nanostructures As Template To Fabricate Metal Nanomaterials | 17 |
| 1.3.3 Using Diatom Nanostructures To Fabricate Hybrid Platform..... | 18 |
| 1.3.4 Using Concept Maps As A Tool To Teach Nano Science And Technology | 19 |
| 2 USING DIATOM NANOPORE AS PROTEIN SENSOR | 20 |
| 2.1 Introduction..... | 20 |
| 2.2 Configuration Of The Diatom-Based Sensor..... | 26 |
| 2.3 Electrical Impedance Spectroscopy | 28 |
| 2.4 Biosensor Surface Treatment..... | 30 |

| CHAPTER | Page |
|---|------|
| 2.5 Results And Discussion | 34 |
| 2.5.1 Antibody Saturation Isotherm | 34 |
| 2.5.2 Protein Dose Response From Pure And Serum Samples | 38 |
| 2.5.3 Selectivity Analysis | 42 |
| 2.6 Conclusion | 44 |
| | |
| 3 USING DIATOM NANOSTRUCTURES AS TEMPLATE TO FABRICATE METAL NANOMATERIALS | 46 |
| 3.1 Introduction | 46 |
| 3.2 Fabrication Nanostructures From Diatom..... | 47 |
| 3.2.1 Different Approaches From Other Group | 47 |
| 3.2.2 Electrochemical Deposition..... | 48 |
| 3.2.3 Materials And Methods | 50 |
| 3.2.4 Gold Nanorods/Nanopatterns From Diatom Frustules | 53 |
| 3.2.5 Gold Nanorods From Diatom Templates | 55 |
| 3.2.6 Conclusion | 58 |
| 3.3 Sputter Coating And Metal-Enhanced Fluorescence Application | 60 |
| 3.3.1 Metal-Enhanced Fluorescence..... | 61 |
| 3.3.2 Material And Method | 65 |
| 3.3.3 Results And Discussion | 67 |
| 3.4 Conclusion | 76 |
| | |
| 4 USING DIATOM NANOSTRUCTURES TO FABRICATE HYBRID PLATFORM..... | 77 |

| CHAPTER | Page |
|---|---------|
| 4.1 Introduction | 77 |
| 4.2 Materials And Methods..... | 79 |
| 4.2.1 Fabrication Of Silicon Chip..... | 79 |
| 4.2.2 Diatom Placement..... | 81 |
| 4.2.3 Electrical Characterization | 84 |
| 4.3 Results And Discussion..... | 85 |
| 4.3.1 Hybrid Platform Structure Characteristics | 85 |
| 4.3.2 Hybrid Platform Electrical Characterization | 87 |
| 4.4 Potential Applications | 90 |
| 4.4.1 Nanoparticle Selection Through Pores Of A Diatom | 90 |
| 4.4.2 Hybrid Silicon MEMS/Diatom Platform For The Cellular Response To Molecules..... | 95 |
| 4.5 Conclusion..... | 100 |
| 5 USING CONCEPT MAPS FOR INTEGRATING RESEARCH AND EDUCATION IN NANO SCIENCE AND TECHNOLOGY WITH GRAND CHALLENGES | 102 |
| 5.1 Introduction | 102 |
| 5.2 What Is Concept Map?..... | 102 |
| 5.3 Grand Challenges For Engineering..... | 105 |
| 5.4 Big Ideas In Nanoscale Science And Engineering..... | 106 |
| 5.5 Construct Grand Challenges Concept Map..... | 107 |
| 5.6 New Interface For Users To Retrieve Content From Maps | 114 |
| 5.7 Two Ways To Use Grand Challenge Nano Concept Map | 117 |

| CHAPTER | Page |
|----------------------|------|
| 5.8 Conclusion | 119 |
| REFERENCES..... | 120 |

LIST OF TABLES

| Table | Page |
|---|------|
| 1-1. Preparation Of 11 F/2 Medium With Following Components..... | 12 |
| 2-1. Comparison Of % Covalent And Ionic Character Of Al-O And Si-O Bonds..... | 24 |
| 4-1. Calculated Current Of Single Nanopore By Different Size At 400 mv..... | 93 |

LIST OF FIGURES

| Figure | Page |
|--|------|
| 1-1 Centric Diatom (Left Figure) And Pennate Diatom (Right Figure) | 3 |
| 1-2 Schematic Diagram Of A Centric Diatom Showing The Petri-Dish Like Nature Of The Frustule.[13]..... | 4 |
| 1-3 Diatom Structure..... | 6 |
| 1-4 Diatom Life Cycle..... | 7 |
| 1-5 Optical Microscope Image Of Coscinodiscus Wailesii, (A) Before Cleaning. (B) After Cleaning..... | 11 |
| 1-6 Diatom Culturing. | 12 |
| 1-7 (A) Schematic Model Of Frustule Pore Architecture For The Diatom Placed On The Gold Working Electrode, (B) Schematic Showing The Antibody–Antigen Binding Inside A Nanowell. | 16 |
| 2-1 Sem And Optical Images Of Electrode And Coscinodiscus Frustules On The Chip | 27 |
| 2-2 (A) Schematic Model Of Frustule Pore Architecture For The Diatom Placed On The Gold Working Electrode, (B) Schematic Showing The Antibody–Antigen Binding Inside A Nanowell. (C) Equivalent Circuit Of A Sensing Site..... | 28 |
| 2-3 Saturation Isotherm For The Two Antibodies On The Alumina And Diatom Substrates, Respectively. | 35 |
| 2-5 Dose Response Of The Two Proteins CRP And MPO..... | 40 |
| 2-6 Demonstration Of Selectivity In Detection Of The Protein CRP In Isotonic Buffer And In Human Serum Samples..... | 41 |

| Figure | Page |
|---|------|
| 3-1 Schematic For Fabrication Of Gold Nanostructures Using Diatom Frustules As Templates From Losic’s Group. | 47 |
| 3-2 The Preparation Of Metal-Coated Diatom Frustules And The Isolation Of Diatom- Templated Metallic Microshells From Payne’s Approach. | 48 |
| 3-3 Schematic Steps For The Synthesis Of Nano-Structures..... | 49 |
| 3-4 Left Panel Is Pennate Diatom; Nitzschia Frustulum And Right Panel Is Centric Diatom, Coscinodiscus Wailesii. Lower Column Is The Higher Magnification Images Of Nitzschia Frustulum And Coscinodiscus Wailesii..... | 50 |
| 3-5 The Serial Procedures For The Process Of The Electrochemical Deposition. | 51 |
| 3-6 Releasing Gold Nanorods From Diatom Template And Substrate..... | 52 |
| 3-7 The Sem Images Of Gold Nanostructures Fabricated By Electrochemical Deposition Using Nitzschia Frustulum Frustules As Template. | 53 |
| 3-8 The Sem Images Of Gold Nanostructures Fabricated By Electrodeposition Using Coscinodiscus Wailesii Frustules As Template..... | 54 |
| 3-9 The Sem Images Of Gold Nanorods Released From The Membrane Using Nitzschia Frustulum Frustules As Template..... | 55 |
| 3-10 The Histogram Of The Length And Diameter Of Gold Nano Rod Fabricated By Diatom-Templated Electrodeposition..... | 57 |
| 3-11 Edax Spectrum Of Gold Nanorods..... | 58 |
| 3-12 Classical Jablonski Diagram For The Free-Space Condition And The Modified Form In The Presence Of Metallic Particles, Islands Or Colloids..... | 63 |

| Figure | Page |
|---|------|
| 3-13 Schematic Illustration Of Fabrication Gold Nano Structures From Diatom Frustules..... | 66 |
| 3-14 Sem Images Of Diatom Frustule And Replica Nano Structures.. | 68 |
| 3-15 Sem Images Of The External Frustule Membrane Of <i>Coscinodiscus Sp.</i> Used As Template With Corresponding Gold Replicas..... | 69 |
| 3-16 Sem Images Of The Internal Frustule Membrane Of <i>Coscinodiscus Sp.</i> Used As Template With Corresponding Gold Replicas..... | 70 |
| 3-17 Afm Images Of Gold Structures Replicated From Cribrum Membrane With Profile Graph Showing The Height Of The Gold Nano Structures..... | 70 |
| 3-18 Fluorescence Image Of Alexa Fluor® 488 On Gold Replica From Diatom..... | 71 |
| 4-1 The Bisector Cross-Section (Top) And Top (Bottom) Views Of Near Aperture Part Of The Diatom Nanopore Membrane Device..... | 80 |
| 4-2 The Optical Micrograph Shows A Diatom Frustule Which Has Been Immobilized Using Poly-L-Lysine..... | 81 |
| 4-3 Cross-Sectional Scanning Electron Micrograph Of Micropore After Completion Of The Fabrication Sequence With A Diatom Frustule Mounted On Top Of It.. | 86 |
| 4-4 The I-V Curves Of A Hybrid Platform For Various Kcl Concentrations At 1 Mm, 10 Mm, 50 Mm, And 100 Mm..... | 88 |
| 4-5 Ion Current Recording Indicating Translocation Of 27 Nm Diameter Polystyrene Beads Through The Diatom Nanopore Membrane..... | 94 |

| Figure | Page |
|--|------|
| 4-6 Schematic Drawing (Bottom) Of The Nanoporous Layers Of A Diatom Frustule (<i>Coscinodiscus Wailesii</i>)..... | 96 |
| 4-7 The Silicon Chips With Diatom Mounted On The Micropore Were Placed At The Bottom Of Transwell. | 97 |
| 4-8 Cell Spreading On Silicon Chip And Diatom Frustules..... | 98 |
| 4-9 Schematic Of A Diatom Valve Pore Structure [130] | 99 |
| 5-1 An Example Of Hierarchically Structured Concept Map..... | 103 |
| 5-2 An Example Of Semantic Network Of Mind Map..... | 104 |
| 5-3 Concept Map Connection Between Grand Challenges And Big Ideas. | 108 |
| 5-4 Grand Challenge Nano Concept Maps | 109 |
| 5-5 Solar Energy Mind Map..... | 111 |
| 5-6 Clean Water Mind Map..... | 113 |
| 5-7 Adding Teaching Activities In The Map..... | 115 |
| 5-8 The Home Interface Of Grand Challenges | 116 |
| 5-9 Starting From Concepts To Grand Challenges And Interested Research Paper..... | 117 |
| 5-10 Starting From Interested Research Paper To Teaching Activities..... | 118 |

CHAPTER 1

INTRODUCTION

1.1 Introduction To Diatoms

Diatoms are eukaryotic, unicellular photosynthetic algae that are well known for the spectacular design of their silica-based cell walls [1-3], and ubiquitous presence in nearly every aquatic habitat on earth. Diatoms produce diverse three-dimensional, symmetric silica structures (called frustules) with pores from nanometer to micrometer dimensions. In addition, they also possess intricate geometries and spectacular patterns of their cell walls. These patterns are species-specific and are precisely reproduced during each cell division cycle. The number of the species is estimated to be over 100,000 and each of them has a unique frustule shape decorated with nanometer-sized pores [4, 5]. Diatoms are enormously important for the biological cycling of not only silicon but also carbon. Diatoms are responsible for approximately 25-30% of total photosynthetic CO₂ fixation [6]. The advantage of diatom for nanotechnology over standard photolithography methods is that diatoms grow exponentially in solution [7], which is faster than the manufacturing rate of MEMS. Diatoms can be grown to more than 10⁶ cells per milliliter of culture medium in a couple days at replication rates over many times a day and requiring only nutrients and light. For these reasons, cultivation of diatoms shows potential as the first step in the nanofabrication of complex functional structures.

Silicic acid (H₄SiO₄) is an important nutrient in the ocean, which is an essential chemical requirement for diatoms, radiolaria, and siliceous sponges. These organisms extract

dissolved silicate from ocean water to build up their silica (SiO₂) skeletal structures. Diatom cell wall is one of the most common siliceous structures observed of silica-secreting organisms. They are responsible for the majority of silica extraction from ocean waters and account about 43% of the primary production. The silica skeletal structure from diatom primarily serves as a mechanical and structural support, providing protection from predators and also acts as sensors. They usually exhibit hierarchical structures and pores over several length scales ranging from tens of nanometers to hundreds of micrometers. This unique structure is challenging to achieve in the lab by synthetic approaches. There are three different hierarchical structures have been found in diatoms: (1) microscale (of the order of the cell), (2) mesoscale (higher order assemblies of biosilica pores) and (3) nanoscale (primary particles and aggregates). [8]

Diatoms can make a three-dimensional micro- to nanoscale structure for them with no difficulties. By contrast, nanotechnology techniques, currently used in the semiconductor industry, are tedious to build up three-dimensional structures layer by layer. This presents an opportunity to use diatoms themselves as templates to make nanostructures as well as exploiting their unique properties.. For example, the regularly repeating micro and nanostructures in diatom cell walls lead to special optical photonic properties.

Diatom research gained tremendous momentum after the identification of silicon transporters in the late 1990s and early 2000s. Genomes of two diatom species have been sequenced, with several genes associated with biosilica synthesis in diatoms identified.

[9] In the last ten years, there have been many research publications on the potential nanotechnology applications of biologically inspired silica from diatoms[2, 10-12].

1.1.1 Structure of Diatoms

Diatoms are usually classified as one of two main groups: centric diatoms and pennate diatoms, depending upon the symmetry of their frustules (Fig. 1-1). Centric diatoms are radially symmetrical, while pennate diatoms tend to be elongated and have parallel groove on the surface.

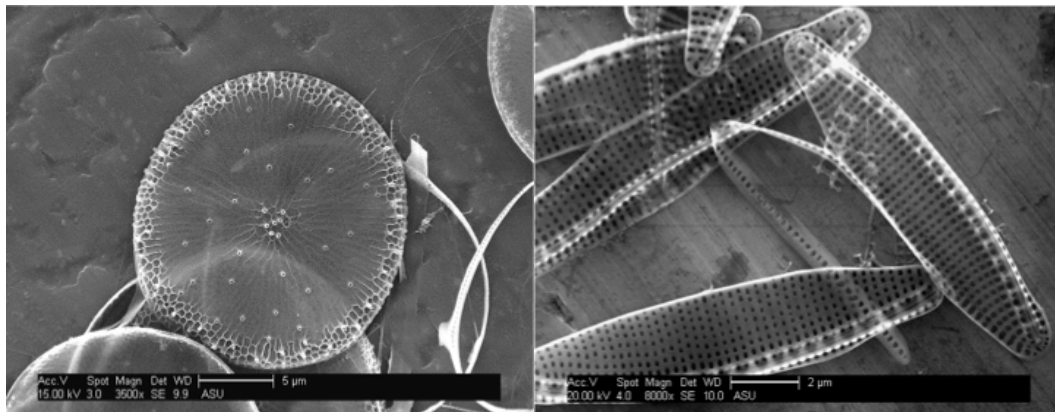


Figure 1-1 Centric diatom (left figure) and pennate diatom (right figure).

The centric type is of primary interest as having nanotechnology potential, due to its uniform pore structure, well-aligned pores, and a wide range of sizes from 20 – 250 µm. The diatom cell is enclosed in unique cell walls known as frustules. The centric diatom frustule contains two equal halves, and resembles a petri dish. Each half consists of a valve and a girdle. The valve forms the larger outer surface and the girdle is the circular band of silica attached to the edge of the valve (Fig. 1-2).

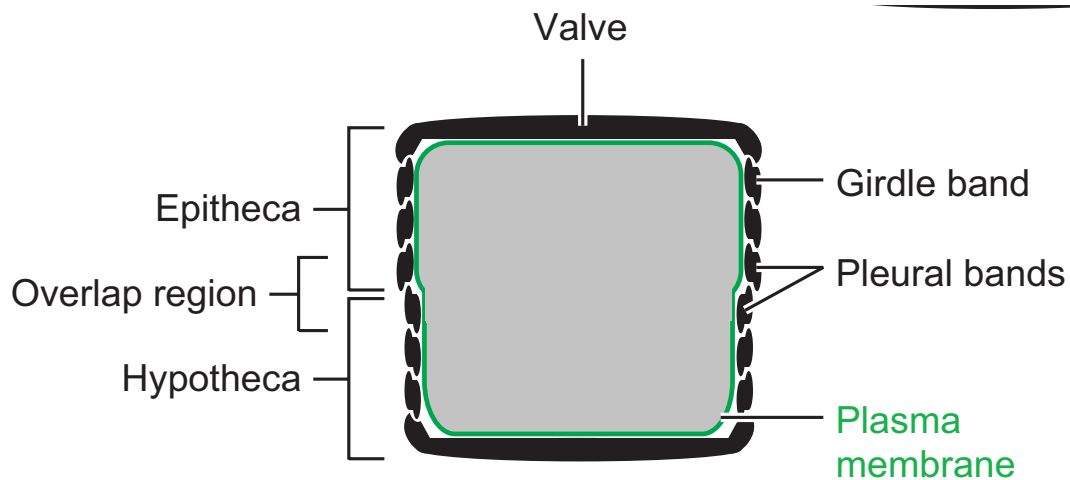


Figure 1-2 Schematic diagram of a centric diatom showing the petri-dish like nature of the frustule.[13]

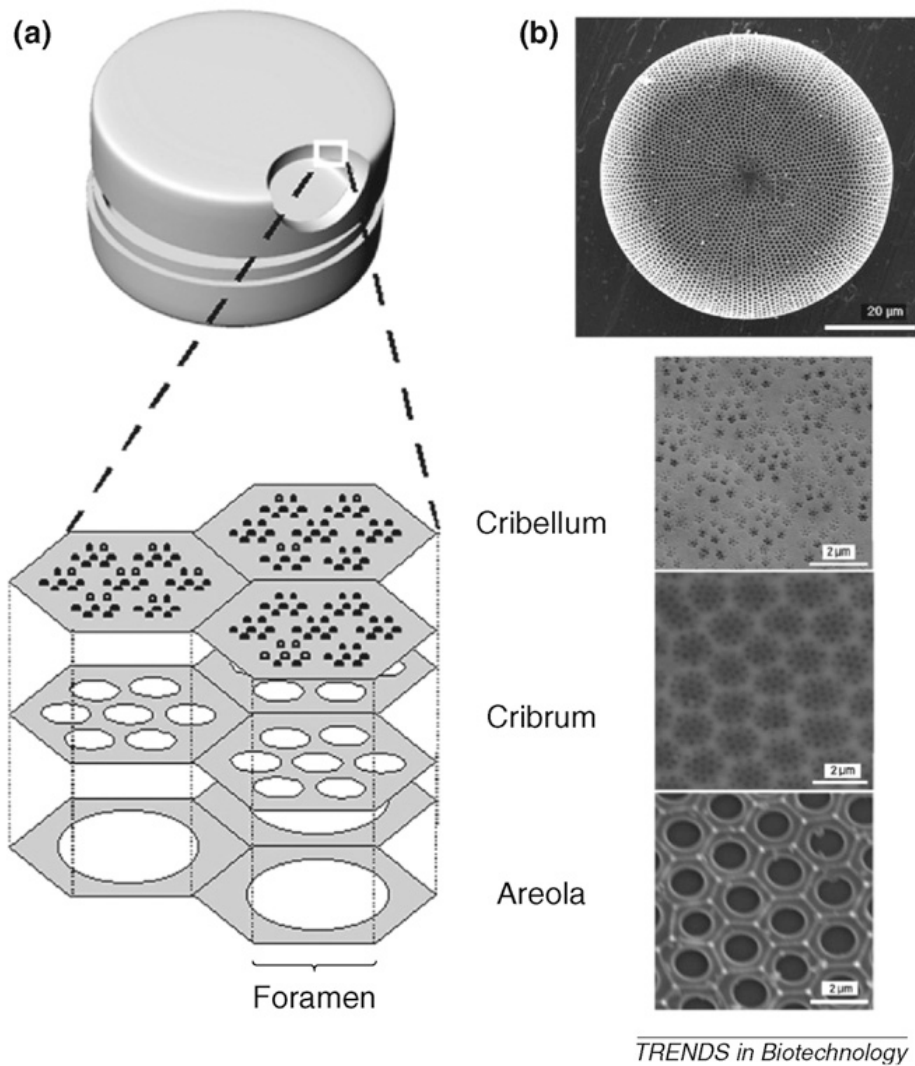
In most diatom species the construction of hypotheca and epitheca are identical. Both theca elements are siliceous and display the ornamental morphological features. In addition, the silicified cell walls are also associated with a range of organic coverings that function in a variety of ways, including protection from desilicification. [14] Each valve possesses three-dimensional (3D) and hierarchical structures of porous plates and solid walls. The pore diameters range from nanometres to micrometres (Fig. 1-3).

The pores from valves and girdle bands provide the channels for diatom to interact with their environment, and facilitate transport of nutrients and waste materials.

Possibly, the thick silica plate forming the biggest pore (areolar chambers) is responsible for the mechanical stability of the frustule whilst the comparatively thin membranes of 200 nm and 40 nm porous membrane have developed for filtration and separation. From Losic's group study, they have compared two different diatom species and investigated the size of the smallest pores (40 nm) is consistent. This consensus might imply that this

pore size is the species comprehensive size exclusion limit for separation of salubrious particles and molecules (<40 nm) and deleterious particles like virus and bacteria (>40 nm). [15]

The large voids or pores in a diatom frustule have a dielectric constant of nearly 1, thus the dielectric constant of the whole silica diatom frustule may be reduced from 3.9, which is the dielectric constant of silica. Introduction of porosity is inevitably related to a decrease in mechanical robustness during the manufacturing process. So diatom frustule, with a robust hierarchical porous nanostructure, may be a good material with a low dielectric constant as interlayer dielectrics for the on-chip interconnection of integration devices to provide high speed, and low cross-talk noise. One could choose larger diatom with two or three layers hierarchical nanoporous structure as interlayer dielectric for the interconnection membrane.



TRENDS in Biotechnology

Figure 1-3 Diatom structure. (a) Schematic of a centric diatom frustule with 3D profile of the silica wall. (b) SEM image of a *Coscinodiscus* sp. with corresponding layers [16].

The rigidity and architecture of silica cell wall force restrictions on the mechanism of cell division and growth. Vegetative reproduction (Fig. 1-4) (asexual) is the main mode of reproduction. As valves can only be formed during cell division and because new valves always develop within the parental cell wall, the sibling cell is usually smaller than the parental cell. As a consequence, the average cell size in a diatom population slowly decreases with continued vegetative growth and finally, the size reduction will result in

cells being too small and the diatoms would die. The other route is by sexual reproduction as shown in Fig. 1-4. The molecular details of this process are almost completely unexplored. Some species of diatoms (e.g., *Thalassiosira pseudonana*) growing in laboratory keep the size constant. The mechanism by which these species avoid size reduction is not yet fully understood.

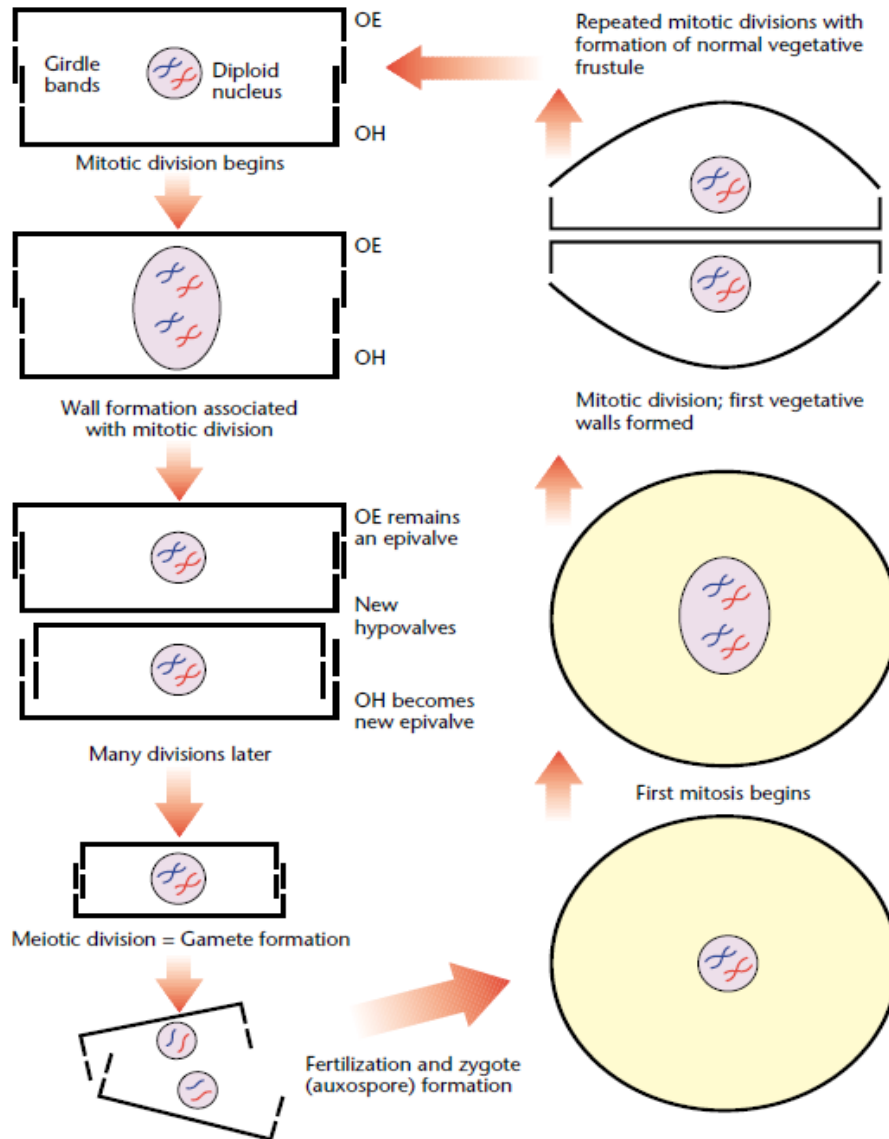


Figure 1-4 Diatom life cycle (OE: original ephivalve, OH: original hypovalve) [3]

1.1.2 Mechanical Properties of Diatoms

In the environment, diatoms are exposed to many mechanical challenges like abrasive particles and sediments. Diatom frustule valves and girdle bands form boxlike protection as a defense mechanism to safeguard plasma inside. The knowledge of mechanical properties and organization of diatoms will inspire the design and engineering of these lightweight structures on the macro- and nano- scale. [17] Hamm et al. studied the mechanical strength of diatom frustule by measuring the minimum force to break a single cell. [18] Mechanical stresses ranging from 150 to 680 N mm⁻¹ were tolerated depending on the region of the frustule. The mechanical stress values are similar to the materials of rubber and low-density polyethylene, where the values are ranging from 100 to 450 N mm⁻¹. The hardness, and elastic modulus have also been done in pennate and centric diatom by using AFM. [19] The hardness variation ranges from 0.03 GPa to 0.11 GPa, and elasticity ranges from 0.6 to 2.8 GPa across the frustule. This is similar to the hardness and elastic modulus found in porous silicon with similar pore size. [20] Another materials having similar value of hardness and elastic modulus are polypropylene and polyethylene terephthalate.[21]

1.1.3 Chemical Properties of Diatoms

The density ranges of diatom are between 1.03 to 1.26 g/cm³ depending on different species. [22] There are many components in diatom cell, including proteins, carbohydrates, nucleic acids, lipids, and SiO₂.

| Component | Density (g/cm ³) |
|------------------|------------------------------|
| Proteins | ~1.3 |
| Carbohydrates | ~1.5 |
| Nucleic acids | ~1.7 |
| SiO ₂ | ~2.6 |
| Lipids | ~0.86 |

After removing all the organic parts from diatom frustule, only silica nanostructures were left. The density of clean diatom frustule should be around 2.6 g/cm³. One group using FTIR spectra to study diatom frustule had observed that the hydrogen atoms are essentially bonded in Si–H configurations and the absorption band of the H–O–Si bonds is usually negligible [23]. It suggests that oxygen-deficient amorphous-silica (a-SiO_x:H) in diatom frustule which may cause the density of diatom frustule lower than 2.6 g/cm³. The XPS spectrum of diatom frustule also shows binding energy peak of Si 2p of SiO₂ is at around 102.5 to 103 eV [24], which indicates the value X of SiO_x would be between 1.24 to 1.78.

The chemical nature of diatom frustule is very similar to hydrated glass: SiO₂ nH₂O, where have free hydroxyl groups on the surface. These reactive groups allow chemical modification of the surface and subsequent functionalization with relative ease. The rich chemistry that can be conducted on the silica structure of the diatom frustule provides huge potential for their application as biosensors.

In order to immobilize a biological sensing element, like antibody or DNA, there are two basic approaches to bind biomolecules onto a surface using the ability of silanes to self-

assemble on silica surfaces: (1) Electrostatic binding. (2) Direct covalent attachment. The first approach is the most common non-covalent method to immobilize biomolecules on the surface. It is simple and depends on the charge distribution of the biomolecules. However, as it also depends on the ionic strength and pH of the solution, changes in ionic strength and pH value can cause the molecules to be released from the surface. The second approach is using direct covalent attachment, which has the greatest potential for the biosensors due to the stability of the covalent bond. The silanes are tightly bound through covalent bonds with the surface.. In addition, silanes are good chelating ligands due to their reactivity with hydroxyls, and can couple organic groups to label diatom frustules with biomaterials.

1.1.4 Diatom Culturing

Two types of diatoms were chosen, the first one is pennate diatom, *Nitzschia frustulum* and the second is centric diatom, *Coscinodiscus wailesii*. The main feature of *Nitzschia frustulum* is that it has periodically organized pores with an average diameter of about 100 nm, which can be used as template to fabricate nanorods and nanopatterns. The features of *Coscinodiscus wailesii* are that it is one of the largest diatom species with diameters 100 to 250 microns, and the pores size of *Coscinodiscus sp.* from the external membrane is around 40nm, which can also be used as template to fabricate nanopatterns. In addition, the diatom frustule can completely cover the gold electrodes of the biosensor that will be used in the chapter 2. The diatom species *Coscinodiscus wailesii* (fig. 1-5a), *Nitzschia frustulum*, and the f/2 medium to enrich the seawater were ordered from the

National Center for Marine Algae and Microbiota (NCMA). The diatoms were cultured in f/2 seawater medium at 20 C under continuous photoperiod in a sterile environment. The diatoms were cleaned by the addition of 50% (v/v) hydrogen peroxide (30% solution) and incubation at 90 C for 1–2 h to remove organic materials (Fig. 1-5b). Samples were centrifuged at 3000 rpm for 5 min, and washed several times with double deionized (18 MΩ*cm) water, and stored in 70% ethanol solution. These treatments cause the diatom frustule to be separated into two frustule valves and a girdle band. The frustule valves were separated from the girdle band and small debris using the settling method [25].

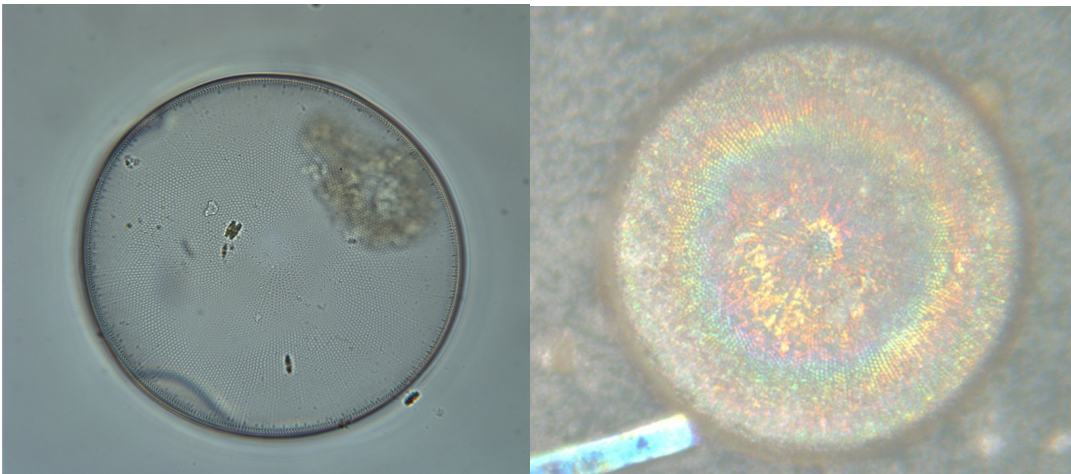


Figure 1-5 Optical microscope image of *Coscinodiscus wailesii*, (a) before cleaning. (b) after cleaning

1.1.4.1 Prepare F/2 Medium

1. Using 600mL flask and add 600ul of NaNO_3 , NaH_2PO_4 , Na_2SiO_3 , Trace metal solution and 300ul of Vitamin into 600mL seawater. (Kit purchased from NCMA: <https://ncma.bigelow.org/mkf250l#.U7H1cBbO9g0>)
2. After adding these stock solutions, shake the flask and mix well.
3. Add appropriate amount medium into diatom culture.
 - 3.1. Add about 1/3 new medium into original diatom culture. Ex: there is 300ml original diatom medium, add ~100ml new medium into it.
 - 3.2. If the original diatom medium is almost full of the flask, one is to divide it into two flasks, another way is to discard the old medium, keep the diatom sit at the bottom. (Turning off light, let the diatom precipitated at the bottom (about 3~4 hours), then gently pour out the upper medium)
4. Change the medium once a week, make sure diatoms is still growing. (Figure 1-6)
5. Shake the diatom every one or two days. Give them quantity CO_2 dissolved in the water.

Table 1-1: Preparation of 1L F/2 medium with following components.

| | |
|---|--------|
| NaNO_3 (75.0 g/L dH_2O) | 1.0 ml |
| $\text{NaH}_2\text{PO}_4 \cdot \text{H}_2\text{O}$ (5.0 g/L dH_2O) | 1.0 ml |
| $\text{Na}_2\text{SiO}_3 \cdot 9\text{H}_2\text{O}$ (30.0 g/L dH_2O) | 1.0 ml |
| f/2 Trace Metal Solution | 1.0 ml |
| f/2 Vitamin Solution | 0.5 ml |
| Filtered seawater to | 1.0 L |

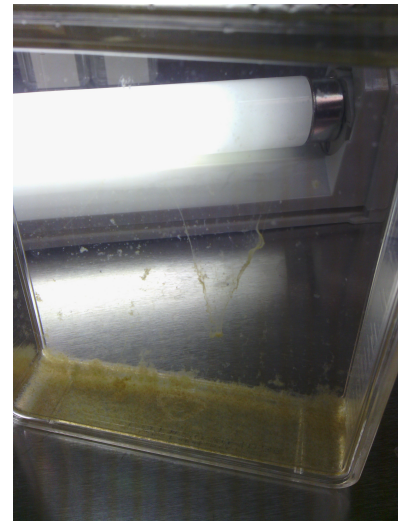


Figure 1-6 Diatom culturing.

1.2 Potential Diatom Applications

Diatom frustules give researchers many inspiration and ideas for the design and production of novel nanostructured materials. There are many reviews recently on diatom molecular biology, [8] and biotechnology. [26] Various applications have been suggested, including using diatom membranes for biomolecule separations [15], size-selective biosensors, microelectromechanical systems (MEMS), and masks for micro- and nano- fabrication [27].

The following four are potential applications that take advantage of the unique properties of biogenic silica.

Protein sensors: Detection of protein markers has been identified as a diagnosis mechanism to provide information of a disease.[28] The enzyme linked immunosorbent assay (ELISA) is the standard for clinical diagnosis, however, the sensitivity is about 3 picogram/ml [29], which requires large sample volume and further restricts in the application of testing sample from infants. The advent of nanotechnology in the field of clinical diagnostics can increase the sensitivity with many new approaches such as surface plasmon resonance (SPR) and electroanalysis that have been developed and applied for the selective detection of different biomarkers. The silica frustules of diatoms functionalized with antibody have also been employed as a biosensor to detect antibody–antigen reactions [30-32]. The major classes of nanomaterials that have been used for protein biomarker detection are: nanotubes, nanowires, nanoparticles and nanotemplates

[33]. The main advantage of these materials is their high surface to volume ratio with enhanced sensitivity and reduced use of reagents. Biogenic silica materials can play a critical role as nanotemplates due to the (i) high surface area to volume ratio, 200 m²/g for fresh diatom shells [34] and (ii) the unique hierarchical structures and properties.

Fabrication of metal nanostructures: Fabrication of nanostructured materials is an emerging area of current research.[35] The development of sensing devices using localized surface plasmon resonance (SPR) exhibited by nanopatterned gold structures has been especially attractive[36]. The nanoscale structures made of gold and other noble metals also offer great potential for application in optoelectronics, chemosensing, biosensing, and catalysis [37-39]. However, the technological advancements will be limited by the ability to synthesize and fabricate such structures on the nanoscale. The potential of using biological scaffolds to fabricate novel types of nanostructures is being investigated. [40-42] Biogenic silica materials offer a novel route for the design and fabrication of nanostructured materials.

Membrane to separate nanoparticles: Nanopore membranes are highly interesting for particles separation[43], molecules detection and DNA translocation studies[44-46]. Nanopore membranes with high porosity also provide the advantage of a high fluid throughput[47, 48]. However, as many of these high fluid throughput nanopore membranes are very thin with dimensions around 50nm, they suffer from being mechanically fragile and hence not ideal for several applications. Biogenic silica materials with their highly ordered porous hierarchical nanostructures can be thin without

compromising the mechanical stability[27]. Thin nanopore membranes with short pores of a length of around 50 nm offer an advantage with respect to temporal and spatial resolution of particle and molecule translocation[49, 50].

Platform for cell culture: The nanostructure of diatom frustule is a good substrate to study cell growth and response. The effect of microstructured surfaces on cell behavior has long been recognized, and it has recently been shown that cells can react to nanoscale structures as small as 10 nm. However, little is known regarding cell responses to nano-patterned surfaces. The topographical surface of diatom frustule could provide a biomimetic cell-stimulating substrate. One can observe the reaction of cell growing on the nanostructure of frustule. Cell may be stimulated by the nanostructure and attach on the rough nano-surface. Chemicals or drugs can treat a single cell from the other side of the diatom membrane due to the fast diffusion rate to observe the reaction and communication around the stimulated cell. This is a good platform to study cell-cell communication[51-53].

1.3 Aim Of This Dissertation

The dissertation will focus on the following three aspects of biogenic silica and additionally include a chapter on using concept maps as a learning tool for nano science and technology.

1. Using diatom frustule as protein sensor
2. Using diatom nanostructures as template to fabricate metal materials

3. Using diatom nanostructures as transport membranes and to fabricate hybrid platform

1.3.1 Using Diatom Frustule As Protein Sensor

The goal of this research is to demonstrate the possibility of using nanoporous biogenic silica as a key component in developing a biosensor platform for rapid label-free electrochemical detection. The biosensor platform consists of a silicon chip with an array of gold electrodes, and each sensor electrode is overlaid with a nanoporous biogenic diatom frustule, that forms numerous nanowells on top of each electrode (figure 1-7). The sensor works on the principle of electrochemical impedance spectroscopy.[28] When specific protein biomarkers from a test sample bind to corresponding antibodies conjugated to the surface of the gold surface at the base of each nanowell, a perturbation of electrical double layer occurs resulting in a change in the impedance. The nanoporous silica structure of diatom frustule would mimic the multi well architecture of an ELISA plate [54].

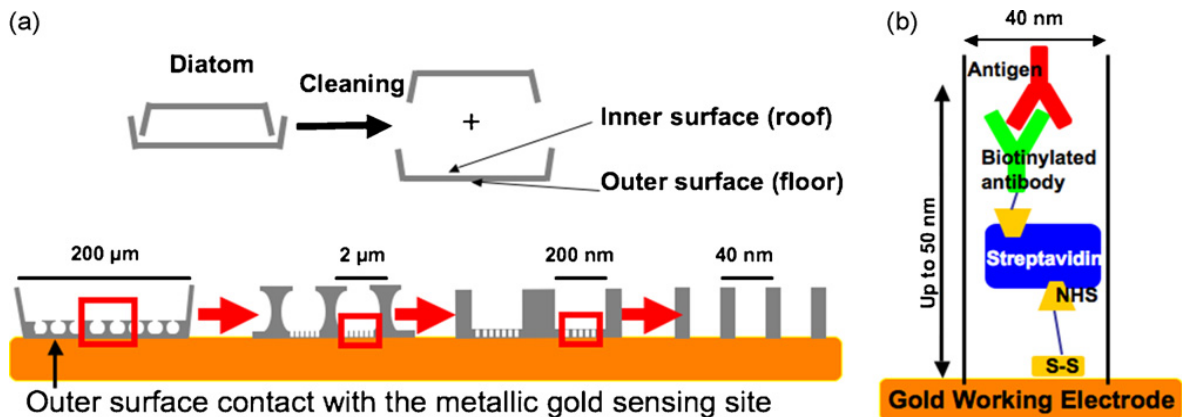


Figure 1-7 (a) Schematic model of frustule pore architecture for the diatom placed on the gold working electrode, (b) schematic showing the antibody-antigen binding inside a nanowell.

1.3.2 Using Diatom Nanostructures As Template To Fabricate Metal Nanomaterials

The one- and two-dimensional arrays of patterned nanostructures, like nanoparticles, nanowires, nanotube, etc, have some unique optoelectronic, magnetic, or catalytic properties that can be adjusted by varying their size or separation distance [55]. The patterned gold nanoparticles have photonic properties and can be used in the detection system of surface enhanced Raman scattering with high sensitivities [56]. The development of effective patterning methods to control materials assembly on a nanometer scale is an important technological challenge. At present, there are several of top-down fabrication techniques, which offer a wide range of structures of high quality, but are generally neither cost- nor time-effective, and for some methods, resolution below the 100 nm range is not easily achievable [55]. Diatoms are a quite new source of inspiration for the design and fabrication of nanostructured materials. In this section, the use of diatom frustules as templates for the fabrication of nano-patterned metal nanostructures will be demonstrated. Template-directed deposition within cylindrical nanopores of a porous membrane represents an attractive and reproducible approach for preparing metal nanowires of a variety of aspect ratios (with diameters of 10– 300 nm and lengths of 50– 1000 nm) [57]. Two methods to fabricate nanostructures will be demonstrated from diatom frustules: electrochemical deposition and sputter deposition, and explore the potential of the metal-enhanced fluorescence to detect dye conjugated molecules.

1.3.3 Using Diatom Nanostructures To Fabricate Hybrid Platform

This section presents an approach towards integrating biogenic silica nanostructures with micromachined silicon substrates in a micro/nano hybrid device. Solid-state nanopore membranes with nanopore diameters ranging from tens to hundreds of nanometers are of significant interest for particle separation [58], cell-cell communication [52, 59, 60], molecule [61-63] and DNA translocation studies [64-67]. However, they are usually patterned by electron-beam lithography to accomplish pore diameters of 20-300 nm [68]. Other ultrathin silicon membranes (~10 nm) with 25 nm diameter pores that employ an ion-beam drilling process are well suited for molecule separation applications, but the manufacturing process is too slow to allow easy scale up [69]. The details of a microfabrication process flow will be presented for producing a hybrid planar micromachined system, which consists of a biomineralized silica nanopore membrane combined with a single micropore through a silicon wafer. Silicon provides an ideal substrate because micropores can be precisely manufactured using photolithography and deep reactive ion etching and integrated with microfluids and microelectronics. The frustules, while being mechanically stable by themselves, need to be supported by an underlying substrate that provides the interface to the microfluidic system. This device can be used for several applications, such as nano particles separation and detection. This platform is also a good substrate to study cell growth that one can observe the reaction of cell growing on the nanostructure of frustule.

1.3.4 Using Concept Maps As A Tool To Teach Nano Science And Technology

Nano science and technology have attracted interests not only from scientists/engineers but also from the general public. A concept map is a good tool of representing relationships between ideas, concepts, images, and words. For example, a road map represents the locations of highways and towns, and a circuit diagram represents the workings of an electrical appliance. The goal of this part is to provide a practical method to connect the real world problems to the nano research. Concept mapping has been shown to help students learn, teachers to better design and structure lessons, and researchers create new knowledge. One can use this tool to design lessons, and inspire students to think of the new solution for the grand challenges.

CHAPTER 2

USING DIATOM NANOPORE AS PROTEIN SENSOR

2.1 Introduction

Proteomics research has resulted in the identification of a number of biomarker proteins, which have the potential to greatly improve disease diagnosis [70-73]. Detection of multiple biomarkers has been identified as a diagnostic mechanism to provide the information necessary for robust diagnosis of a disease in any person within a population [74-76]. Widespread use of protein biomarkers in healthcare will ultimately depend upon the development of techniques that allow rapid and multiplexed detection of a wide range of biomarkers with high selectivity and sensitivity.

The enzyme linked immunosorbent assay (ELISA), a fluorescent optical detection method, is the “gold standard” for clinical diagnostics with sensitivity down to about 3 picogram/ml (pg/ml) [77]. ELISA is a well-established technology that is safe, inexpensive, and high throughput as there is no need of radioactivity. Before the development of the ELISA, the only option to conduct immunoassay is radioimmunoassay that is using radioactively labeled antigens or antibodies. However, ELISA can suffer from high background and also be limited in ability to detect low-affinity antibodies. It also needs comparably large amount of reagents and the long incubation time for reach of the multiple steps.

Electrical detection of protein biomarkers is a relatively new approach that monitors a specific electrical parameter that undergoes change during the protein detection event.

The impact of nanotechnology on the field of clinical diagnostics has resulted in the

incorporation of nanoscale materials in designing diagnostics assays. The major classes of nanomaterials that have been used for protein biomarker detection are: nanotubes, nanowires, nanoparticles and nanotemplates [33, 78]. Often these materials have been utilized for their improved surface area towards developing detectors with enhanced sensitivity and reduced use of reagents. The use of carbon nanotubes for cancer protein biomarker detection has been demonstrated (Kam et al. 2005). Electrochemical conductance technique has yielded sensitivity in the range of lower nanogram/ml (ng/ml) to a few hundred pg/ml [79]. Implementation of the field effect transistor based transconductance technique using silicon nanowires has made it possible to detect proteins with sensitivity in the range of picogram/ml- femtogram/ml [80]. The use of antibody-coated nanoparticles as electrical biosensors operating on electrochemical conductance technique has also resulted in sensitivities in the pg/ml range [79]. The use of silicon nanoporous templates for protein detection has been demonstrated with sensitivity in pg/ml [54]. In all the nanomaterial-based electrical protein biosensors, detection response is on the order of minutes with very low sample volume, typically on the order of nanoliters.

While, each of these nanomaterial-enabled proteomic biosensors have demonstrated impressive performance metrics, there is a paucity of rigorous studies to benchmark these new technologies against the standard clinical diagnostics assay-ELISA, where detection occurs in a multiwell microtiter plate. Among the four nanomaterial classes mentioned above, nanotemplates can be most easily configured to generate a proteomic assay similar in geometrical configuration to the ELISA assay and this has led to the design of nanotemplate-based electrical biosensor assays [28]. It was expected that by generating

such an assay one would be able to benchmark the biosensor performance with respect to ELISA, enabling a quicker penetration into the domain of portable diagnostics assays.

Bothara et al. [54] have proposed a biosensor assay architecture utilizing nanoporous alumina membranes that mimics the multi well architecture of an ELISA plate. It comprises of a base microelectrode array with multiple metallic microscale measurement sites/electrodes. A nanoporous alumina membrane is overlaid onto the base microelectrode generating a high-density array of nanoscale voids- also known as nanowells, on a single metallic sensing site. Each nanowell functions in a similar manner as that of a well in ELISA plates with the detected proteins bound to the base of the well. There are three key differences between the nanomonitor nanowells and the micro wells of ELISA. First, protein detection is achieved by measuring the perturbation to the electrical double layer in the nanowells resulting in an electrochemical impedance change due to the protein-binding event, whereas in the micro wells quantification of fluorescence is a measure of the protein-binding event. Second, the measured electrical signal due to the electrical double layer perturbation is cumulative of the signals generated from an array of nanowells on a single microscale sensing site, whereas in the case of microwells in ELISA, the complete well is interrogated and quantified. Third, protein binding and detection is achieved through measuring single interactions between the primary antibody and the protein (antigen) in the nanowells, where as in the micro well proteomic assay there are two capture steps associated with the protein detection. The first step is the capture of the protein by the immobilized primary antibody and the second capture step binds the secondary antibody tagged with the flurophore to the

primary antibody-antigen complex. These three key differences between the ELISA and nanowell biosensor assays lead to (a) improved antigen-antibody association by increasing the antibody capture density within the nanowells, (b) enhanced detected signal strength due to signal accumulation from arrays of nanowells and (c) reduced the assay time due to protein detection through single capture step.

Nanoporous alumina membrane has been employed for the detection of penicillin up to 0.1 ng/ml through electrochemical conductance measurement [81]. The nanoporous alumina membranes have been used [54] for building the electrical immunoassay-based biosensor due to the following reasons: (a) the capacitance leakage between individual nanopores was eliminated because alumina is a good electrical insulator (b) interference from electrical noise due to the thermal shielding was reduced and (c) biocompatibility of the material in electrical biosensing. Despite these advantages, the manufactured nanoporous alumina membranes have a number of limitations, which can significantly impact the biosensor performance. They are (a) absence of simple chemistries to achieve surface functionalization of the surface of the nanopores in the nanoporous alumina membrane, making it difficult to improve the detection sensitivity and (b) absence of simple chemistries to adhere the alumina onto the sensing site, which is essential to minimize background noise signals.

In the current work illustrates the design and fabrication of a biosensor using biogenic silica from diatoms as the nanoporous template, which has been heterogeneously integrated on to the microelectrode platform. Though alumina and silica surfaces appear

to be somewhat similar, there are significant differences, namely, (a) Si-O bond is much more covalent than the Al-O bond (50% covalent character in silica vs. 35% in alumina) (Table 2-1), and therefore, substitution reactions are more facile in silica (b) alumina surface is not as stable at pH below 8 and there are surface charges caused by lattice defects [82] and (c) surface hydroxyl groups of hydrated alumina are less acidic than those on silica surface because, the isoelectric point of alumina, which is an indication of the ionization of the surface hydroxyl groups $Al-OH \rightleftharpoons AlO^- + H^+$, is attained at pH 9, while that for silica the isoelectric point is reached at pH 2 [83].

Table 2-1 Comparison of % Covalent and Ionic character of Al-O and Si-O bonds

| Ceramic Compound | % Covalent character | % Ionic character |
|------------------|----------------------|-------------------|
| Aluminum Oxide | 35% | 65% |
| Silicon Dioxide | 50% | 50% |

Diatoms offer an alternative approach to engineering nanoscale systems because of the ability to design materials that are inspired by or adapted from biologically produced nanostructures. These biogenic silica nanostructures derived from diatoms possess several unique properties [27] including, 1) Highly ordered porous hierarchical nanostructures. Such a highly ramified network of micro and nanopores enhances diffusion of nutrients and facilitates “molecular traffic control”, which is vital for optimum performance. 2) The ability to undergo a variety of surface modifications through well-established chemistries that allow easy tethering of biomolecules [84]. 3) Flexibility of design through the availability of a variety of shapes, sizes, and symmetries, from more than a hundred of thousand species of diatoms. The micro- and nanoscale

hierarchical pore structures offer the potential for confinement enhancements in sensitivity. The large surface area ($>200\text{m}^2/\text{g}$ for fresh diatom shells) also makes them a promising platform for sensors in general and biosensors in particular. 4) Finally, these silica-based templates also offer the advantage of easier integration with conventional well-established processing methods in the semiconductor industry.

The potential of diatoms as biosensors has been shown previously. For example, photoluminescence generated by the biogenic silica frustules of diatoms has been employed as the physical transducing effect to detect the biomolecular interaction of complementary DNA chains, [31] and antibody-antigens [30]. However, all of the studies so far have only employed optical detection schemes.

It is believed that the present work is the first reported study of using diatoms as part of a sensor configuration that employs changes in electrical properties to selectively and quantitatively detects antibody-antigen interactions. The performance of this multi scale assay as a biosensor has been demonstrated by detecting two inflammatory proteins; C-reactive protein (CRP) and Myeloperoxidase (MPO), which have been identified to be biomarkers of vulnerable coronary vascular plaque rupture [85, 86]. The use of diatoms significantly enhances the sensitivity as compared to nanoporous alumina membranes. The improved detection sensitivity and specificity as compared to the detection of these two protein biomarkers in alumina membranes and the detection performance is shown to be comparable to an ELISA assay.

2.2 Configuration Of The Diatom-Based Sensor

The diatom species *Coscinodiscus wailesii* was chosen because it is one of the largest diatom species with diameters 100 to 250 microns. In addition, the diatom frustule can completely cover the gold electrodes (fig. 2-1a). The siliceous cell wall has a honeycomb structure consisting of the vertical chambers arranged in hexagonal symmetry with porous plates forming the floor and the roof of the honeycomb (fig. 2-1b). In this particular diatom species, the outer surface (floor) of the plate, which is in touch with external environment (fig. 2-2a), is perforated by highly symmetric nanoscale pores, whereas the internal surface (roof) of the plate, which is in contact with the algal cell, exhibits a single microscale pore in the center of each honeycomb. The microelectrode chips comprising of metallic gold sensing sites were first coated with polylysine by treatment with 0.01% aqueous solution of polylysine. In order to place a diatom frustule on the electrode, one drop of cleaned diatom frustule suspension was deposited on the polylysine-coated chips (fig. 2-1c, 2-1d). Micromanipulation and attachment of an individual diatom frustule onto the electrode was performed using KRN-09 Positioner (J MicroTechnology, USA).

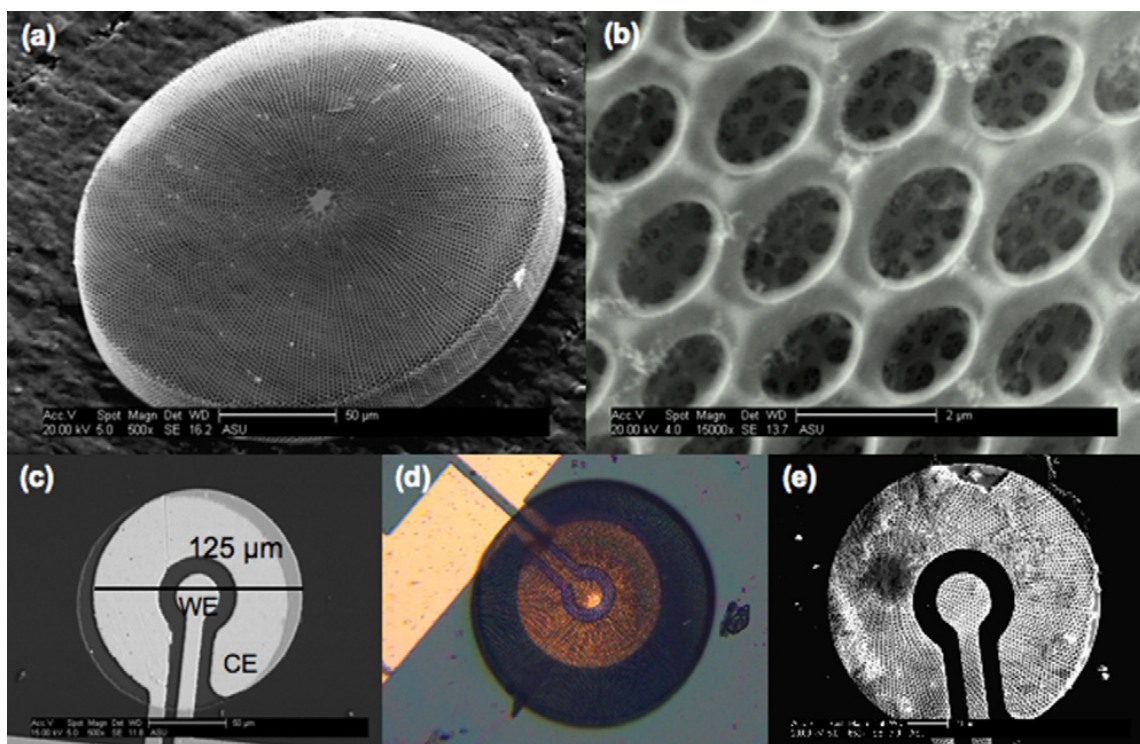


Figure 2-1 SEM and optical images of electrode and Coscinodiscus frustules on the chip: (a) Coscinodiscus frustule imaged by SEM, outer surface facing up. Scale bar: 50 μm ; (b) Inner surface consisting of the vertical chambers. Scale bar: 2 μm ; (c) SEM image of gold electrode on the chip. Scale bar: 50 μm ; (d) Optical image and (e) SEM image of a Coscinodiscus frustule on the gold electrode. Scale bar: 50 μm

The diatom frustule was positioned such that the outer surface of the porous plate, which has the nanoscale pores, is in contact with the metallic gold sensing site, which forms the base of the nanowell of the biosensor (fig. 2-2a). SEM images were acquired using a Philips XL-30 field-emission scanning electron microscope operated at 15~20 kV to visually verify that the positioned diatom frustules completely covered an individual metallic gold sensing site (fig. 2-1e). Hence each sensing site comprised of a working and a counter electrode. The diameter of the working electrode (WE) was 25 μm and the diameter of the counter electrode (CE) was 5 times larger. Electrical measurements were obtained across the WE and CE.

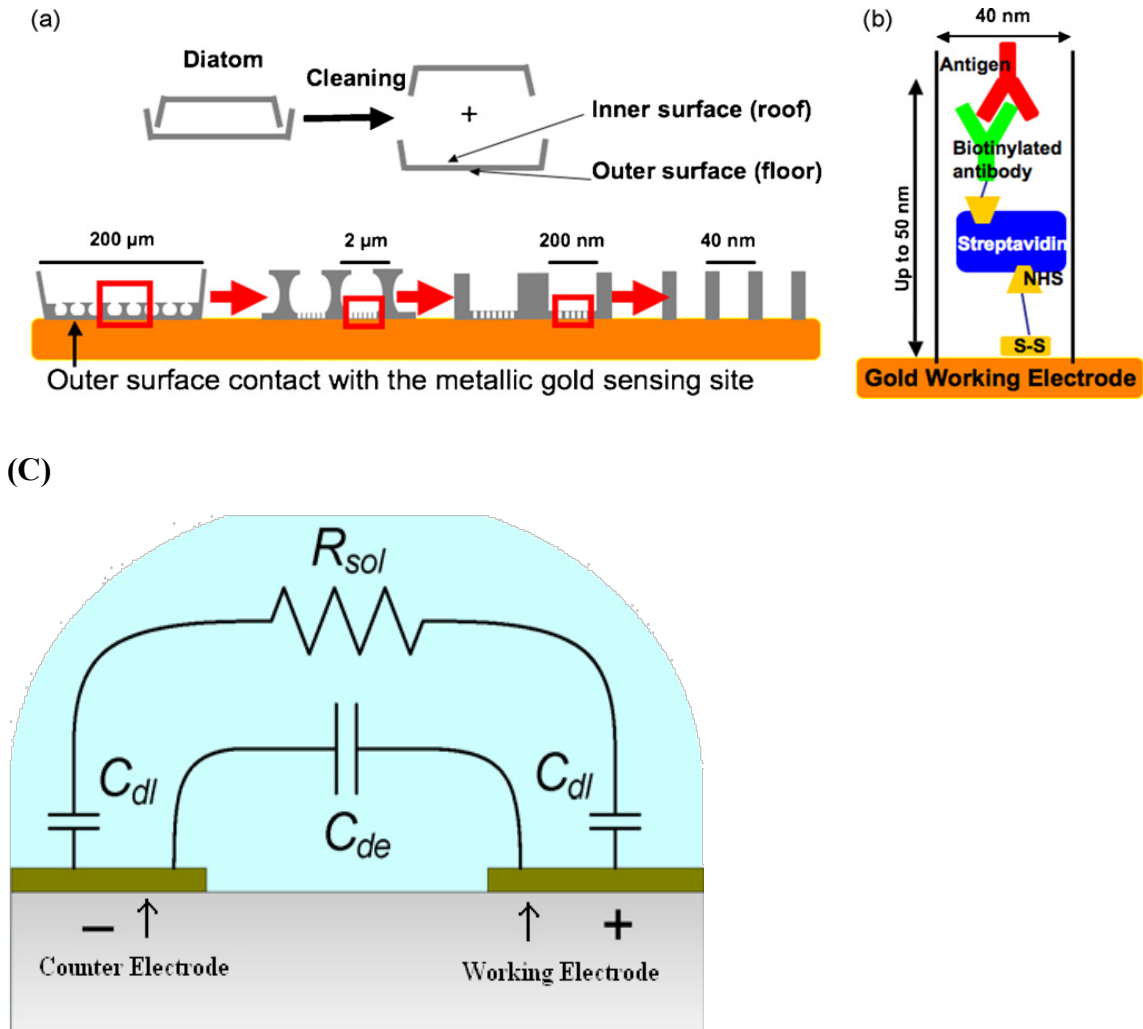


Figure 2-2 (a) Schematic model of frustule pore architecture for the diatom placed on the gold working electrode, (b) schematic showing the antibody-antigen binding inside a nanowell. (c) Equivalent circuit of a sensing site.

2.3 Electrical Impedance Spectroscopy

All the biomolecules (linker molecules, antibodies and antigens) have surface charges.

The binding of these molecules to the base of each nanowell perturbs the charge distribution in the electrical double layer that forms at the solid/liquid interface [54, 87].

This charge perturbation produces a capacitance change in the electrical double layer (fig.

2-2b) [54, 88]. The biomolecule binding induced capacitance change can be measured by the electrical impedance spectroscopy technique. This technique is widely used in electrical biosensors for detecting surface charged analytes [54, 70, 81, 89]. In this technique a low AC voltage is provided as the input to a sensing site, which functions as the electrical stimulus to direct the surface charged biomolecules onto a sensing site. The binding of the biomolecules produces a change in the measured output impedance across a sensing site [54, 88]. The measured impedance is the sum total of two components, the resistance and capacitance of the sensing site. It is only the capacitive component that is a measure of the biomolecule binding event, as the capacitive component indicates the surface charge differential in the electrical double layer as a function of biomolecule binding [54, 90, 91]. Hence the input voltage parameters (frequency and voltage amplitude) need to be optimized to measure this capacitive component.

It was determined that an AC voltage of 100mV at a frequency of 1 kHz when applied between the WE and CE of a sensing site enabled the measurement of the changes to the capacitive component associated with the protein binding event. When the biomolecules are added to the biosensor device, they cause the electrical double layer (EDL) to move upwards. Due to this perturbation of the electrical double layer the capacitance across the EDL changes. Hence monitoring the capacitance change in the EDL is a measure of the protein-binding event. An increase in antigen concentration will in turn increase the capacitance change in the EDL up to an upper bound that corresponds to the absence of free antibody sites. The EDL is approximately 20-50 nm in height, hence capacitance changes only due to biomolecule binding occurs in this region. The equivalent electrical circuit of a sensing site (Fig. 2-2c) comprises of a resistor and two capacitors. The

resistor is a measure of the bulk resistance of the buffer solution, R_{sol} , due to the ions present in the bulk regions of the nanowells (>50 nm from base of the nanowell). The dielectric capacitance between the two electrodes, due to the base substrate is represented by C_{de} . This capacitance does not change for varying input AC voltage frequencies and hence this capacitance is accounted for when the biosensor is calibrated during baseline/control measurements. The electrical double layer capacitance is represented by C_{dl} , which undergoes a change due to the biomolecule-based perturbation to the EDL. The measured C_{dl} capacitance is a sum of the contributions from the WE and CE nanowells. Based on electrochemistry, it has been determined that the bulk resistive component dominates the impedance measurements at high frequencies (>10 kHz) and the capacitive double layer component dominates the impedance measurements at low frequencies (1 kHz and lower) [91-93]. 1 kHz has been determined to be the optimum frequency for operating the biosensor after evaluating the biosensor performance over a frequency range from 50 Hz to 10 kHz. At 100 mV and 1 kHz, and it is at 1kHz the maximum change in the EDL capacitance with minimum background electrical noise was observed.

2.4 Biosensor Surface Treatment

The inflammatory proteins for testing the biosensor performance have been selected from a review of the literature for acute coronary syndrome (ACS) and are histologic participants that constitute a vulnerable plaque [94]. The constituent elements of vulnerable plaque include vascular cells (endothelial and smooth muscle cells) and

platelets. Protein markers from vascular leukocyte cells have been identified as primary markers for vulnerable coronary vascular plaque rupture because the immune system mediates the inflammatory response to vulnerable plaque rupture. The primary protein biomarkers associated with vascular cells are: soluble CD40Ligand, C-reactive protein (CRP), Oxidized-LDL and Myeloperoxidase (MPO). In recent years the research focus has been on identifying the presence of the two protein markers CRP and MPO on the pathophysiology of vulnerable coronary plaque rupture [85, 86]. Hence in this investigation, the focus was on (a) detecting two specific proteins - CRP and MPO in isotonic buffer as well as in human serum and (b) enhancing the detection performance i.e. improving the sensitivity and reducing the cross reactivity more specifically from human serum samples such that the detection performance is comparable to ELISA. Detection of clinically relevant concentrations for both the proteins will be examined in context of establishing the sensitivity of the diatom biosensor in distinguishing between low and high risk to ACS. Recent research has established that CRP level $<1\mu\text{g/ml}$ indicates a low risk; CRP $>1\mu\text{g/ml}$ and $<3\mu\text{g/ml}$ indicates average risk and CRP $>3\mu\text{g/ml}$ indicates high risk of developing cardiovascular disease. Similarly for MPO clinical samples exhibiting concentrations $>0.3\text{ ng/ml}$ are at high risk for cardiovascular disease. Such a performance is especially relevant in the clinical environment, as it will provide a method to detect levels of multiple biomarkers simultaneously to assess activation of the endothelium, leukocytes, platelets, the coagulation system, and plaque turnover to identify patients who may already be primed for an exaggerated inflammatory response.

The antigens CRP, MPO and the biotinylated monoclonal antibodies for these two proteins were all purchased from Calbiochem, San Diego, CA. The monoclonal antibodies were used for the detection assay in order to increase specificity. Detection of the two inflammatory protein markers and identifying the biosensor performance was achieved through a process through a single capture step where the binding of the antigens to the immobilized primary antibodies was transduced into a measurable change in the electrical double layer capacitance. The gold surface at the base of the nanowells was functionalized with dithiobis (succinimidyl propionate) (DSP, Pierce Chemicals, St Louis, MO). DSP (Fig. 2-2b), a covalent linker, has a thiol (sulfur) end group that has great affinity to gold [95, 96]. Hence the thiol end of the linker binds to the gold base of the nanowell and the NHS end group at the opposite epitope end of the linker is available to bind to streptavidin. The entire gold base surface of the nanowell was saturated with DSP linker molecules prior to injecting streptavidin. 10 μ l of streptavidin at a dose of 100 μ g/ml was injected into the diatom nanowells. After a 30-minute room temperature incubation, the nanowells were washed three times with 0.15 M PBS. The concentration of streptavidin required to saturate the nanowell surfaces was identified empirically. 10 μ l of the biotinylated antibody was then injected onto the nanowells and after a 15 minute incubation at room temperature was washed thrice with 0.15 M PBS. The saturation doses of the two antibodies were determined experimentally as detailed in the results section. The antibody-saturated surface was then treated with 10 μ l of 100 μ g/ml of Bovine Serum Albumin (BSA, Pierce Chemicals, St Louis, MO) to ensure blocking of any unbound surfaces of the nanowells. After 15 minutes incubation at room temperature the nanowells were washed thrice with 0.15 M PBS. 10 μ l of 0.15 M PBS was then

injected onto the sensing site and AC input voltage (100 mV, 50Hz-1 kHz) was applied across working electrode (WE) and counter electrode (CE) of each sensing site. The impedance from each sensing site was obtained, which corresponded to the zero dose measurements. After aspirating the 0.15 M PBS solution, 10 μ l of the lowest dose of the antigen was added to the sensing site of the biosensor surface, after 15-minute incubation at room temperature the impedance was measured using EIS. Typically steady state measurements were obtained within 15 minutes of injection of the test antigen sample. After the measurement of the impedance the sensing site was washed thrice with 0.15 M PBS. A schematic representation of the binding of the biomolecules for detection of the proteins within the nanopores of the diatom is shown Figure 2-2a. The same process was repeated for the next highest dose of the antigen for the entire range of doses of the antigen.

To detect antigens from human serum, 10 μ l of commercial human serum free of CRP and MPO was injected into the diatom nanowells after saturating the diatom nanowells with the antibody. After steady state was achieved, the impedance value was noted as the baseline. Aliquots of both the antigens were prepared in the antigen free commercial human serum (GIBCO, Invitrogen, San Diego, CA) for the range of doses. The dose response was performed in a manner similar to that of the dose response for antigens when aliquoted in 0.15 M PBS.

Changes in impedance were measured for the various doses of the two proteins and the change was expressed as a percentage change with respect to the PBS baseline for the pure samples and as a percentage change with respect to human serum base line for the serum-spiked samples.

2.5 Results And Discussion

The discussion of the results is dealt with in three parts (i) antibody saturation isotherms, (ii) protein dose response from pure buffer and serum samples and (iii) selectivity analysis. Two proteins CRP and MPO in pure buffer and human serum samples were tested (A) on planar gold microelectrodes, (B) alumina membranes overlaid on to the gold microelectrodes and (C) diatom membranes overlaid onto the gold microelectrodes to observe the differences.

2.5.1 Antibody Saturation Isotherm

The first set of experiments was performed to identify the dose of the antibody that would saturate the sensor surface. The impedances have been shown at the detection frequency of 1 kHz, as noted in the experimental section. (All measurements were taken triplicate. The measurements were averaged and the average error margin for the data is shown per dose.) Starting from a lower concentration (1ng/ml) of the monoclonal antibodies, nanomembrane-overlaid sensor platform was treated in a step-wise manner with increasing concentration of the antibodies. At 5 $\mu\text{g/ml}$ for anti-CRP and 1 $\mu\text{g/ml}$ for anti-MPO, impedance reached saturation with the diatom membrane while the saturation doses for alumina were 1 $\mu\text{g/ml}$ for anti-CRP as well as for anti-MPO as shown in figure 2-3. There was 26%, 15% and 6 % change from baseline for anti-CRP saturation from diatom, alumina membranes and planar gold respectively and 22%, 12% and 9% change from baseline for anti-MPO saturation from diatom, alumina membranes and planar gold

respectively. This corresponds to a 1.5 to 2 times increase in the relative signal as one goes from alumina to diatom-based sensors, and 1.5 to 2.5 fold increase is seen from gold to alumina.

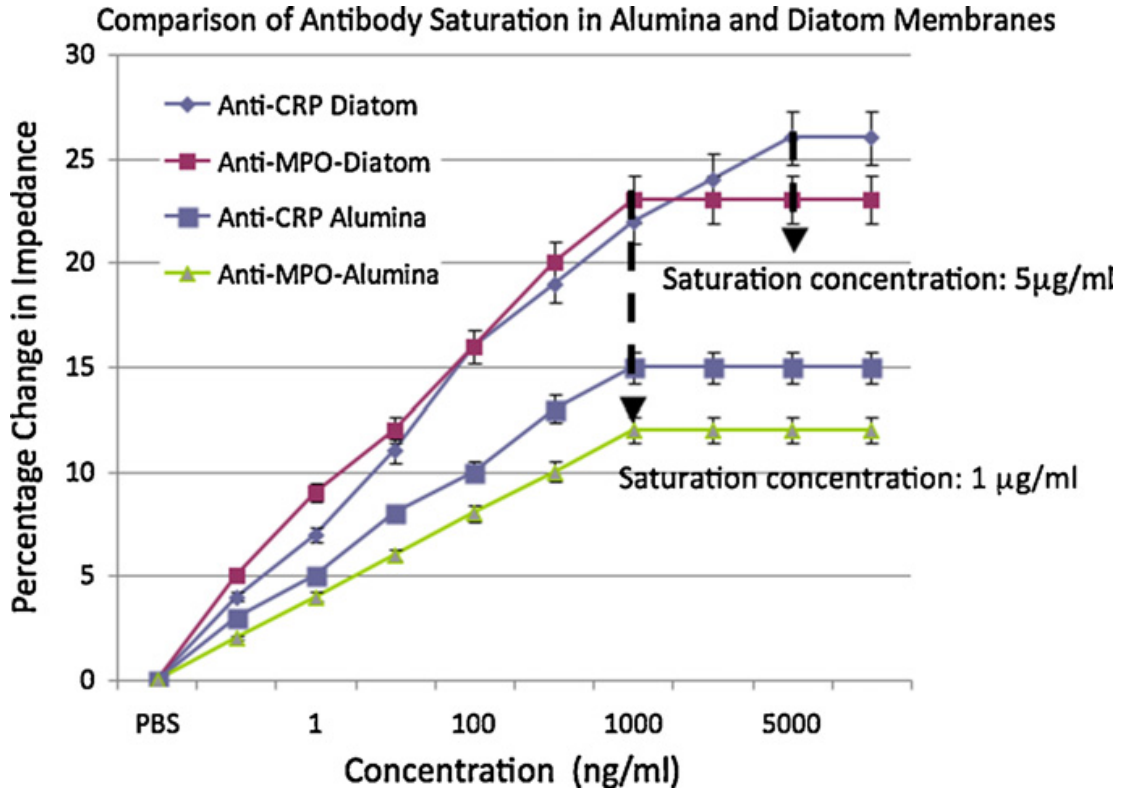


Figure 2-3 Saturation isotherm for the two antibodies on the alumina and diatom substrates, respectively.

The percentage change in impedance from the baseline was considerably higher on the diatom membrane as compared to the alumina membrane, which was higher than that for just the gold film.

It is tempting to assign the increase in the measured signal strength to the increase in surface areas on going from planar gold to alumina to diatom. But, the surface area of the 200 nm pores in the alumina membrane that is exposed to the gold electrode is estimated

to be only 25% of the total surface area of the underlying gold film, where as, the surface area of the 40 nm pores in the diatom membrane that is exposed to the gold electrode is just 5%.

(Note: The comparison of pore density and porosity of alumina membrane and diatom frustule (Fig. 2-4)

Alumina membrane, there are around 800 pores in the area of 10 μm by 10 μm , hence the pore density is $8/\mu\text{m}^2$. The area of one 200nm pore is $0.0314 \mu\text{m}^2$. The porosity of 200nm pore equals $800 \cdot 0.0314 \mu\text{m}^2 / 100 \mu\text{m}^2 = 25.12\%$.

Diatom frustule: there are around 400 pores in the area of 10 μm by 10 μm , and in each 200nm pore there are around ten 40nm pores. The pore density of 40nm pores is $40/\mu\text{m}^2$. The area of one 40nm pore is $1.256\text{E-}3 \mu\text{m}^2$. The porosity of 40nm pore equals $400 \cdot 10 \cdot 1.256\text{E-}3 \mu\text{m}^2 / 100 \mu\text{m}^2 = 5\%$.)

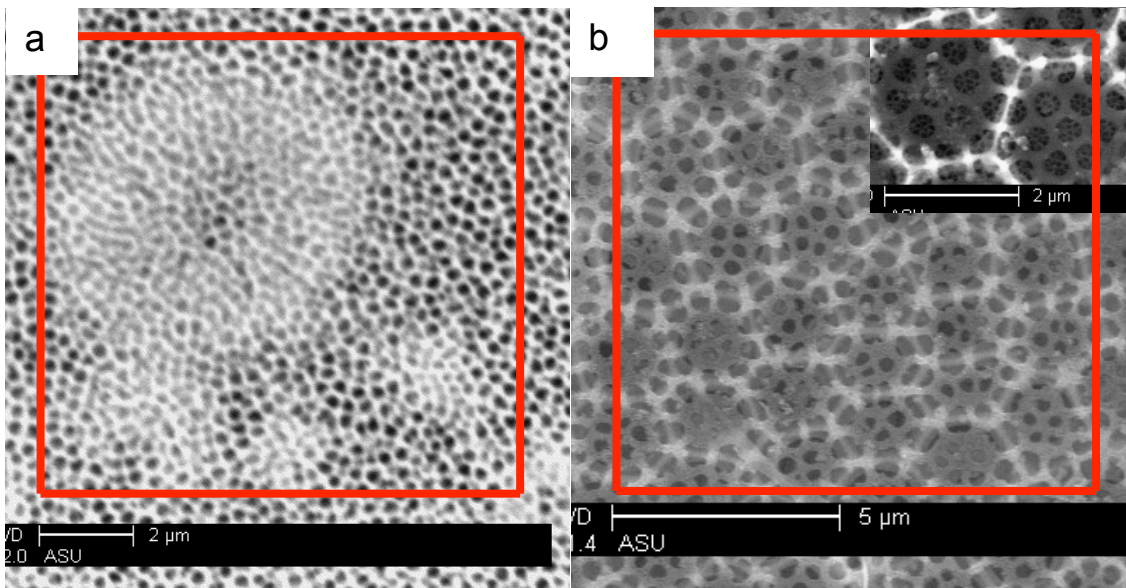


Figure 2-4 The SEM image of Alumina membrane and diatom frustule of *C. Wailesii*. (2a) Alumina membrane. (2b) Diatom frustule of *C. Wailesii*. The inserted image shows smallest 40nm pores inside 200nm pores.

Therefore, the observed increase cannot be explained on the basis of surface areas.

However, when one calculates the pore densities, it is seen that the pore density in the diatom is five times larger than in the alumina membrane. Hence, the results obtained from antibody saturation indicate that the enhanced confinement offered by the diatom nanopores is perhaps playing an important role. Confinement-induced enhancement of antibody-antigen interactions has been postulated earlier [97] to explain the increase of sensitivity due to nanopatterning the surface of a sensor. It has been shown to be particularly effective when the surface is tailored within a few multiples of the antibody-antigen size [97]. It is proposed that the hierarchical pore structure of the diatom offers a topography that can result in confinement-induced enhancement.

In previous studies on nanoporous alumina [54], increased sensitivity has been observed as compared to the native gold film. This obviously cannot be explained by increased

surface area and it was suggested that spatial confinement of the protein biomolecules within the nanopores in could be playing a role. This phenomenon may be physically correlated to macromolecular crowding of proteins in cellular systems that enable protein efficacy and functionality. Within cellular systems, the cytoplasm inside of the cell is typically “crowded” with a complex dispersion of proteins and ions. Unlike the intra cellular environment, protein detection in in-vitro environments such as the biosensor platforms is performed in relatively less dense or “crowded” environments, which are thought to significantly affect the protein efficacy and hence adversely influence the sensitivity of detecting these proteins. To attain the crowding effects within biosensor platforms, the packing density of the protein biomolecules is significantly increased through biomolecule confinement in the nanoporous platforms, which is believed to contribute to enhancing the sensitivity of detection.

2.5.2 Protein Dose Response From Pure And Serum Samples

The dose response studies were performed for the two proteins CRP and MPO over a concentration range from 1pg/ml to 1 µg/ml.). It was observed that the percentage change in impedance increased with the increase in concentration of the antigens. The percentage changes in the impedance were significantly higher during the antigen dose response on diatom membrane as compared to the alumina membrane. The percentage change in impedance from PBS baseline ranged from 60% (MPO), 58% (CRP) on diatom, 38% (MPO) 30% (CRP) on alumina and 22% (MPO), 20% (CRP) on planar gold for the two proteins when aliquoted in PBS over the protein dose range of 1 pg/ml to 1 µg/ml as shown in figure 2-5a. The percentage change in impedance from human serum baseline

ranged up to 42% (MPO), 40% (CRP) on diatom, 33% (MPO), 26% (CRP) on alumina and 15%(MPO) 12% (CRP) , on planar gold electrodes for the two proteins when aliquoted in human serum as shown in figure 2-5b.

The limit of detection was found to be 1 pg/ml for CRP and MPO in pure samples on diatom membranes and 100 pg/ml on alumina membranes and 1 ng/ml on planar gold electrodes as shown in figure 2-5a. Similarly the limit of detection was 10 pg/ml on diatom membranes, 500 pg/ml on alumina membranes and 5 ng/ml for planar gold electrodes for CRP and MPO detection from human serum samples. For proteins in pure buffer, 10-fold increase is seen in sensitivity upon use of nanoporous alumina membrane as compared to gold and a 100-fold increase is realized on going from alumina to diatom. In serum a 10-fold increase is seen from gold to alumina and a 50-fold increase is seen on going from alumina to diatom.

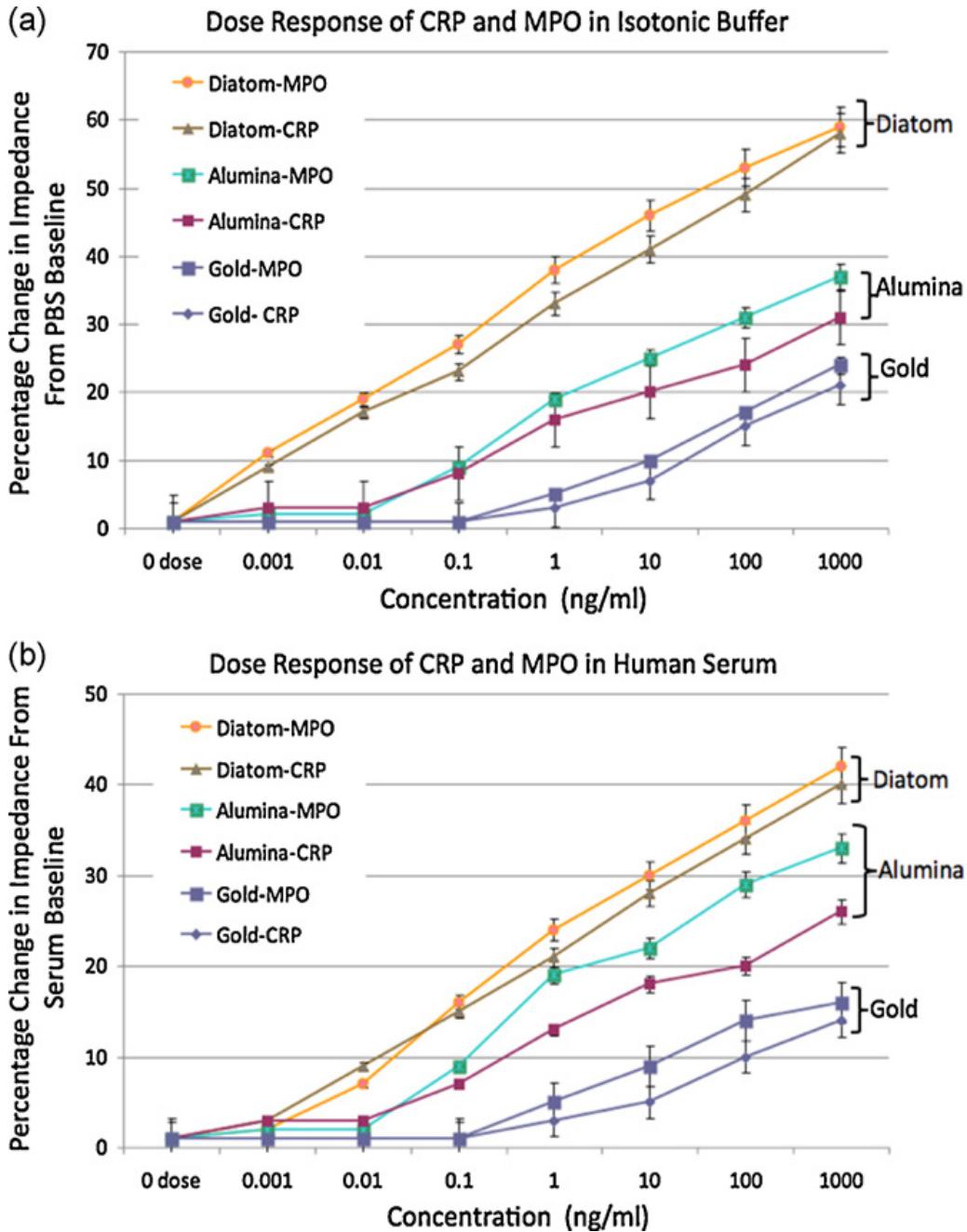


Figure 2-5 Dose response of the two proteins CRP and MPO. (a) The proteins were aliquoted in isotonic buffer samples and were evaluated over a detection regime from 1 pg/ml to 1 μ g/ml. (b) Protein dose response for proteins aliquoted in commercial human serum. Similar to the isotonic buffer samples, maximum changes to the impedance were observed from the diatom substrate as compared to the alumina and gold substrates.

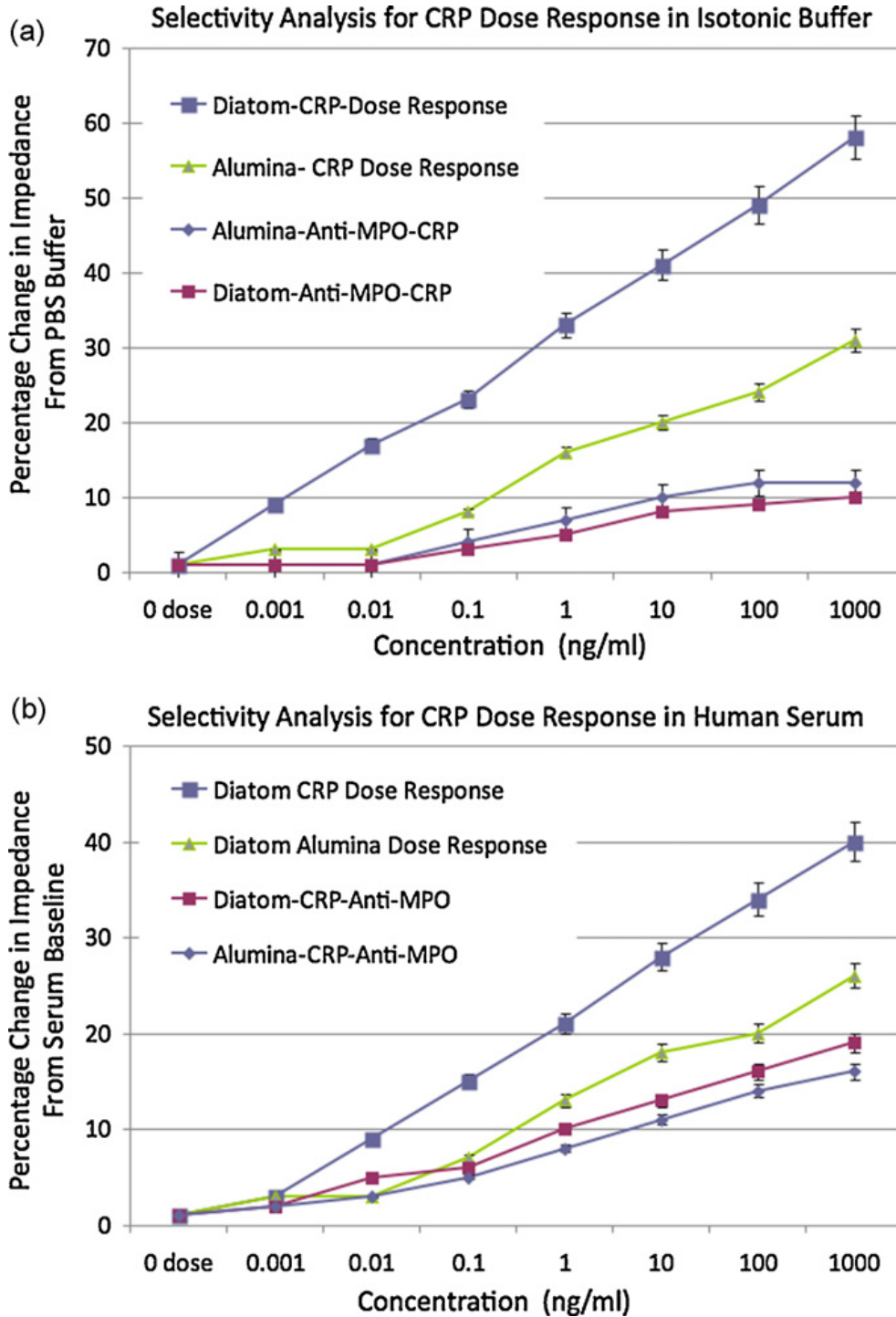


Figure 2-6 Demonstration of selectivity in detection of the protein CRP in isotonic buffer and in human serum samples (a) dose response of CRP aliquoted in isotonic buffer on anti-CRP and anti-MPO saturated diatom and alumina substrates. (b) Dose response of CRP aliquoted in human serum on anti-CRP and anti-MPO saturated diatom and alumina substrates.

2.5.3 Selectivity Analysis

A key feature in identifying the potential of the diatom biosensor towards clinical applicability is to identify its performance in robustly and selectively detecting a targeted antigen from complex samples. In order to simulate these conditions, the efficacy of the diatom biosensor was investigated in detecting the two proteins markers CRP and MPO aliquoted in PBS and commercial human serum over the dose range from 1 pg/ml to 1 µg/ml, on their respective antibody saturated diatom surfaces as well as on the non-specific antibody saturated surfaces (CRP on anti-MPO surface and MPO on anti-CRP surface). These sets of experiments were performed to identify the cross-reactivity of the pure and serum protein samples on similar inflammatory protein receptors. An impedance change of 58% and 30% from base line was observed for CRP dose response on anti-CRP saturated diatom and alumina substrates with the protein samples aliquoted in isotonic buffer samples. Comparatively 10% and 11% change in impedance was observed for CRP aliquoted in isotonic buffer on anti-MPO saturated diatom and alumina substrates respectively (figure 2-6a). In the case of CRP proteins samples aliquoted in human serum, 40% and 26% from base line was observed for CRP dose response on anti-CRP saturated diatom and alumina substrates respectively. Comparatively 19% and 16% change in impedance was observed for CRP aliquoted in human serum on anti-MPO saturated diatom and alumina substrates respectively (figure 2-6b).

In the case of MPO aliquoted in isotonic buffer, 60% and 38% change in impedance was observed over the dose range of 1 pg/ml to 1 µg/ml on anti-MPO saturated diatom and alumina substrates respectively. Comparatively a 10% change in

impedance for MPO samples was observed over the same dose range on anti-CRP saturated substrates (Figure 2-67). For MPO samples aliquoted in human serum impedance changes of 42% and 33% from base line was observed for MPO dose response on anti-MPO saturated diatom and alumina substrates respectively. Comparatively 22% and 17% change in impedance was observed for MPO on anti-CRP saturated diatom and alumina substrates respectively (Figure 2-8). Therefore, these is a nearly two fold increase in impedance for any given dose in the dose response for both the proteins on the specific antibody coated substrate as compare to the non-specific antibody saturated substrate either in PBS or in human serum samples.

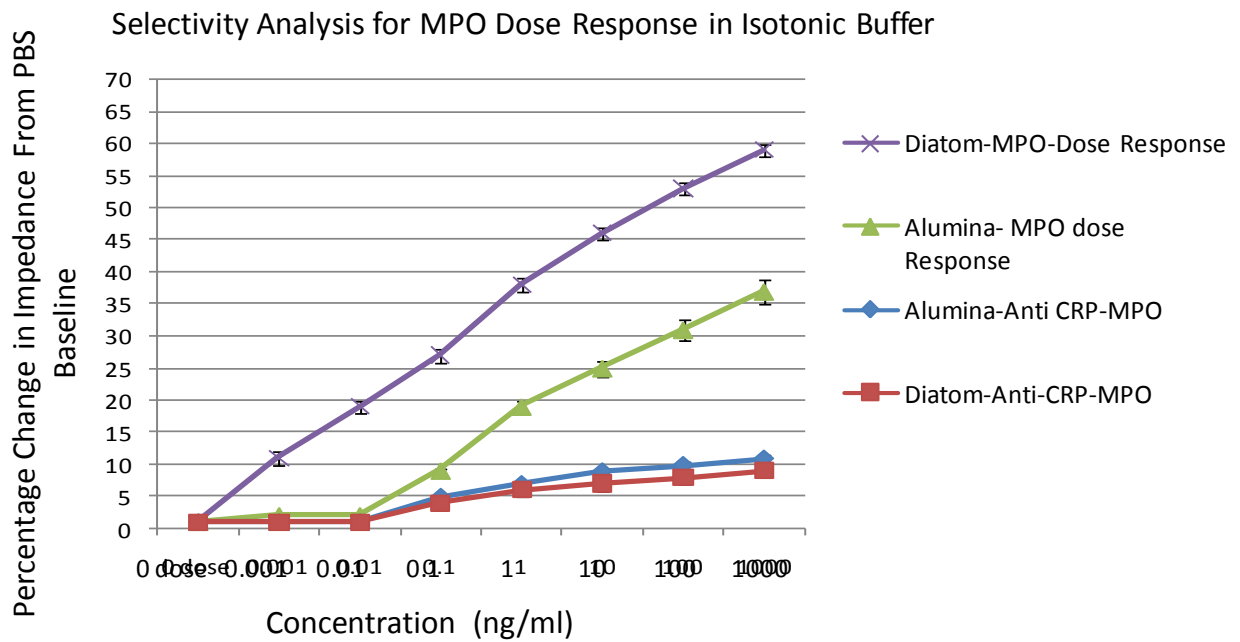


Figure 2-7 Dose response of MPO aliquoted in isotonic buffer on anti-MPO and anti-CRP saturated diatom and alumina substrates.

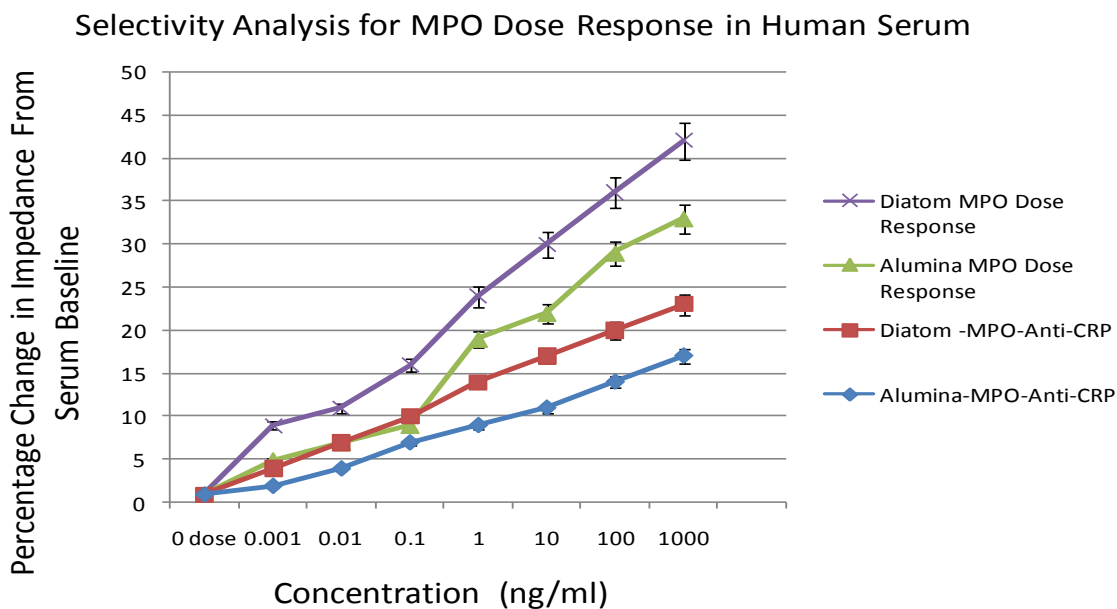


Figure 2-8 Dose response of MPO aliquoted in human serum on anti-MPO and anti-CRP saturated diatom and alumina substrates.

2.6 Conclusion

The design of the diatom membrane-based biosensor is believed to significantly contribute to the enhanced detection strength translating to enhanced sensitivity of the biosensor. Approximately three times enhancement in the impedance changes from planar gold surfaces and twice the improvement in impedance changes as compared to manufactured alumina nanopore surfaces have been demonstrated for individual doses over the dose response range. The diatom membrane surface enables robust detection of the two inflammatory markers in commercial human serum samples at the lower picogram/ml dose regime, which is a clinically significant dose regime in identifying patient risk to cardiovascular disease. The five characteristics viz. Response time, Dynamic range, Signal Strength, Sensitivity and Selectivity, which are critical for a

successful sensor, are all enhanced for the diatom-based sensor. The faster response time and the enhanced sensitivity may be attributed to the enhanced diffusion of fluids in nano channels [98], which in this case would be the nanowells. The linear dynamic range of detection extends from 1 pg/ml – 1 µg/ml (6 orders of magnitude), which is much higher than ELISA (1-2 orders) [99]. The diatom-based sensor exhibits an increase by nearly a factor of two in the relative signal as compared to alumina-based sensors. For proteins in pure buffer, 10-fold increase is seen in sensitivity upon use of nanoporous alumina membrane as compared to gold and a 100-fold increase is realized on going from alumina to diatom. In serum a 10-fold increase is seen from gold to alumina and a 50-fold increase is seen on going from alumina to diatom. Specificity studies have revealed that there is a two fold increase in impedance for any given dose for both the proteins on the specific antibody coated substrate as compared to the non-specific antibody saturated substrate either in PBS or in human serum samples.

In summary, the diatom biosensor could be used as a rapid, label-free screen for selectively detecting disease biomarkers and can be developed as a lateral flow immunoassay device due to the rapid and significantly enhanced impedance changes to the measured electrical impedance due to the binding of the protein biomolecules. There is enormous potential of operating this device in “real-life” conditions to distinguish between low and high cardiovascular risk by detecting proteins in clinically relevant concentrations.

CHAPTER 3

USING DIATOM NANOSTRUCTURES AS TEMPLATE TO FABRICATE METAL NANOMATERIALS

3.1 Introduction

Nanostructured surface can be broadly defined as the typical features have the dimension in the range of 1-100 nm. So far, nanostructured materials or nanomaterials are perhaps the only sub-field of nanoscience that has made the transition from fundamental science to real world applications, thus becoming a technology. [40] Most fabrication processes in nanotechnology involve planar lithographic approaches. Three-dimensional structures are built up layer by layer. Diatom frustules have unique hierarchical nano structures, with regular porous patterns on it, which is so attractive for nanotechnology. One remarkable example is to convert the chemical composition of diatom frustules into a wide variety of non-natural chemistries without losing the 3D morphologies [100]. The porous structure of diatom frustules also motivated the following approaches for replication of two-dimensional patterns. It offers an alternative approach to expensive lithographic fabrication methods. Losic and his coworkers have demonstrated how to fabricate golden inverse diatom replicas by the thermal evaporation of gold [16, 41]. This gold nanostructures with unique morphology, including arrays of nanoscale pillars, rods, have special plasmonic properties, namely, localized surface plasmon resonance (LSPR). Payne's group uses diatoms as templates for the formation of 3D metallic materials, which showed effective surface-enhanced Raman scattering (SERS) effects [36].

In this chapter, a variety of methods will be introduced to fabricate nanostructures through diatom frustules. One application of the metal-enhanced fluorescence will also be presented to show the special property of localized surface plasmon resonance (LSPR).

3.2 Fabrication Nanostructures From Diatom

3.2.1 Different Approaches From Other Group

As mentioned in the introduction, Losic's group has demonstrated the use of diatoms as template to fabricate gold nanostructures (Fig. 3-1). The process starts with the thermal evaporation of gold on the diatom frustules. Evaporated gold condenses inside of the frustule pores, which result in the transformation of the pores into reverse gold structures. [41] Good gold replicas have been obtained from two different diatom species, which suggests that this method may be used as a general approach. However, this method would need a lot of gold as one would have to deposit a minimum thickness of 1000 nm of gold to obtain a continuous film covering the whole diatom frustule.

Payne's group used very similar approach except (Fig. 3-2). they chose silver instead of gold to deposit on the diatom

frustule. Only 30 nm Ag metal were evaporated onto the diatom, then resulting Ag-coated diatoms were isolated by brief sonication. In order to get metallic microshell

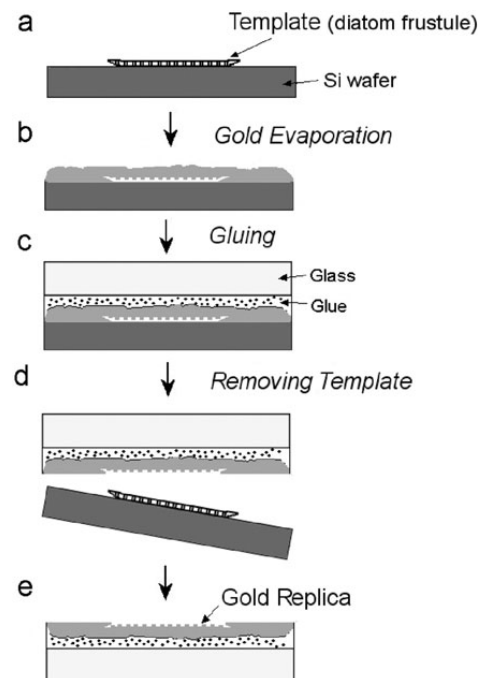


Figure 3-1 Schematic for fabrication of gold nanostructures using diatom frustules as templates from Losic's group.

replicas of the diatoms, the product was treated with 1 % HF for 12-15 hours to remove the silica shell of diatom. The resulting 30 nm thick silver microshell is robust and remains intact throughout the whole process. [36] The microshell with the rough metal surface was also examined with surface-enhanced Raman spectroscopy (SERS), allowing detection to 100 nM rhodamine 6G (R6G).

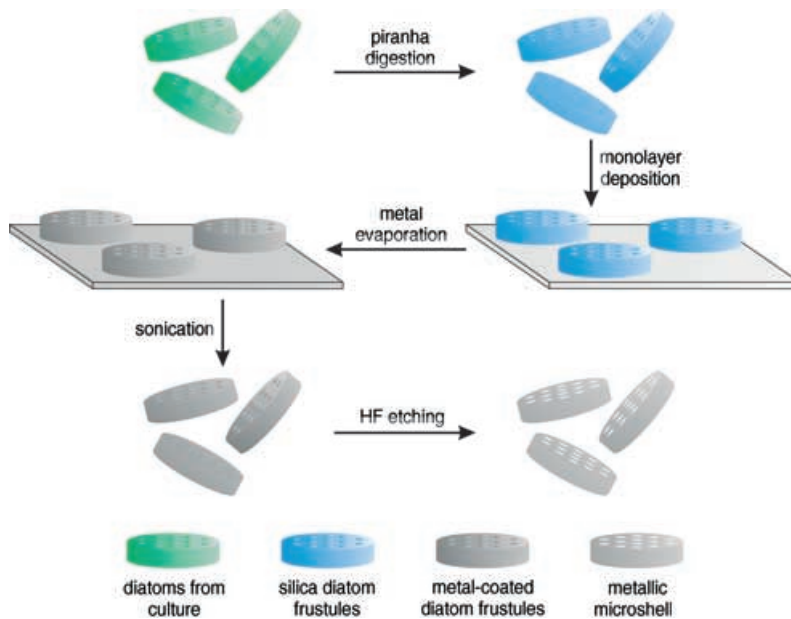


Figure 3-2 The preparation of metal-coated diatom frustules and the isolation of diatom- templated metallic microshells from Payne’s approach.

3.2.2 Electrochemical Deposition

In this section, a method for the high-throughput generation of gold nanorods using template-assisted synthesis nanorod fabrication will be presented. Electrochemical deposition offers marked advantages over other methods for the synthesis of one-dimensional nanostructures. Template-directed electrochemical deposition within nanopores of diatom frustule membranes represents an attractive and reproducible

approach for preparing metal nanorods. This is a process that uses electrical current to reduce dissolved metal ions so that they form a coherent metal coating on an electrode, and does not require expensive instrumentation or high temperatures. Since nanomaterials grown inside the template have a high growth rate, this method is not time-consuming. A power supply provides a direct current to the anode, oxidizing the metal atoms that comprise it and allowing them to dissolve in the solution. At the cathode, the dissolved metal ions in the electrolyte solution are reduced at the interface between the solution and the cathode. The general scheme for the synthesis of one-dimensional nanostructures is shown in Fig. 3-3. The thin metal film is evaporated onto the one face of the template, or the template is placed on the conducting substrate. This metal film is used as a working electrode responding for depositing materials in the pores. Usually, there is a layer of sacrificial metal deposited into the pores to help releasing nanostructures from the substrate. Then, deposition of desired components is performed sequentially, and the nanorods/nanowires are released by dissolving the thin film electrode, sacrificial metal layer, and template.

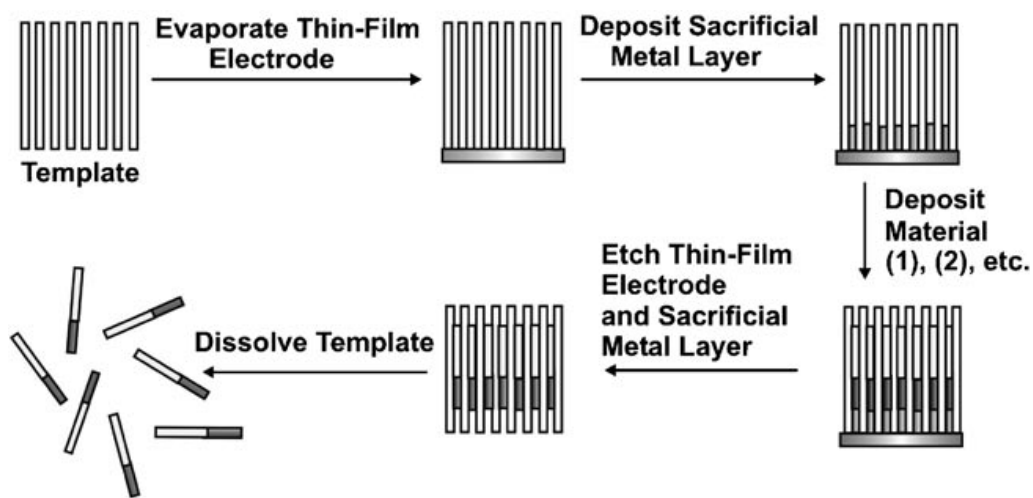


Figure 3-3 Schematic steps for the synthesis of nano-structures (nanorods and nanowires) by the deposition of materials into nanoporous templates. [101]

3.2.3 Materials And Methods

The diatom frustules were deposited on the aluminum foil membrane, which was sputtered with a thin film of gold to assist electrochemical deposition and enhance the electrical contact. Two types of diatoms were chosen as templates, the first one is pennate diatom, *Nitzschia frustulum* and the second is centric diatom, *Coscinodiscus wailesii*. (Fig. 3-4) The membranes were then transferred to a three-electrode electrochemical growth cell. Gold electroplating solution (Orotemp 24 RTU RACK, Technic Inc.) was

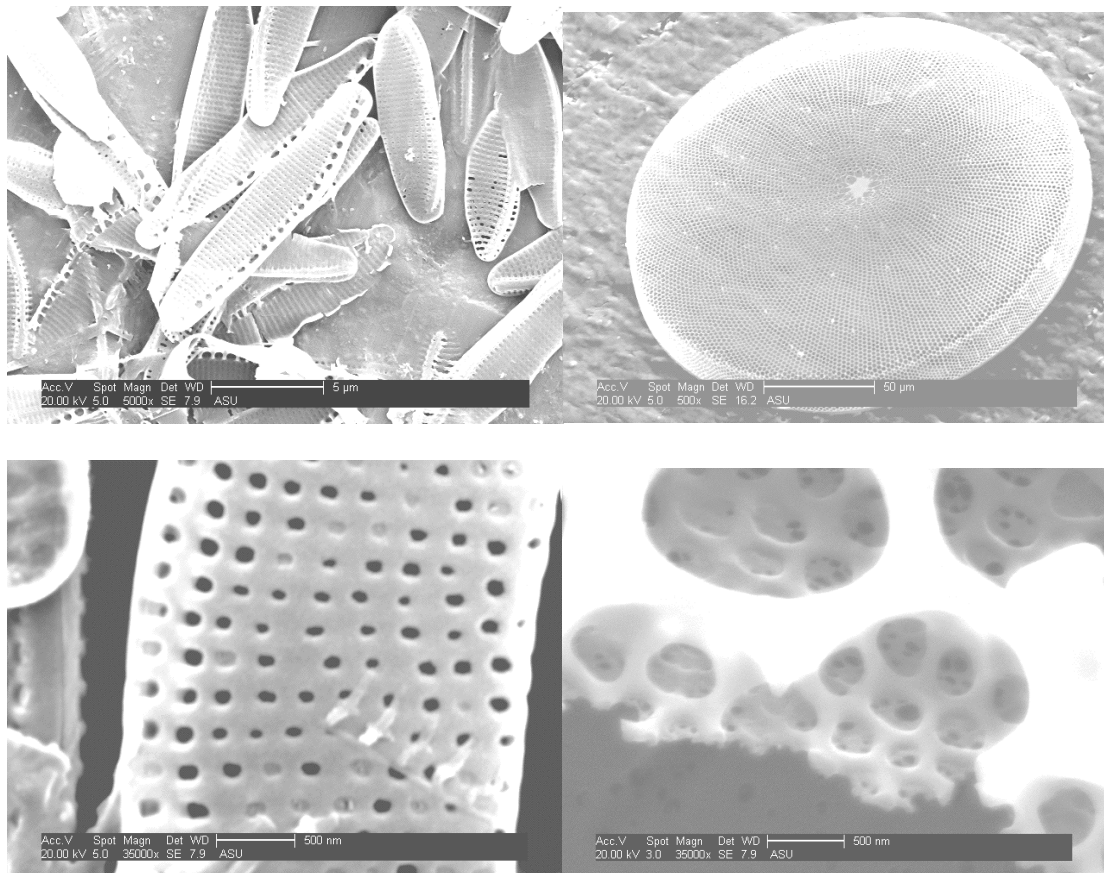


Figure 3-4 Left panel is pennate diatom; *Nitzschia frustulum* and right panel is centric diatom, *Coscinodiscus wailesii*. Lower column is the higher magnification images of *Nitzschia frustulum* and *Coscinodiscus wailesii*.

added into the cell and gold layer was deposited at -0.9V . The gold deposition was conducted at 0.2 to 0.4 C (One coulomb is equivalent to one ampere flowing for one second ($1\text{ C} = 1\text{ A sec}$)). The final thickness of gold deposition will depend on the time and current. Upon completion of gold deposition, a final rinse was performed and the membrane was removed from the growth cell (Fig. 3-5).

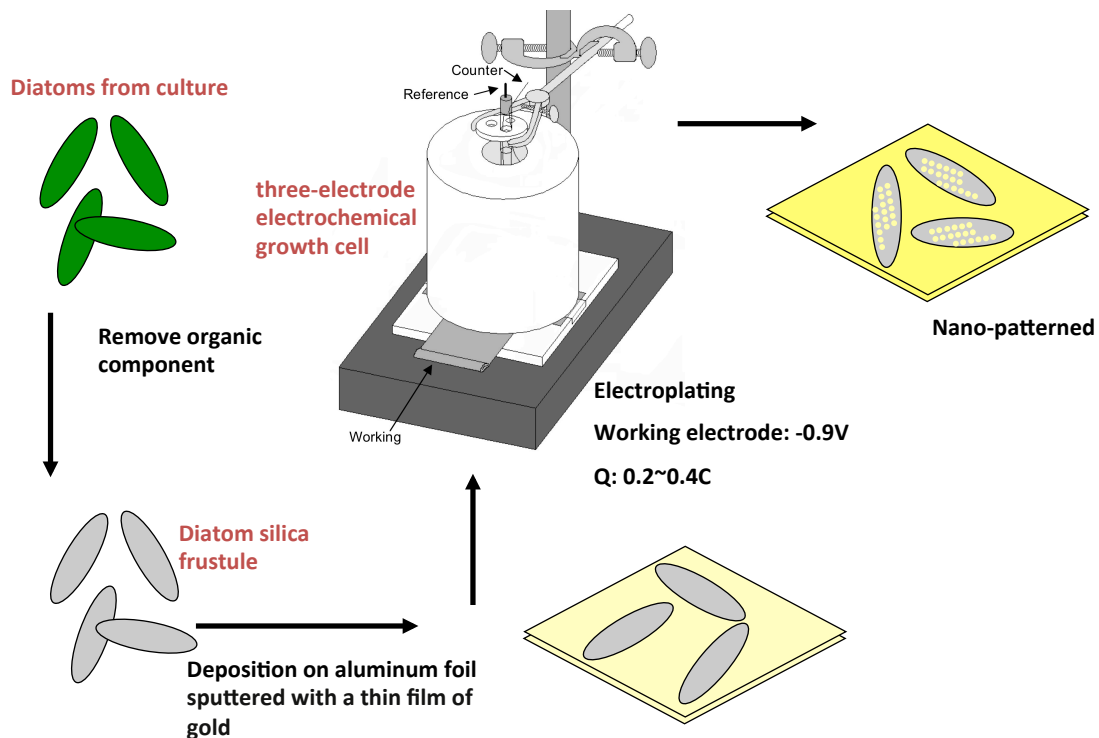
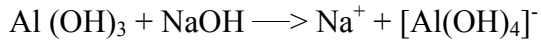
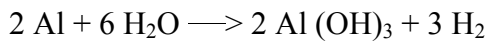


Figure 3-5 The serial procedures for the process of the electrochemical deposition.

Membranes were then divided into two parts so that one part was saved for imaging and the other was dissolved for analysis of nanorods. The aluminum foil membranes were cut into small pieces and put into microtube. The 3 M NaOH solution was added to dissolve membrane for 15 min with agitation and sonication. Free gold nanorods were then

precipitated via centrifugation and rinsed in nanopure water repeatedly until a neutral pH was achieved. (Fig. 3-6)

With the production of aluminates ($\text{Al}(\text{OH})_4^-$), the amphoteric (capable of acting as either an acid or a base) aluminum hydroxide $\text{Al}(\text{OH})_3$ goes in solution:



A layer of aluminum oxide previously formed by passive corrosion is dissolved by the addition of sodium hydroxide. $\text{Al}_2\text{O}_3 + 2 \text{NaOH} + 3 \text{H}_2\text{O} \longrightarrow 2 \text{Na}^+ + 2 [\text{Al}(\text{OH})_4]^-$

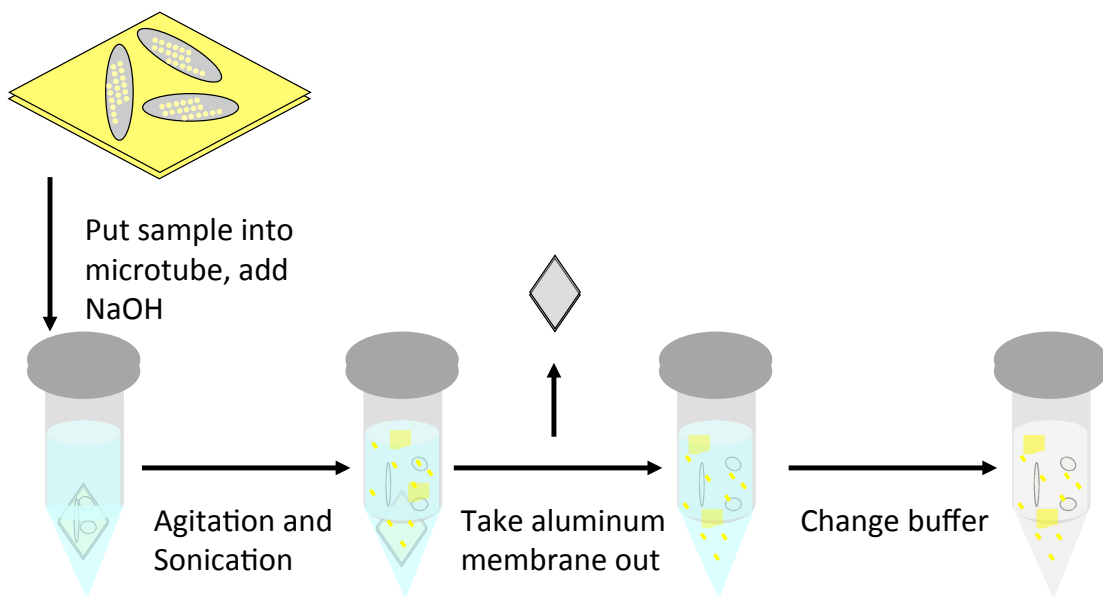


Figure 3-6 Releasing gold nanorods from diatom template and substrate.

3.2.4 Gold Nanorods/Nanopatterns From Diatom Frustules

A series of SEM images of the gold nanopattern on the surface of the *Nitzschia frustulum* frustule are shown in Fig. 3-7. The main feature of this diatom is that it has periodically organized pores with an average diameter of about 100 nm, with the range from 60 nm to 120 nm.

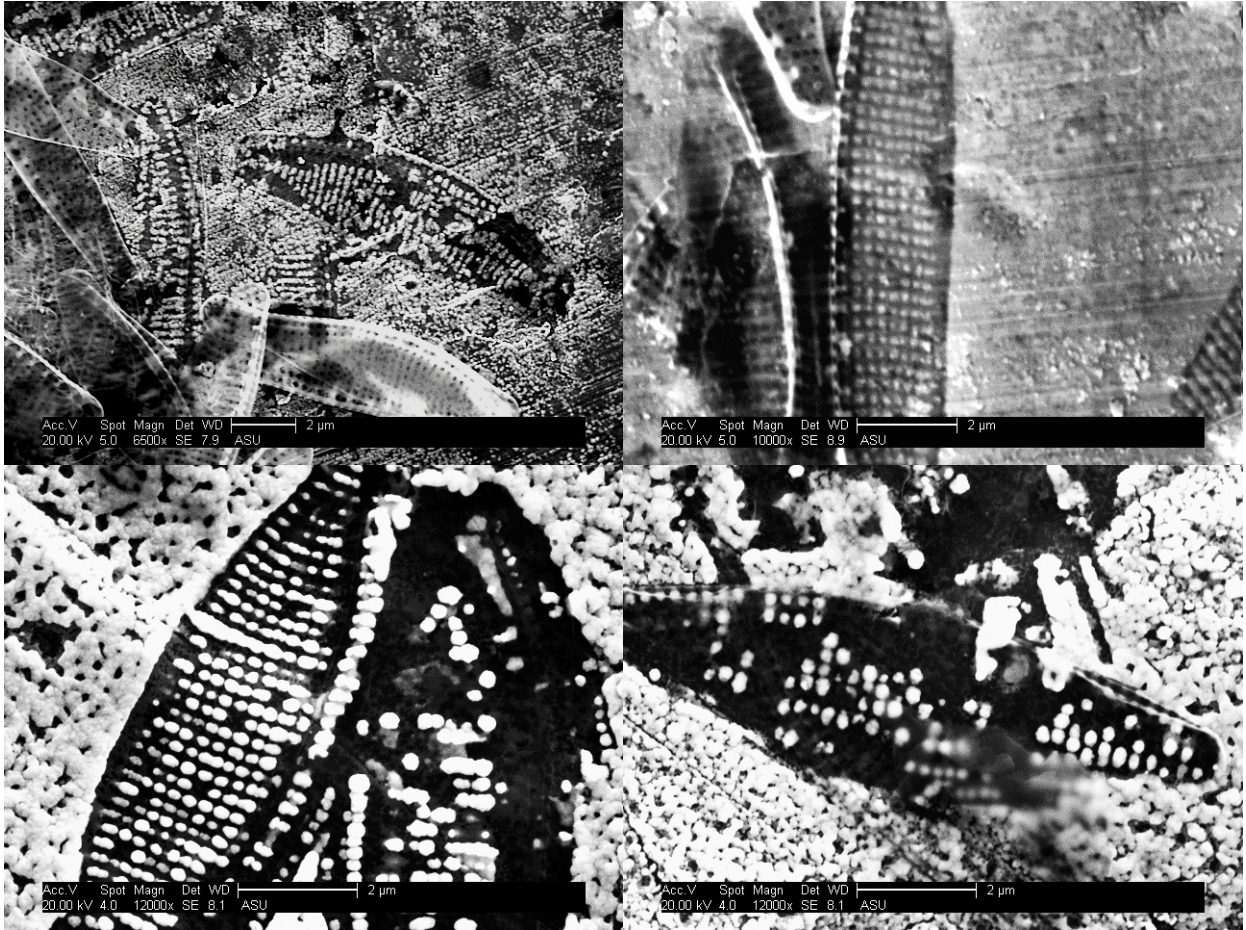


Figure 3-7 The SEM images of gold nanostructures fabricated by electrochemical deposition using *Nitzschia frustulum* frustules as template.

Another series of SEM images of the surface morphology of the frustule template from the external membrane and girdle band of *Coscinodiscus sp.* and the corresponding gold

nanorods/nanopatterns structures are shown in Fig. 3-8. The pore size of *Coscinodiscus* sp. from the external membrane is around 40nm, and the average pore size of girdle band is 200nm.

From the gold nanopatterns left behind on the membrane surface, it is obvious that the shape, size, and organization of gold structures represent the void of the porous frustule valve.

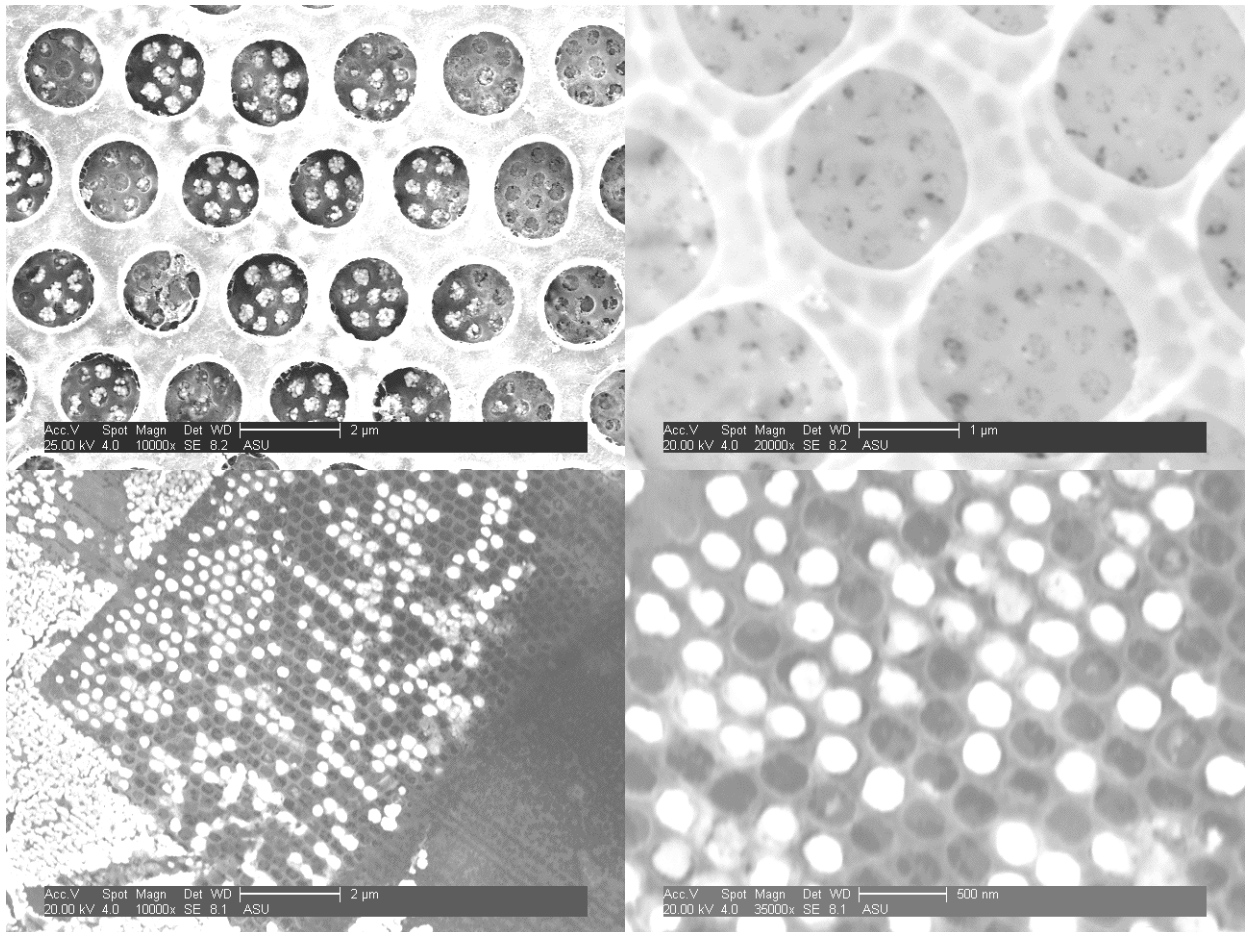


Figure 3-8 The SEM images of gold nanostructures fabricated by electrodeposition using *Coscinodiscus wailesii* frustules as template. Top two images are nanorods inside the valve of frustule. Bottom two images are nanorods in the girdle band of frustule.

3.2.5 Gold Nanorods From Diatom Templates

The next step is to release gold nanopatterns from membrane surface so that free gold nanorods in the solution can be obtained. Fig. 3-9 shows SEM images of gold nanorods from *Nitzschia frustulum* and the dimension of these rods are also analyzed.

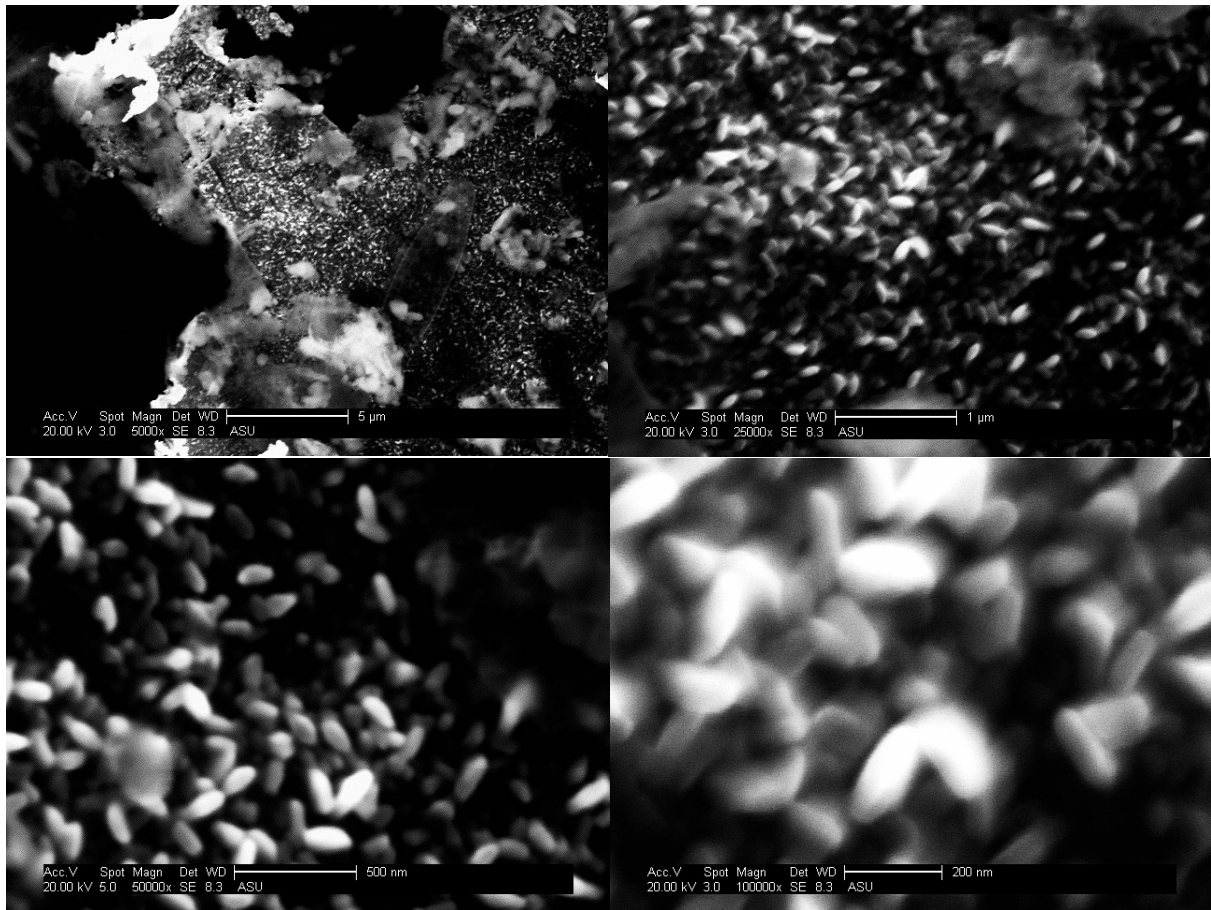


Figure 3-9 The SEM images of gold nanorods released from the membrane using *Nitzschia frustulum* frustules as template.

The average length of gold nanorods is 168.7nm and the average diameter of gold nanorods is 73.4nm. (Fig. 3-10) This number is matched with the dimension of the pores of *Nitzschia frustulum* which pore size ranges from 60nm to 120nm. The length of

nanorods depends on two factors. One is the time period of electrochemical deposition, and another one is the thickness of the diatom frustule. For the first factor, under the same electric current condition, the longer time it was deposited, the longer nanowires would grow. However, the second factor would limit the length of nanorods. The average thickness of *Nitzschia frustulum* is 200 nm. If the nanorods were grown over the thickness of diatom frustule, then the gold would not only deposit within the pores, but also deposit on the surface of the frustule. For the case *Nitzschia frustulum* was used as template, the length limitation is 200 nm. The nanorods have been examined by the EDAX to characterize the composition. As shown in figure 3-11, the spectrum shows the major composition of nanorods is gold, verifying that the nanorods come from electrochemical deposition of gold.

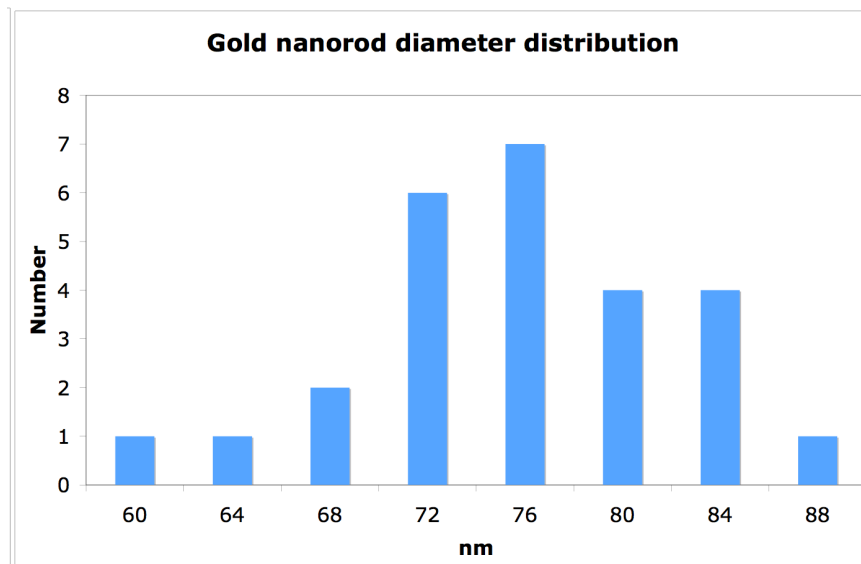
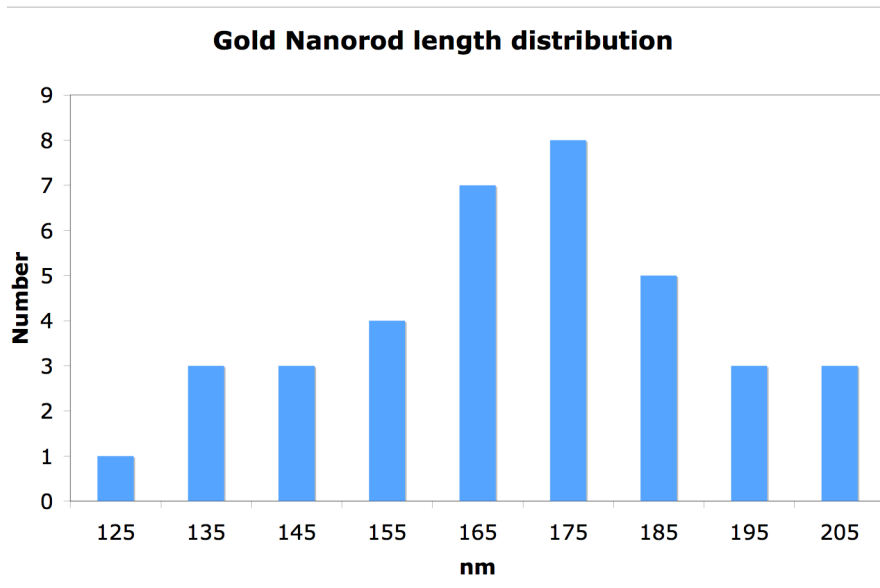


Figure 3-10 The histogram of the length and diameter of gold nano rod fabricated by diatom-templated electrodeposition. The average length of gold nanorods is 168.7nm and the average diameter of gold nanorods is 73.4nm.

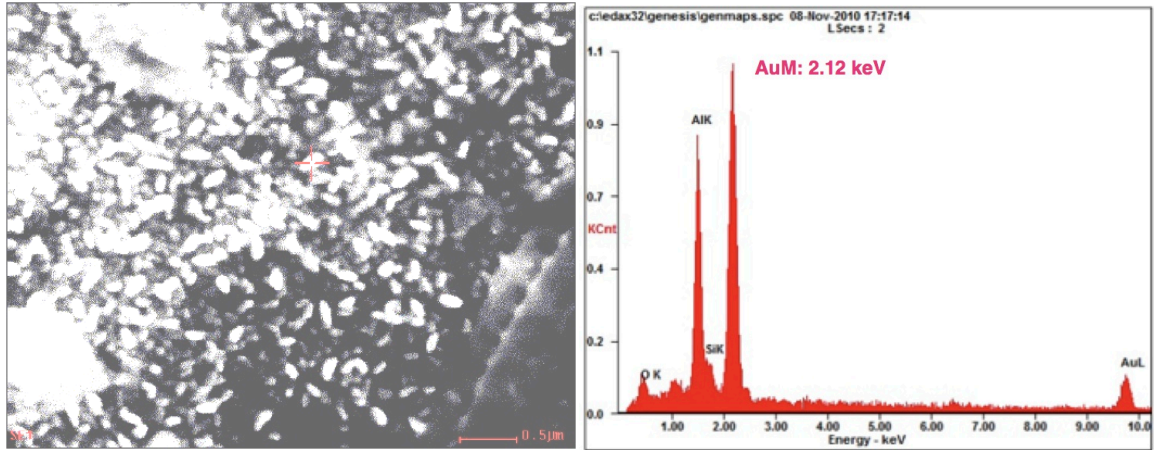


Figure 3-11 EDAX spectrum of gold nanorods

3.2.6 Conclusion

The procedure is fairly generic and can be used with a variety of metals and any diatom species to produce a library of structurally unique materials. Diatom-templated approach can be used for the cost-effective generation of solid gold nanorods, followed by dissolution and detachment of the diatom template. By modifying the procedure of alternately deposition segments of desirable and non-desirable metals, multiple nanorods would be obtained. The alloy nanorod can also be obtained by depositing from gold-silver mixed plating solution, and porous gold nanorods can be done by selective etching of alloy nanorods. Nanorods have wide variety of applications. Gold nanorods are considered excellent candidates for biological detecting applications. In addition, nanorods with near-infrared absorption peaks can be excited by a laser at the absorbance band wavelength to produce heat, potentially allowing for the selective thermal destruction of cancerous tissues [102].

Before releasing the nanorods from the surface, the gold nano-patterned surface could be used as substrates for the optical detection techniques, such as surface-enhanced Raman spectroscopy (SERS) and metal-enhanced fluorescence (MEF). However there is a significant problem with gold plating baths with the poor stability as the instability of gold plating solutions usually leads to the formation of colloidal gold. The formation of colloidal gold is undesirable, as the particles tend to increase surface roughness. If the nano-patterned substrate was fabricated by this method for SERS or MEF application, one has to control the plating bath condition very well to prevent the formation of colloidal gold. Or, another approach can be examined to get good nano patterns by using diatom as template. The next section the physical deposition method to fabricate nano structures from diatom frustules will be demonstrated, and the application of metal-enhanced fluorescence will be studied.

3.3 Sputter Coating And Metal-Enhanced Fluorescence Application

In this section, the gold nanostructures are formed by means of sputter deposition of gold onto porous frustules. Gold nano-patterns on substrate will be obtained upon release from the diatom templates and will be characterized using scanning electron microscopy (SEM), and atomic force microscopy (AFM). This gold nano-patterned surface can be used as substrates for the optical detection by using surface enhanced Raman spectroscopy (SERS) [36] and metal-enhanced fluorescence (MEF) [103].

The most commonly used physical vapor deposition (PVD) evaporation techniques are thermal and sputtering. In thermal evaporation, the source material is brought to evaporation temperature either by the heat generated by the resistance of a metal container or by bombardment of a beam of high-energy electrons. In sputtering process, it requires the generation of energetic heavy + ions (generally Argon) that are responsible for sputtering atoms from the target. An electric field between target and anode contains the electron cloud. Magnetic fields cause the electrons to spiral and collide with Ar atoms, which are then ionized. The Ar⁺ are accelerated, strike the target, and knock off target atoms. Sputtered energies can be 1 to 10 eV, while evaporated energies are <1eV. The result is that the sputtered films are denser, generally amorphous in nature and more adherent than evaporated films. Thermal evaporation provides energy in the 0.1-0.15 eV range, thus does not damage substrate surface. However, sputtering with high energy can damage substrate surface for the impact of high-energy species.

The advantages of evaporation deposition include the high deposition rate (~ 0.1 $\mu\text{m}/\text{min}$), little surface damage, excellent purity of the film because of the high vacuum condition, and very little substrate heating. However, it is more difficult control of film composition than sputtering and also has x-ray damage caused by the electron beam evaporation. The advantages of sputtering deposition include more reproducible deposition control- same deposition rate for same process parameters, so it's easy to control the film thickness via time. Although the substrate or diatom template may be damaged due to ion bombardment, it was still a proper attempt to examine if we can use this technique to get nanopatterns from diatom frustule.

3.3.1 Metal-Enhanced Fluorescence

Fluorescence technology has been one of the most widely used in many fields and plays an important role in biotechnology and medical diagnostics. This technique is of particular interest because the specific interaction of an antibody with its antigen is used for molecular recognition. While fluorescence detection can be very sensitive, the wide spread application of this technique is usually limited by the quantum yield and the photosatability of the fluorophores. The optimization of the performance of fluorophores has been explored by many methods; one approach is using quantum dots to enhance the sensitivity and stability [104-106] and another viable approach is to explore the nanomaterial and nanostructure based substrates to enhance fluorescence signals [103, 107-109]. The strong interactions of fluorophores with metallic nanostructures lead to the production of surface plasmons and result in significant increases in intensity, photostability, and decreases in lifetime. Fluorophores are excited with an external light source and the energy from the electronically excited states (fluorescence emission) is

partially transferred (coupled) to surface plasmons in metals in close proximity (<100 nm). As a result of the plasmon coupling, two distinct observations can be made: (1) an increase in fluorescence emission and (2) a decrease in the lifetime of the fluorophore. These effects result from interactions of the excited-state fluorophores with free electrons in the metal, the so-called surface plasmon electrons, which in turn produce favorable effects on the fluorophore. The effects of metallic surfaces include fluorophore quenching at short distances ($\sim 0-5$ nm), spatial variation of the incident light field ($\sim 0-15$ nm), and changes in the radiative decay rates ($\sim 0-20$ nm). [110]

Lakowicz and Geddes refer to this phenomenon as metal-enhanced fluorescence (MEF) [103, 110]. They discussed the interaction of fluorophores with the metal by the following mechanisms: (1) Energy transfer from the fluorophores to the metal surface, therefore quenching the fluorescence. It is a non-radiative process and at a distance less than 5 nm, and can be understood by damping of the dipole oscillation by the nearby metal. It is due to a coupling between the fluorophore and the plasmon polariton at the surface of the metal. (2) The concentration of the electromagnetic field. When metallic structures act as antennas concentrating the field in places where the fluorophore is located, consequently, enhance the fluorescence. In this case, it has been found that the electric field is intensified around sharp corners/tips of metal nanostructures, which is also known as the “antenna” effect. When subject to an external electromagnetic field, the electrons move coherently inside the material. The presence of these small displacements from equilibrium causes the charge density wave to oscillate in the metal. The oscillations are called localized surface plasmon resonances. Such localized plasmon resonances in two or more close nanopatterns may be coupled with the resulting

electromagnetic field highly amplified between the nanopatterns. (3) The modification of the rate of the fluorophore with an increased the intrinsic radiative rate and decreased the lifetime of the fluorophore. It is due to higher photonic mode density in the proximity of metal nanostructures. To better understand this concept it is informative to consider the Jablonski diagram for fluorophores in the free-space condition and the modified form when in close proximity to conducting metallic particles or colloids (Fig. 3-12).

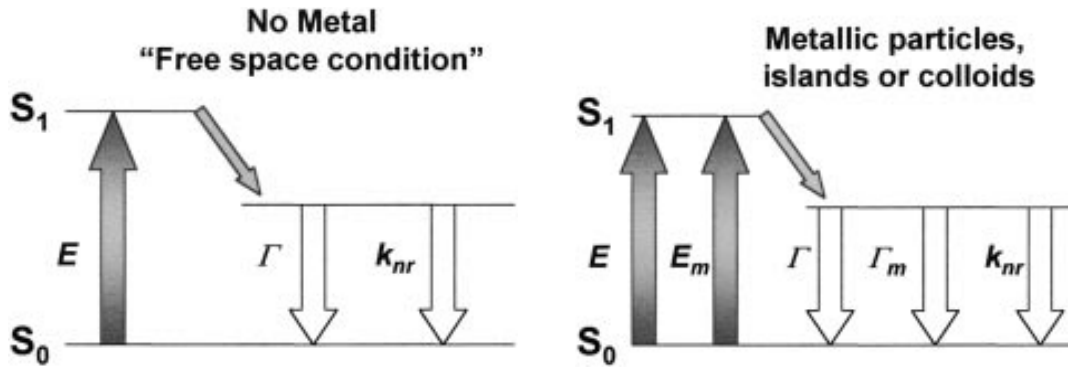


Figure 3-12 **Classical Jablonski diagram for the free-space condition and the modified form in the presence of metallic particles, islands or colloids.** E -excitation, E_m -metal enhanced excitation rate, and Γ_m - represents the radiative rate due to the metal proximity; k_{nr} is the non-radiative rate. From Geddes and Lakowicz. [103]

The fluorescence lifetime (τ_0) is given by:

$$\tau_0 = \frac{1}{\Gamma + k_{nr}}$$

Γ is the radiative rate of the fluorophore, and k_{nr} is the non-radiative rate.

In the present of metallic particles or nanopatterns, the radiative rate is modified. The new lifetime replacing the previous equation to

$$\tau = \frac{1}{\Gamma + \Gamma_m + k_{nr}}$$

Γ_m represents the radiative rate due to the metal proximity.

When fluorophores are placed at suitable distances from metallic particles or surfaces, fluorophores can undergo modifications to the radiative decay rates, Γ_m , where an increase in Γ_m results in reduction in lifetime. At this point it is informative to consider how modifications of both E_m and Γ_m are likely to influence other free-space fluorescence phenomenon.

Both quantum dots and nanostructured substrates approaches are useful and important to detect low concentration of biomolecules.[111] For the purpose of on-chip fluorescence detection and imaging, the MEF approach would be more useful if fluorescence substrate can be readily integrated into microdevices. Many metallic and non-metallic nanostructures have been used and show great potential, such as gold surface nanoscale grating [112], silver fractal nanostructures [113], gold plasmonic nano-antenna dots [114], and micropatterned nanostructured aluminum oxide [115]. However, the expensive nanofabrication process, such as electron-beam lithography or focused ion-beam milling, needed to fabricate nanostructure substrates make MEF inaccessible to many potential users. Alternative simple and cost-effective techniques such as soft lithography, and polymer transfer printing have been developed to broaden the accessibility [116, 117]. Biomaterials are a relatively new source of inspiration and template for the design and fabrication of nanostructured materials [118, 119]. One group had used porous diatom frustules as template to fabricate gold nanostructures [16, 41]. The metal-coated diatom frustules and diatom-templated metallic shells also hold great potential for surface-enhanced Raman spectroscopy (SERS) applications [36].

As periodically metallic nanopatterns surfaces have proven effective as MEF substrates, it was hypothesized that the diatom-templated metallic substrates could potentially be used as substrates for the fluorescence detection of analytes.

Here the approach of using the diatom frustule as template for fabrication of gold nanostructures is presented and the application of metal-enhanced fluorescence surface examined. The process starts by the sputter coating of gold on the diatom frustules and silicon wafer, followed by sonication to remove diatom frustules to leave the inverse gold structure on surface as MEF substrate. Given its simple and cost effective fabrication process and capability to be integrated with microchips and systems, this approach may suitable for a great deal of applications which require high-throughput and sensitive fluorescence detection of biomolecules.

3.3.2 Material and Method

The 10 mm x 10 mm individual pieces of silicon wafer was used as gold deposition substrate. Few drops of cleaned frustule suspension were deposited onto silicon wafers and were dried under a gentle stream of nitrogen for 1 to 2 minutes. Frustules were randomly deposited on the substrate surface by exposing their inner or exterior surface. The gold thin film (30 nm) on the diatom frustule templates and silicon wafers was performed using the Hummer X Sputter System. Following sputter coating, the resulting metal-coated diatom frustules were removed from silicon wafer surface by brief sonication in EtOH for 30 seconds, and leaving gold nanostructures on the substrate (Fig. 3-12).

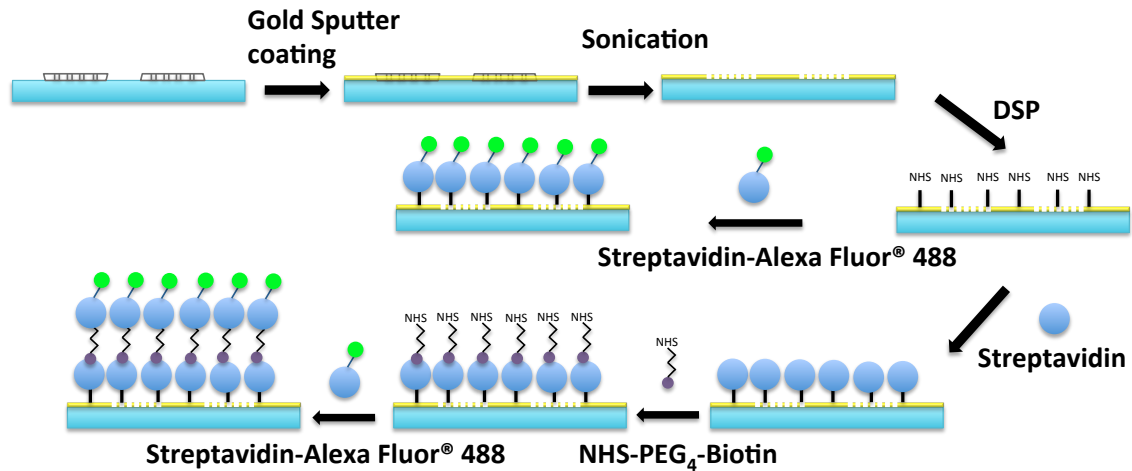


Figure 3-13 Schematic illustration of fabrication gold nano structures from diatom frustules. Serial procedures have been done on surface for the fluorescence enhancement experiment.

SEM images of the products reveal that the gold coating is deposited homogeneously across the silicon wafer surface and maintains the intricate micro- and nanoscale features of the diatom templates. In most cases, when the frustule templates were removed from the surface, a gold thin film remained on the silicon wafer after sonication. The resulting gold films after removal of frustule were rinsed with copious amounts of double deionized (18 M Ω *cm) water and dried under a stream of nitrogen.

A series of surface modification procedures were conducted as schematically illustrated in Figure 3-13. The gold nanopatterned chips were immersed in 4 mg/mL DSP in DMSO for 30 min and then rinsed with DMSO and distilled water. In order to compare the effect of distance between the fluorescence dye and metal surface, two procedures have been used. One was to add 100 μ g/mL Alexa Fluor[®] 488 conjugated with streptavidin directly on the activated gold surface, which was formed by thiolation reaction between the gold

film and DSP for 1 h, and then rinsed with distilled water. The other end of DSP is NHS group that will react with primary amino group protein from streptavidin. Another procedure was to add 100 µg/mL streptavidin on the activated gold surface for 1 hr, rinsed with distilled water and then 1 mg/mL NHS-PEG₄-Biotin in DMSO. After 1 hr, it was rinsed with DMSO and distilled water. NHS-PEG₄-Biotin was used as a spacer between dye and surface because biotin can bind to streptavidin and NHS group can react with primary amino group from Streptavidin-Alexa Fluor® 488. Final step was to add 100 µg/mL Streptavidin-Alexa Fluor® 488 for 1 hr. The unbound dyes were washed away gently using DI water and substrate is dried under a stream of nitrogen. All reactions were conducted at room temperature. Fluorescent images were captured by using a fluorescence microscope equipped with a mercury arc lamp source (Olympus, Inc.). The sample was excited by mercury arc lamp source with excitation filter, 475-490 nm. The fluorescence enhancement is determined by analyzing the fluorescence images using the ImageJ, developed at the National Institutes of Health. Program ImageJ has been used to read files of fluorescence images and measure the mean value of intensity on gold thin film and nanopatterns.

3.3.3 Results And Discussion

The scanning electron microscopy (SEM) images of *Coscinodiscus wailesii* frustules and gold micro-/ nano- patterns are shown in Figure 3-14. Figure 3-14(a) shows diatom

frustule placed on silicon wafer after gold sputter coating, and 3-14(b) shows the gold patterns after removing diatom frustule by sonication.

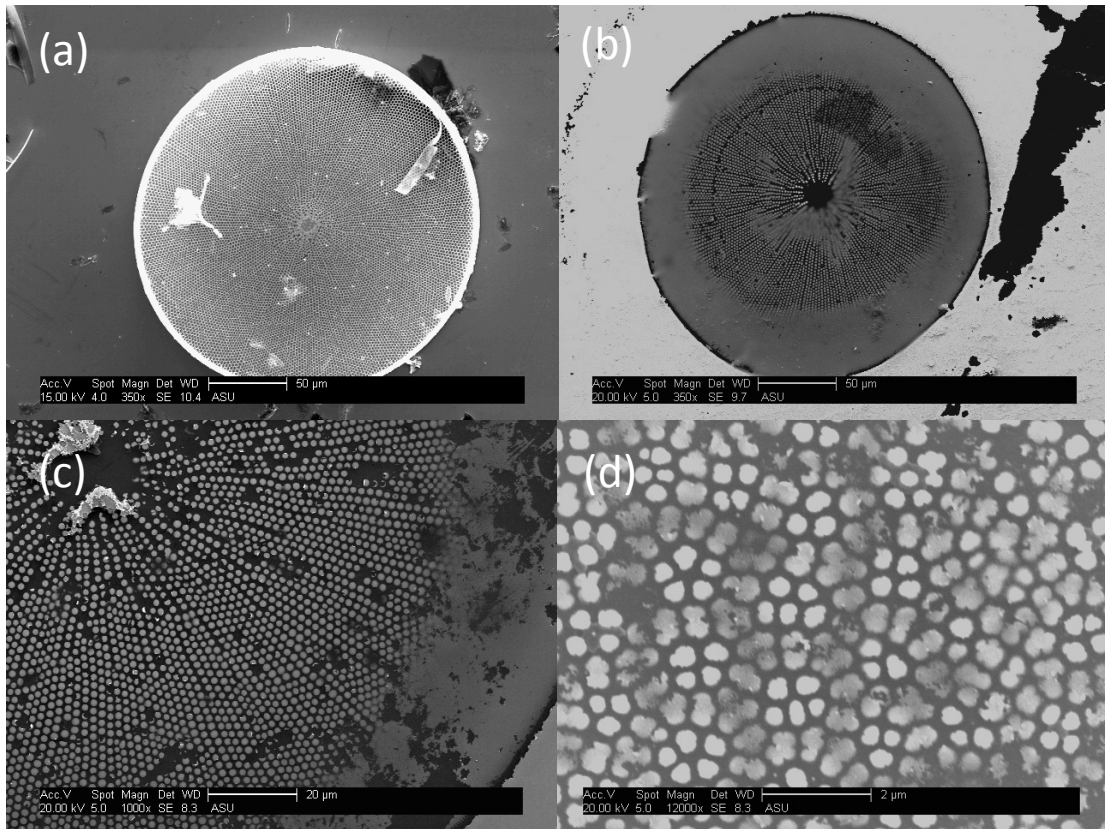


Figure 3-14 SEM images of diatom frustule and replica nano structures. (a) Diatom frustule was deposited on surface after gold sputter coating. (b) SEM images of corresponding gold replicas from whole diatom. (c-d) images with greater details with micro and nano patterns.

As seen from Figure 3-14(c) and 3-14(d), there are two different kinds of patterns depending on internal or external porous membrane layers of frustules which were used as templates. The typical size of micro patterns from Fig. 3-14(c) is in the range of 1-1.5 μm, and the size of nano patterns from Fig. 3-14(d) is between 250-300 nm. The SEM images of the gold replicas of corresponding sections of the external diatom membrane are shown in Fig. 3-15. It is obvious that the size, shape and organization of gold

structures represent the negative of the porous frustule used as the template. The average cribrum pore size from diatom frustule is 284 ± 39 nm, and average size of gold replicas is 274 ± 56 nm, with the spacing 100 ± 17 nm. It is evident from the corresponding images that these small gold structures are conformal with the template pores.

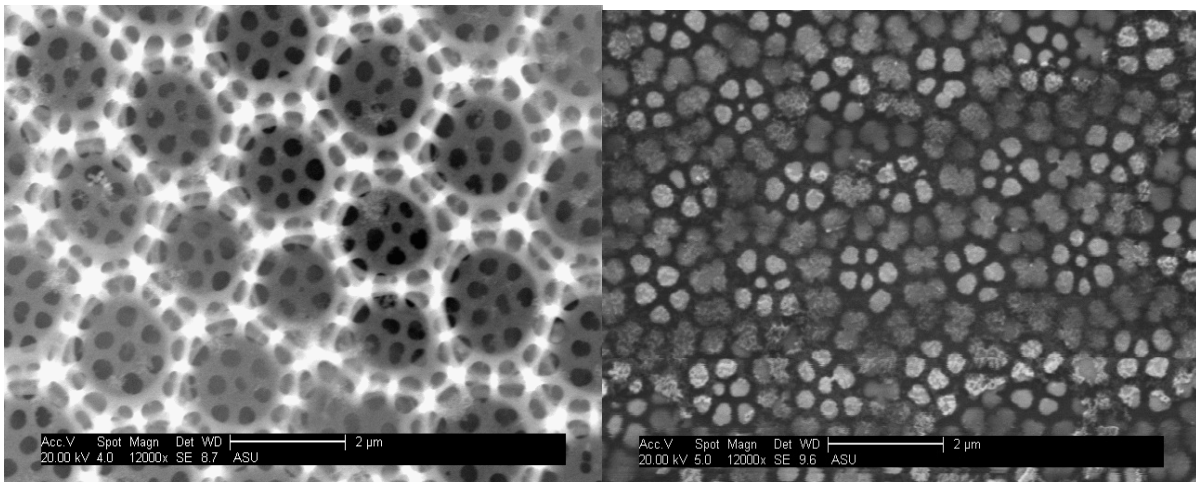


Figure 3-15 SEM images of the external frustule membrane of *Coscinodiscus sp.* used as template with corresponding gold replicas.

Fig. 3-16 shows the gold replicas of corresponding sections of the internal diatom membrane. The average areola pore size from diatom frustule is 1.265 ± 0.113 μm , and average size of gold replicas is 1.245 ± 0.132 μm .

It has been demonstrated that patterns can be fabricated as small as hundred nanometers to several micrometers with high yield by combining a lift-off process with a sputter coating deposition process.

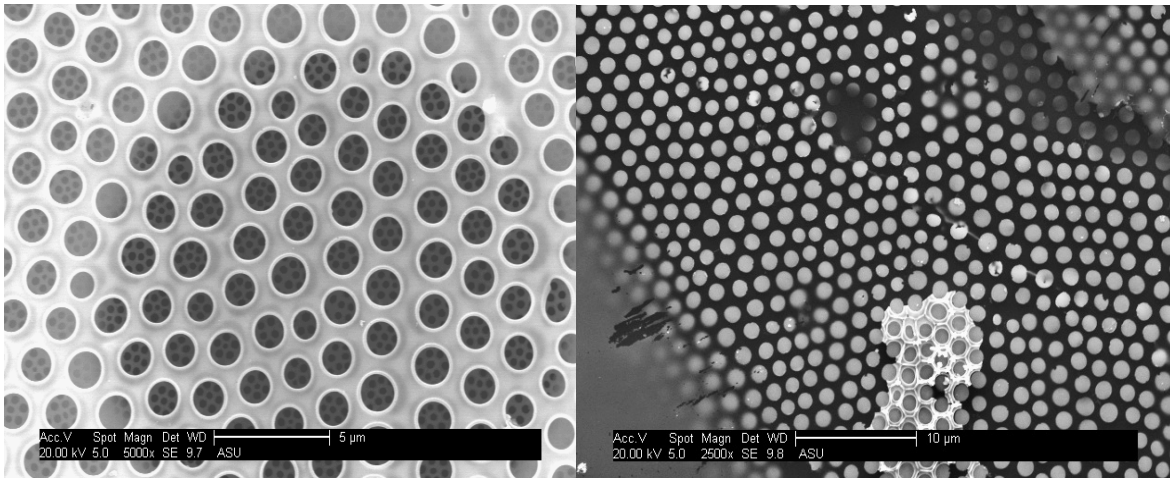


Figure 3-16 SEM images of the internal frustule membrane of *Coscinodiscus sp.* used as template with corresponding gold replicas.

The AFM images obtained of the gold replica fabricated from corresponding parts of the frustule are shown in Fig. 3-17. These images show ~250 nm sized gold patterns, which correspond to the main pores of cribrum (second layer in the template). The height of these nano patterns ranges from 20 to 25 nm determined by AFM measurement, which depends on the sputter deposition time. The thickness of gold thin film can be controlled by the deposition time of sputter coating to get 30 nm height gold nano structures.

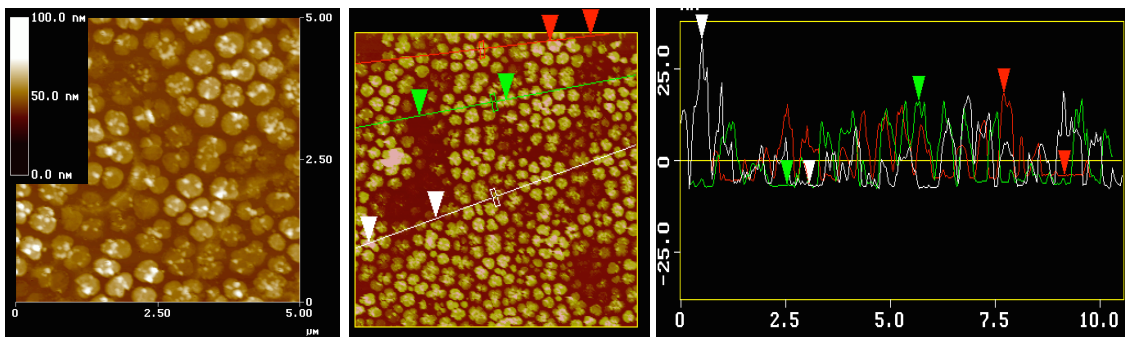


Figure 3-17 AFM images of gold structures replicated from cribrum membrane with profile graph showing the height of the gold nano structures.

This fabrication process is important for many reasons and has two types of advantages- one from the technique and the other arising from templates. First the advantages of technique: A) The process is very simple, straightforward, and easily reproducible. B) Sputter coating deposition is used extensively in the semiconductor industry, and sputter coater is also common for sample preparation for standard SEM imaging. C) It can also be performed with different deposition techniques and metals, depending on various desired application, such as thermal evaporation. Second, the advantages of templates: A) Given that there are over 100,000 different species diatoms, one can create thousands of structurally unique structures and pore sizes as templates [4]. B) The pattern can be tailored by choosing specific species with unique size and patterns to fit the needs. C) The resulting patterns exhibit periodic structural details, including nanometer sized patterns (Fig. 3-14d).

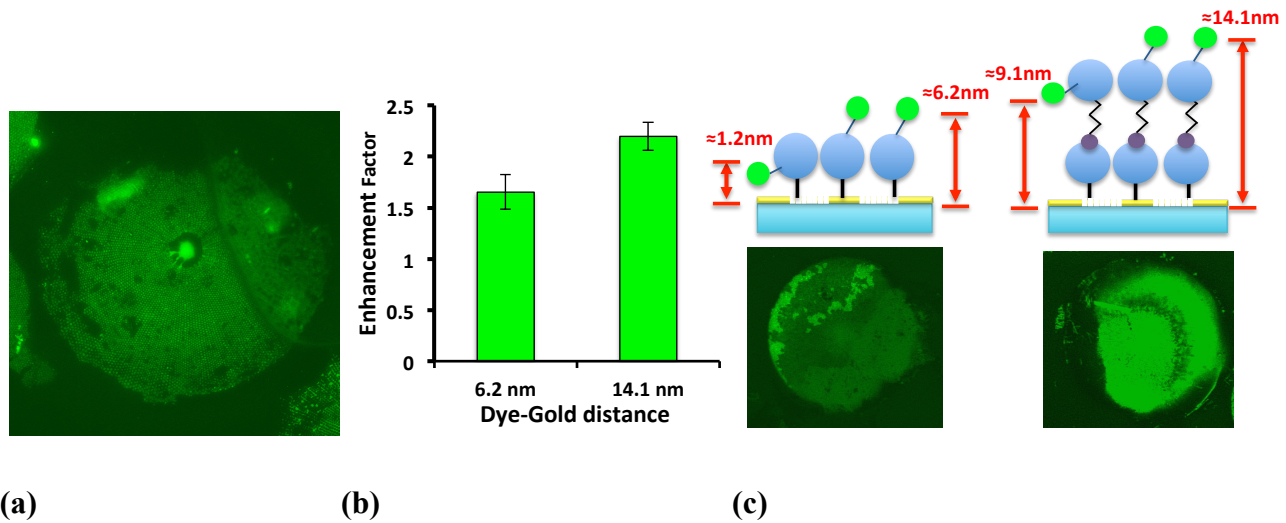


Figure 3-18 (a) Fluorescence image of Alexa Fluor® 488 on gold replica from diatom. (b) Enhancement factors of the Alexa Fluor® 488 with different dye-gold distance. Alexa Fluor® 488 are attached onto either gold nano structures or planar gold substrates. Enhancement factors were calculated by dividing the value from Alexa Fluor® 488 on gold replica by that from Alexa Fluor® 488 on planar gold. (c) Schematic illustration the distance from Alexa Fluor® 488 to surface.

It is believed that the present work is the first reported study of using diatom-templated nanostructure to study metal-enhanced fluorescence.

One of the main goals of this research is to demonstrate that the diatom-templated nanostructure surface can be used as MEF substrates; in other words, the fluorescence enhancement will be obtained on the diatom-templated nanostructure surface. The fluorescence images of Alexa Fluor® 488 on the gold nanostructure substrates are given in Figure 3-18a. The fluorescence images for this dye have demonstrated that, depending on the location of dyes, the fluorescence was either unaffected or enhanced in comparison to the controls, in which fluorescence was due to the Alexa Fluor® 488 located on the planar gold surfaces. The intensity of fluorescence was measured from the planar gold surfaces, and from the nanostructure from diatom frustule. The intensity of nanostructure divided by the intensity of planar gold (i.e., the ratio) gave the enhancement factor. The definition of enhancement factor is different from other groups [108, 110] where they used the intensity on glass or SiO₂ substrate as reference. In our approach, the gold was deposited on whole surface, so the planar gold surface is our reference to calculate enhancement factor. From Fig. 3-18b, diatom-templated gold nanostructure surface produced an enhancement factor of 1.65 at 6.2 nm dye-gold distance. The enhancement effect observed on the gold nanostructure could be result from interactions of the excited-state fluorophores with free electrons in the metal, the so-called surface plasmon electrons. [110] However, there is another fluorophore quenching effect at this short distances (~0-5 nm). From Fig. 3-18c, the shortest distance between dyes to the gold surface is only 1.2 nm, which may cause fluorophore quenched. The energy transfers from the fluorophores to the metal surface due to a coupling between the fluorophores

and the plasmon polariton at the surface of the metal. When the distance increasing, EM field amplification takes responsible for the fluorescence intensity enhancement at this distance range (~5-15 nm).

In order to examine the fluorescence enhancement at longer distance between the gold surface and the fluorescent dyes, the spacer had been added between dye and surface. Figure 3-18c schematically depicts the immobilization of Alexa Fluor® 488 at well-defined distances on gold nano patterns using DSP, streptavidin and NHS-PEG₄-Biotin. Two different assembly procedures are described in the Experimental Section and Figure 3-13. The appropriate size and height of the building blocks by DSP was 1.2 nm, streptavidin was 5 nm, and NHS-PEG₄-Biotin was 2.9 nm. The NHS groups on the gold film will react with primary amino group from streptavidin. However, it is difficult to predict the exact position of amino group on the streptavidin surface. But it can be assumed that the shortest distance between conjugated dye and gold surface is 1.2 nm, which is the length of DSP, and the longest distance of that is 6.2 nm, which is the summation of the length of DSP, and streptavidin. The average distance is 3.7 nm. For the second configuration, the only difference is adding streptavidin and NHS-PEG₄-Biotin. The shortest and longest distance becomes 9.1 nm and 14.1 nm, and the average is 11.6 nm. These separations positioned the Alexa Fluor® 488 at two different spatial locations in the range of 1.2 nm to 6.2 nm and 9.1 nm to 14.1 nm respectively. These ranges are within the amplified local EM field of gold nanostructures. From Fig. 3-18c, the enhanced fluorescence can be clearly compared side by side at two dye-surface distances. The enhancement factor is 1.65 for 6.2 nm dye-gold distance. When the dye-

gold distance changed to 14.1 nm, the enhancement factor becomes to 2.2. One can observe the difference of fluorescence intensity distinctively from fig. 3-18c.

These data suggest that the fluorescence quenching effect takes responsible for the fluorescence intensity in such short range (<5 nm). The energy transfers from the fluorophores to the metal surface due to a coupling between the fluorophores and the plasmon polariton at the surface of the metal. When the distance increasing, EM field amplification takes responsible for the fluorescence intensity enhancement at the range between 5 and 15 nm. Fluorophores are excited with an external light source and the energy from the electronically excited states (fluorescence emission) is partially transferred (coupled) to surface plasmons in metals. The surface plasmons are the free electrons in metals which collectively oscillate at frequencies similar to light.

Subsequently, light at visible spectral range can induce the surface plasmons. Since the wavelength of fluorescence emission and the surface plasmons overlap, the excited state energy of fluorophores species can be coupled to surface plasmons.

The other metal-enhanced fluorescence platforms have also been reported. Zin's group had developed template-guided immobilization of protein-functionalized QDs at well-defined distances on plasmon resonant gold nanoarrays using designed peptides and protein spacers. [104] They observed the enhancement factor for 200 nm gold arrays with 150 nm spacing for QD emission was ~ 3 at QD-gold distance ~ 16 nm. This result is comparable to our data that the average size of gold nanopatterns is 274 ± 56 nm, with

the spacing 100 ± 17 nm. When fluorescence dye were placed on top of the gold nanopatterns surface at distance ~ 11.6 nm, the enhancement factor is ~ 2.2 .

The localized surface-plasmon resonance (LSPR) peak of 200 nm gold arrays with 150 nm spacing is 549.0 nm. [104] The LSPR data from other group also have similar results. Petrou's group observed strong absorption with a peak close to 560 nm wavelength for 180 nm gold arrays with 270 nm spacing. [120] These data suggest the LSPR peak of ~ 200 nm gold nanopatterns ranging from 549 nm to 560 nm wavelength. This range overlaps the fluorescence emission of Alexa-488, where the emission peak is at 515 nm with 36 nm FWHM, suggesting the excited state energy of fluorophores can be coupled to surface plasmons. Their results can support the MEF enhancement from diatom-templated gold nanopatterns could be based on overlap of surface plasmons and fluorescence emission.

The advantages of the diatom-templated nanostructures for fluorescence enhancement therefore can be summarized as follows. First, the diatom frustules can be used as template to fabricate gold nanostructures by combining a sputter coating deposition and a lift-off process. Diatoms can be routinely grown in laboratory conditions and it also provides a cheap resource to a huge number of preferred templates. Hence, the fluorescence enhancement substrate can be made rapidly and very cost-effectively. Second, after modifying surface with few steps, the fluorescent dyes or labeled biomolecules can be attached to the surface of the substrates to achieve fluorescence enhancement. By increasing the distance between dye and gold surface, we can get the

enhancement factor larger than two. Third, the use of a diatom-templated nanostructure substrate in our approach suggests the simplicity for integrating into lab-on-chip sensor or microfluidic devices for fluorescence-based bioassay applications. However, for diatom-templated nano fabrication to become more established as a reliable approach, several limitations that exist will need to be overcome. As the diatom template technique is a relatively new approach, it still needs the high yield and precise controlled from other conventional fabrication methods. Especially the large-scale fabrication may be a critical issue because of a lack of enough quantities of purified diatom frustules. Additionally, because the exact mechanisms of formation of the porous patterns of diatom frustule are not yet fully understood, one has to invest a lot of time and effort to find out the appropriate patterns of diatom species for the purpose of application.

3.4 Conclusion

In conclusion, a straightforward fabrication method that employs diatoms as templates for the formation of gold nanostructure substrates is demonstrated. The method is very generic and can be used with different metals and desired diatom species to produce unique nanopatterned substrates. It has also been shown that the nanostructured surfaces of diatom-templated metallic materials could be used as useful MEF substrates. This substrate can enhance fluorescence signals up to 2.2 times compared to the planar gold substrate. Given its simple fabrication process and integrability with micro devices or microfluidics, this technology offers a new avenue for fluorescence-based bioassay and analysis.

CHAPTER 4

USING DIATOM NANOSTRUCTURES TO FABRICATE HYBRID PLATFORM

4.1 Introduction

Solid-state nanopore membranes with nanopore diameters ranging from tens to hundreds of nanometers are of significant interest for particle separation [58], cell-cell communication [52, 59, 60] and even molecule [61-63] and DNA translocation studies [64-67]. Anodized aluminum oxide (AAO) membranes are commercially available examples, but the membranes have to be thick (60 μm) to ensure mechanical stability of the film, resulting in slow diffusion rates for particle separation and cell-cell communication studies. Silicon nanopore membranes overcome the diffusion limitation by being significantly thinner (~ 300 nm). However, they are usually patterned by electron-beam lithography to accomplish pore diameters of 20-300 nm [68]. Other ultrathin silicon membranes (~ 10 nm) with 25 nm diameter pores that employ an ion-beam drilling process are well apt for molecule separation applications, but the manufacturing process is too slow to allow easy scale up [69]. Track-etched membrane technology is widely used for commercial membrane fabrication using hydrocarbon-based plastic materials and it has recently been applied to SiN membranes, showing the ability to achieve pores with diameters between 1.5 nm and 20 nm pores [121]; however, this nanopore fabrication method is limited to a low density per area. Thin nanopore membranes with short pores of a length of around 50 nm offer an advantage with respect to temporal and spatial resolution of particle and molecule translocation [49, 50].

Nanopore membranes with a high porosity offer the advantage of a high fluidic throughput [47, 48]. However, thin, highly porous membranes suffer from being mechanically fragile. Thus, most nanopore membranes are not an ideal platform for the desired application, since they have to strike a balance between porosity and mechanical stability. This difficulty has already been solved by nature: diatoms produce diverse three-dimensional nanoporous silica structures that exhibit high porosity while maintaining mechanical stability [18].

With diatoms size up to 250 μm in diameter, they are ideal candidates to be combined with existing devices featuring micron-sized structures, such as microfluidics. The advantages of diatom nanoporous cell walls will be taken on silicon substrate to form an integrated membrane platform.

In this chapter, the details of a microfabrication process flow will be presented for producing a hybrid planar micromachined system consisting of a biomineralized silica nanopore membrane combined with a single micropore through a silicon wafer. Silicon provides an ideal substrate because micropores can be precisely manufactured using photolithography and deep reactive ion etching and integrated with microfluidics and microelectronics. The frustules, while being mechanically stable by themselves, need to be supported by an underlying substrate that provides the interface to the microfluidic system. By placing the diatom frustules on the micromachined silicon chip latter can serve as the macroscopic support structure.

4.2 Materials And Methods

4.2.1 Fabrication Of Silicon Chip

The silicon support structure was prepared using 4" diameter, double-sided polished (DSP) Si (1 0 0) wafers with a thickness of 440 μm . The standard AZ 4620 resist was spun to a final thickness of 7.9 μm on one side of the substrate. The 100 μm diameter aperture was patterned on the OAI Model 808 high-resolution mask aligner and developed in AZ300MIF supplied by AZ Chemicals. Silicon etching was performed in a STS ICP Advanced Silicon Etcher, running a modified Bosch process with SF_6 for the etching and C_4F_8 for the passivation step [122, 123]. The 100 : 1 etch selectivity of silicon over the photoresist allowed the 100 μm diameter patterned region thinning to a final thickness of 40 μm after the etch (Fig. 4-1(a)). The process was tailored for fast etch with a perpendicular side wall profile, providing a slightly concave bottom profile of the recess. In a subsequent step, the through-wafer via aperture with a diameter of 20 μm or 30 μm was defined via the backside photolithography with AZ 3312 photo resist on the OAI 808 aligner. The Bosch process was employed again to create the through-wafer aperture (Fig. 4-1(b)). The micromachined silicon substrate was thermally oxidized to provide electrical insulation and an oxide surface for subsequent chemical modification (Fig. 4-1(c)). Next, SU-8 3025 UV-patternable negative tone epoxy resin was spun on the large recess side and exposed to open up the recess structure (Fig. 4-1(d)). The 40 μm thick epoxy layer reduces the capacitance of the silicon chip in a fluidic cell, thereby reducing the electrical noise originating from the setup. The wafer was then diced into 10 mm x 10 mm individual pieces each holding a single aperture.

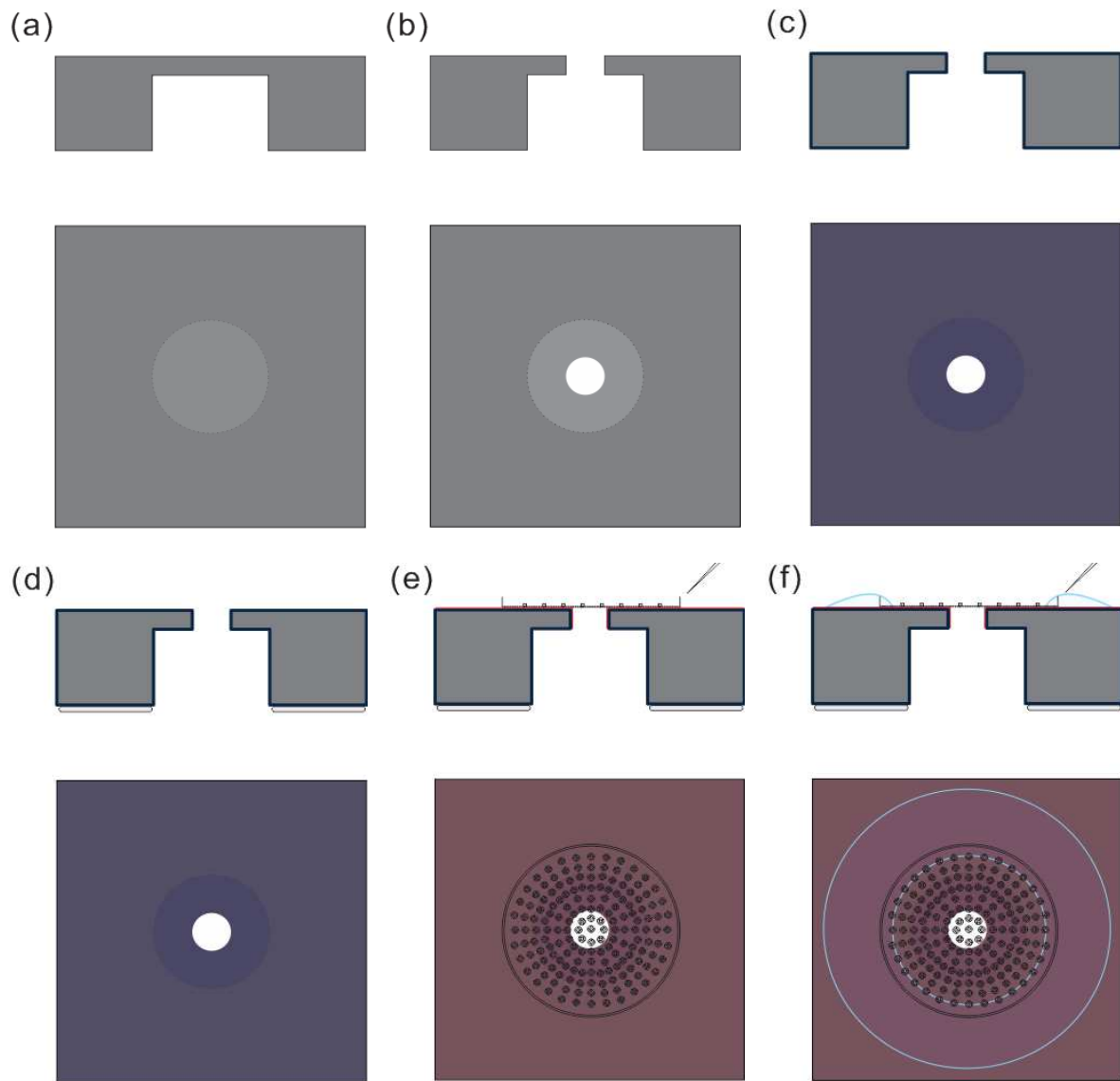


Figure 4-1 The bisector cross-section (top) and top (bottom) views of near aperture part of the diatom nanopore membrane device. (a) Using photolithography and a deep silicon etch process, a 0.1mm recess is etched into one side of a silicon support substrate. (b) A 20 μm or 30 μm diameter aperture is etched through the center of the recessed region by backside alignment techniques and the same etch process (c) The surface is thermally oxidized. (d) A noise reducing 40 μm thick SU-8 layer is patterned on the backside of the substrate. (e) A diatom frustule is positioned on top of a silicon aperture using a micromanipulator. The red poly-L-lysine layer which is dried from 0.1% poly-L-lysine solution generates electrostatically charge linkage. (f) The UV curable epoxy resin NOA-60 is applied surround the diatom by mechanical micromanipulator to stabilize the diatom frustule on the silicon substrate by the cross-linking of the resin.

4.2.2 Diatom Placement

4.2.2.1 Manually Placement

Upon a single silicon die with one micro-aperture, the diatom frustules of *Coscinodiscus wailesii* suspended in a water-ethanol solution were placed using a micropipette and the solution was allowed to spread into a thin layer. A mechanical micromanipulator (KRN-09 Positioner, J MicroTechnology, USA) was used to move one of the diatom frustules suspended in solution on top of the micromachined through wafer via aperture. The diatom frustule was positioned such that the outer surface of the porous plate, which has the nanoscale pores, is in contact with the silicon dioxide surface. During the drying step, the frustule adhered to the silicon dioxide surface and the addition of 0.1% poly-L-lysine solution resulted in electrostatically charge linkage (Fig. 4-1(e)).

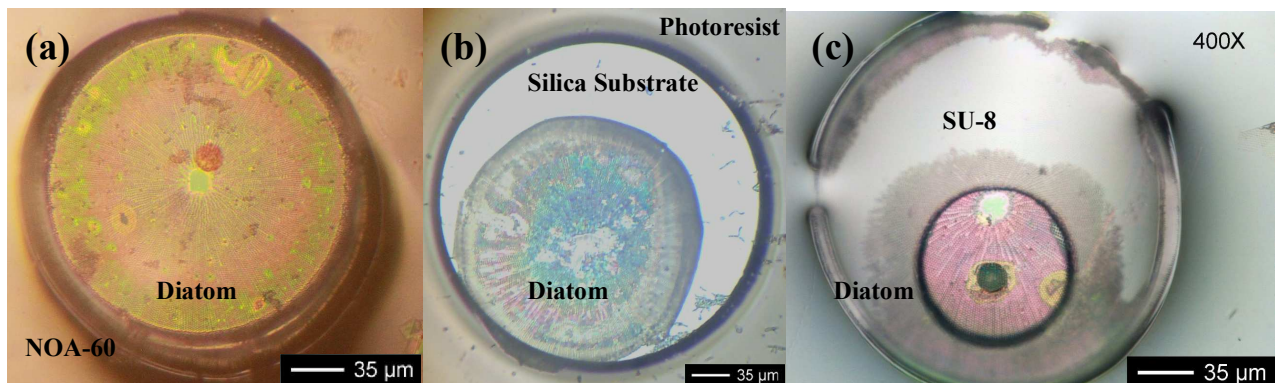


Figure 4-2 (a) The optical micrograph shows a diatom frustule which has been immobilized using poly-L-lysine. The perimeter of the diatom was subsequently sealed using UV-curable NOA-60 epoxy resin. (b) One diatom frustule adheres on the silica substrate within 8 μm high, 300 μm diameter circular photoresist groove. (c) Diatom frustule has been immobilized using SU-8. SU-8 has been removed in a ~ 100 μm area around the through – wafer via.

The optical image of diatom frustule positioned on top of a silicon aperture is shown in Fig. 4-2(a), where the silicon micropore is visible through the nanoporous membrane, indicating a free fluidic path through the diatom frustule. In order to provide enhanced stability in solution, the diatom was fixed on the silicon surface using a mechanically compliant UV curable epoxy resin (NOA-60) in addition to the charge linker. In this step, NOA-60 was applied around the diatom by mechanical micromanipulator, making sure that the center of the diatom was not accidentally coated (Fig. 4-1(f)). A subsequent flood exposure in ultraviolet (360-400 nm) resulted in cross-linking of the epoxy resin.

It is a delicate job to place diatom precisely on top of the through wafer via aperture.

First, one have to place diatom frustule on top of the chip in good contact. Because these centric diatom frustules are like petri dish, there are two ways for them to be placed on the surface. One is the ring of the petri dish sitting on the surface; another is the opposite way that whole plate of the petri dish is touching on the surface. Diatom frustules with the second configuration that the whole membrane is touching on the surface have to be used so that there is no gap between the silica surface and frustule membrane. In order to increase the possibility of diatom frustules sitting on the silica surface with whole plate, a thin layer of poly-L-lysine were coated on the silica surface. The silica surface carries SiO^- group in the neutral buffer solution, so both silica chip and diatom frustules carry negative charges. If there is no linker like poly-L-lysine, diatom frustules prefer to land on chip with the ring sitting on the surface because of the electrostatic repulsive force between diatom frustules and silica surface. With the help from the linker of poly-L-lysine, the chances of diatom frustules sitting on silica surface with whole plate increase a

lot. After diatom frustules were precipitated on the silica surface, the mechanical micromanipulator was used to position one diatom frustule on top of the micromachined through wafer via aperture.

4.2.2.2 Self-Assembly Placement

An alternate approach was devised based on patterning methods found in the literature by a high wettability contrast between hydrophilic bonding areas and hydrophobic surrounding areas on the wafers [124, 125]. The substrate was patterned into hydrophilic and hydrophobic areas using photoresist AZ 4620. The areas where photoresist was present were rendered hydrophobic and areas where the resist was removed by lithography where silicon dioxide surface was exposed were hydrophilic. The hydrophilic diatom frustules, when dispersed in a polar solvent such as water, adhered only to the hydrophilic spots. The 8 μm high, 300 μm diameter circular photoresist grooves ensured the placement of one 200 μm diameter diatom frustule on the pore of the silica substrate (fig. 4-2(b)). The silicon dioxide surface areas were coated with 0.1% poly-L-lysine solution resulted in charge linkage. The electrostatic force is strong enough that the adhered diatoms were not washed away during the acetone lift-off. Once the diatom was temporarily bonded to the chip with poly-L-lysine, a 5 μm thick SU-8 3005 was spun onto the diatom-silica chip. A slow multi-ramp process was used to pre-bake the sample to prevent the SU-8 from forming bubbles at the surface and cracking of the diatom due to stress during curing. Exposure was completed with a mask consisting of a 100 μm diameter chrome dot that was positioned over the 20 μm pore but within the

circumference of 200 μm diameter diatom (Fig 4-2(c)). After a 2 hour post-exposure bake to speed up the cross-linking of SU-8, the chip was developed in SU-8 developer for two minutes and rinsed with iso-propyl alcohol. The immobilization process was completed by placing the diatom chip in a 3:1 mixture of sulfuric acid and hydrogen peroxide for two minutes to ensure clog-free pores. This ensures the presence of unclogged pores in the diatom frustule.

4.2.3 Electrical Characterization

A variety of electrical test were conducted to characterize the nanopores on diatom frustules when they were filled with electrolyte. The silicon chip with the attached diatom frustule was mounted vertically in a Teflon holder. The holder sealed against the chip using O-rings. The holder provides fluidic access to either side of the chip with a fluidic bath volume of 3 ml. Electrical connection to the fluidic baths was made via Ag/AgCl wire electrodes. The electrodes were connected to a HEKA EPC-8 patch-clamp transimpedance amplifier operating in voltage clamp mode with the Bessel filter set at 1 kHz or 5 kHz cut-off frequency to limit the high-frequency noise. The nanopore resistance was derived from the slope of the current-voltage (I-V) response. Steady-state current was measured by applying a voltage within the range of -400 to 400 mV across the diatom frustule. The current was recorded using a National Instruments PCIe-6251 Data Acquisition board at 10 kHz or 50 kHz sampling rate. The recording was controlled using the WinEDR software package developed at the University of Strathclyde.

4.3 Results and Discussion

4.3.1 Hybrid Platform Structure Characteristics

The main goal of this research was to demonstrate that this hybrid platform combining a diatom frustule with a silicon chip could be used as a lab on chip device for low noise measurements of electrochemical signatures such as pore conductance and impedance spectroscopy. Cylindrical micropore channel has been fabricated using standard microelectronic fabrication techniques as described in Section II. A cross-sectional SEM image of a single micropore after microfabrication is shown in Fig. 4-3(a).

A 100 μm diameter recess was etched into the backside of silicon substrate to a final 40 μm thickness, with a 30 μm through-wafer aperture at center. The surface is thermally oxidized to provide electrical insulation, and the backside of silicon substrate was coated with 40 μm of SU-8 to reduce noise. A diatom frustule is placed on top of the silicon aperture and was fixed on the silicon substrate by UV-curable epoxy resin (Fig. 4-2(a)).

The diameter of diatom frustule is around 250 μm so that can cover the micropore of the silicon substrate. Fig. 4-3(b)-(d) show a series of SEM images of *Coscinodiscus wailesii* frustule. Fig. 4-3(b) shows the whole frustule with intact valve settled on the substrate exposing their exterior surface (convex). In our platform, this exterior surface is in contact with the silicon substrate, providing maximum contact area between the frustule and the surface.

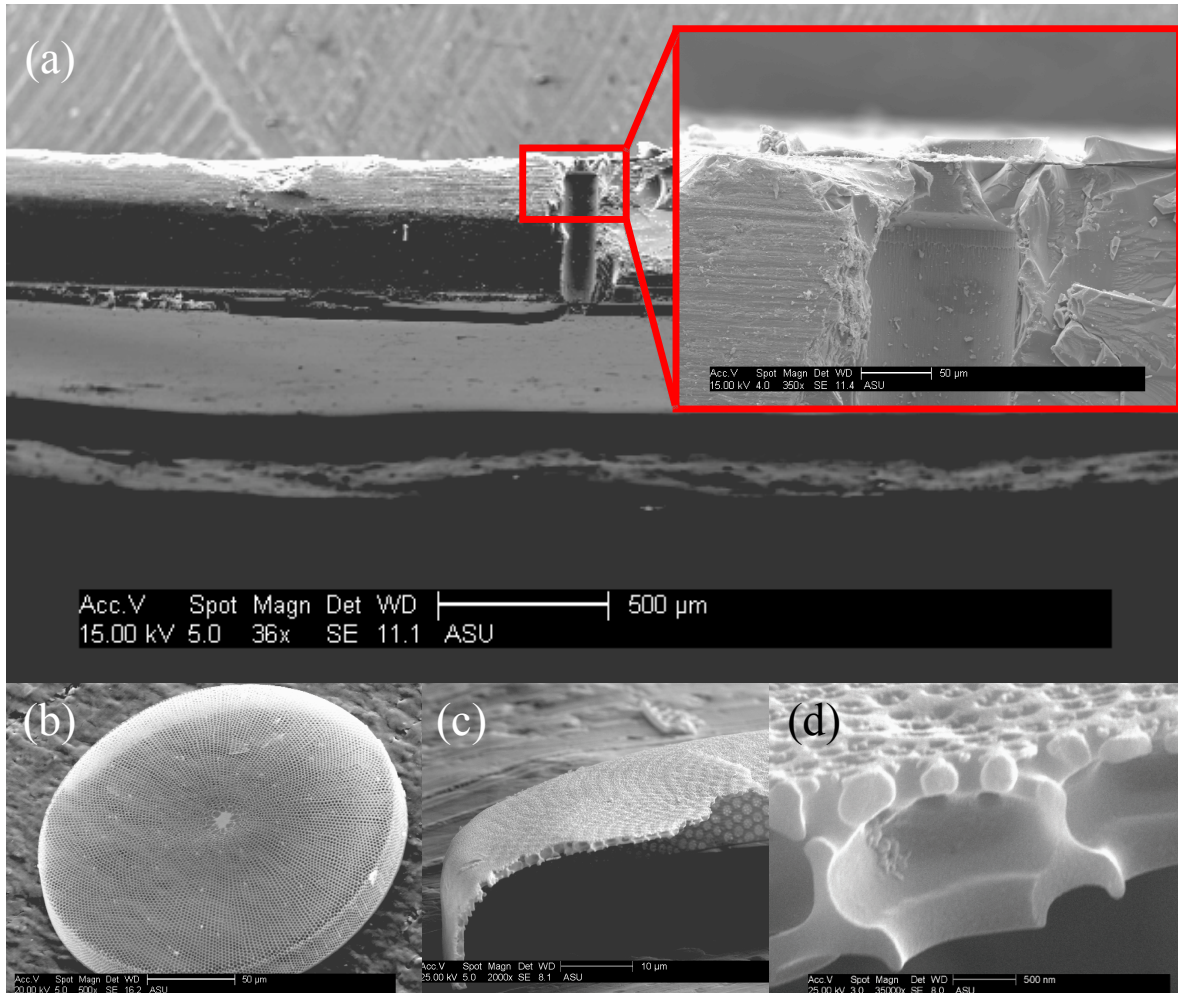


Figure 4-3 (a) Cross-sectional scanning electron micrograph of micropore after completion of the fabrication sequence with a diatom frustule mounted on top of it. (b) The whole frustule with intact valve settled on the substrate exposing their exterior surface (convex), and (c) the cross-sectional SEM image shows the profile structure of the frustule, the higher magnification image in (d) shows the details of the three porous layers hierarchical structure.

The cross-section SEM image shows the profile structure of the frustule (Fig. 4-3(c)), and the higher magnification image in Fig. 4-3(d) shows the details of the three porous layers hierarchical structure. The outer porous layer containing the smallest pores with the pore diameter is determined as 45 ± 9 nm [15], and the thickness of this layer is less than 50 nm. This layer plays an important role as a selective membrane in contact with the

environment to uptake nutrient and to defend against bacterial and viral attack [15]. The second porous layer is connected to the internal (third) porous silica plate. The pores diameter in the second layer range from 200 nm to 250 nm and are overlaid with the first layer pore arrays. The thickness of second layer is around 250 nm that is comparatively thicker than the first layer. It is possible that thick silica plate of second layer is responsible for the mechanical stability to support the first thin layer for filtration and separation. The third porous (internal) layer with pore diameter around 1 μm also provides the support to the second layer for the mechanical stability. The thickness of this integrated multilayer porous membrane is range from 1 to 1.5 μm . This hybrid platform gives us the advantages of high volume manufacturing precisely from silicon substrate and high porosity and thin, mechanical stable nanopore membrane for high fluid throughput from diatom frustule.

4.3.2 Hybrid Platform Electrical Characterization

The preliminary conductivity measurements of hybrid platform in KCl solution have been completed for characterization purposes. Prior to making measurements, the dry nanopores on diatom membrane must be filled. To fill nanopores with water, it is immersed in the deionized water for up to 8 hours. The initial condition of the device is filled with deionized water and it is the minimum conduction state, and KCl sweeps were completed from lowest concentration to the highest. Fig. 4-4(a) shows the I-V traces of a hybrid platform for various KCl concentrations at 1 mM, 10 mM, 50 mM, and 100

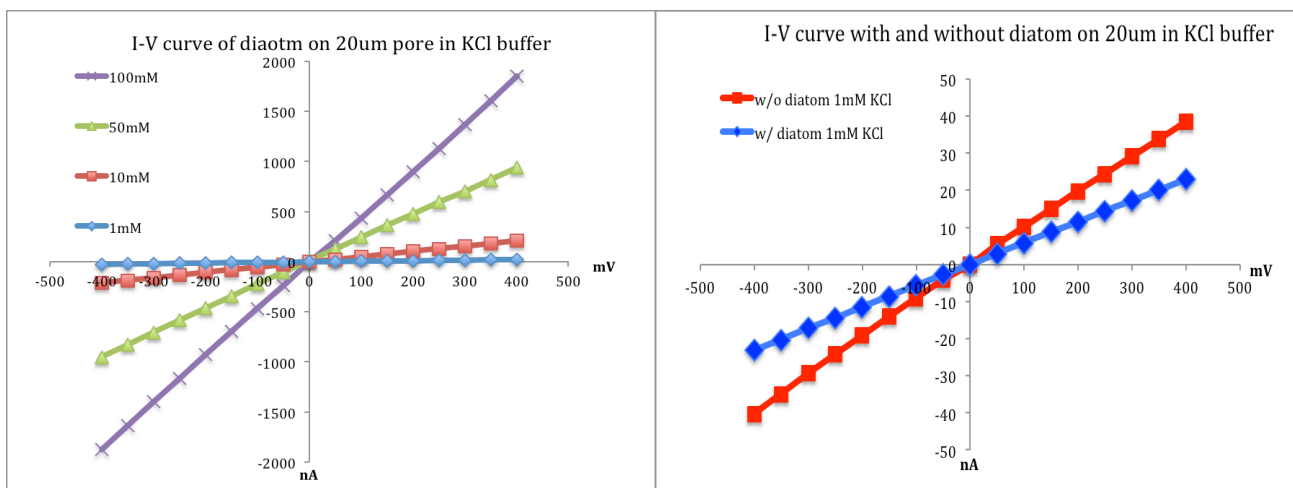


Figure 4-4 (a) The I-V curves of a hybrid platform for various KCl concentrations at 1 mM, 10 mM, 50 mM, and 100 mM. The applied voltage across the pores was held constant for 5 s each from -400 to 400 mV in 50 mV steps. (b) The I-V curve of the hybrid platform with and without the diatom in 1 mM KCl solution.

mM. The applied voltage across the pores was held constant for 5 s each from -400 to 400 mV in 50 mV steps.

The average current value was used to plot the I-V trace. The slopes of the lines correspond to the conductance of the diatom pores. Since the I-V relation is linear in this graph so that we can get conductance of the hybrid platform according to Ohm's law. It's also apparent that as the concentration of the KCl solution is increased, the conductance increases. For example, the conductance of the pores in 1mM KCl is 0.058 μS , and the conductance increases to 4.619 μS in 100 mM KCl.

In order to measure the influence of diatom frustule, the I-V curves of the platform with and without the diatom are also compared in. Fig. 4-4(b). The conductance decreased from 0.098 μS to 0.058 μS in 1mM KCl, which implies that when a diatom frustule was fixed on the silicon surface, the only one possible route for ions to travel between two

fluidic baths is through the nanopores of diatom. This finding proves our hypothesis that the transport is through the nanopores and not the perimeter of diatom.

The second set measurement to characterize the particles transport through the membrane pores have also been done. The fundamental of sensing particle through membrane pores is based on the concept of Coulter counter [126]. A device consists of two chambers containing an electrolyte solution and separated by one or few channels. When a particle enters through one of these channels, a change in electric current or voltage pulse is detected. In general situation, for a known single nanopore geometry the drop in current can be correlated to size, mobility, surface charge, and concentration of the particles passing through the pore. If nanoparticles move through the finest nanopores of diatom, then we should see a current reduction. According to the concept of Coulter counter, the size of particle can be calculated from a current reduction. However, the geometry of diatom nanopores is not perfect cylindrical and the pores size are not identical. Therefore, the magnitude of the current blockage could not be employed to estimate the size of particle. Although it is hard to estimate the size of the passing nanoparticle, we still can detect how many translocation events occur when we observe current reduction. And there are also some possible applications of this hybrid platform such as particle separations, cell-cell communication studies [43], and nanohole array based sensing [127]. In these scenarios, the size and shape of the nanopores is less importance compared to the number and order of the nanopores. The benefit of using biomineralized frustrules as nanopore membranes on silicon microstructures, effectively replacing thin silicon dioxide membranes structured using lithographic techniques is the extremely low

cost of the process while being able to have up to hundreds of nanopores accessible in the active area of the device.

4.4 Potential Applications

4.4.1 Nanoparticle Selection Through Pores Of A Diatom

In most research, individual nanopores are the preferred configuration when it comes to nanoparticle counting and sizing, since for a known nanopore geometry the drop in current can be directly associated with the size of the nanoparticle passing through the pore. Single pores, however have the significant disadvantage of a low throughput and the danger of failure once the single nanopore becomes irreversibly clogged. Arrays of nanopores are a solution to the problem of catastrophic failure of a nanoparticle sensor due to single pore clogging. While top-down manufacturing of nanopores allows precise tailoring of the pore size and geometry, nanopore arrays of 100 or more closely spaced nanopores typically require long serial patterning processes using electron-beam or ion beam sculpting. In many possible application scenarios, such as filtration and cell-cell communication studies, the size distribution of the nanopores is less of importance compared to the number and maximum diameter of the pores. In these cases the benefit of using biomineralized frustrules as nanopore membranes on silicon microstructures, effectively replacing thin silicon dioxide membranes structured using lithographic techniques is the extremely low cost of the process while being able to have up to 500 nanopores accessible in the active area of the device. For such a membrane to be useful in

applications, the integrity of the fluidic seal between the diatom frustule and the oxidized silicon surface were verified.

Our experiments exposing the chip with the mounted diatom frustule to deionized water, phosphate-buffered saline (PBS) and 1M potassium chloride solution showed no detachment of the frustule. Using a horizontally mounted chip, we checked for eventual leakage paths by testing the permeability of the diatom frustule to fluorescent polystyrene particles of 500 nm diameter. No translocation events were observed when using an epifluorescence microscope.

The next question to be addressed was if it was possible to record the passage of single nanoparticles through the nanopore membrane, using the assembled device as an electrofluidic particle counter and sizer. The amount of reduction in ionic current upon particle translocation can be described by the theory of Coulter counting that has been reported by DeBlois and Bean [126]. Translocation of a particle through a pore of similar size causes the cross section area to be reduced, which results in a drop in conductance which is given by the geometrical parameters of the pore and the particle. Assuming known pore geometry, the size of the beads can be determined. The reduction in current of a single cylindrical pore is then given by the ratio of the cube of the particle diameter and the product of length and the square of the pore diameter. DeBlois et al. [126] introduced a correction factor S

$$S = \left(1 - 0.8 \frac{d^3}{D^3}\right)^{-1}, \quad (1)$$

which is a function of particle diameter d , and pore diameter D , accounting for the crowding of the electric field lines around the particle inside the pore, resulting in the following relation:

$$\Delta I = I_0 S(d/D) \frac{d^3}{l \cdot D^2}, \quad (2)$$

with ΔI being the drop in current, I_0 the base line current without the particle blocking, and l the length of the cylindrical pore. If we assume that the current is limited by the nanopores, with a nanopore in the third tier of the hierarchical structure having a diameter of 40 nm and a length of 50 nm, we can determine the current through a single nanopore. Assuming cylindrical pore geometry, the base line current is given by:

$$I_0 = V \cdot \frac{\pi \cdot \sigma \cdot D^2}{4 \cdot (l + 0.8D)}. \quad (3)$$

However, the nanopores of diatom frustules are not perfect cylinder, and the size of nanopores is not identical either. It is difficult to estimate the particle size based on the current drop when particle traveling inside the nanopore.

From equation (3), we can calculate the theoretical current through a single nanopore by know conductivity, nanopore diameter, nanopore length, and applied voltage. The conductivity of 27 nm polystyrene beads in 1mM Potassium Hydroxide electrolytic solution is 243 $\mu\text{S/cm}$, and the diameter of a nanopore in the third tier of the hierarchical structure is 45 nm and the length is 50 nm. At 400mV transmembrane bias voltage V , a current through a single nanopore is calculated at 180 pA. Due to the sizes of nanopores in the third tier is determined as 45 \pm 9 nm [15], the currents through a single nanopore also range from 126 pA to 239 pA (Table 4-1). If there were a polystyrene bead of 27 nm

diameter in the nanopore, it would reduce the current by 42 pA in 45 nm nanopore. The current drop caused by the 27 nm polystyrene particle ranges from 36 pA to 58 pA based on the size of nanopores in the third tier as 45 \pm 9 nm. A dip of this amplitude is still distinguishable from the noise floor of the setup.

Table 4-1 Calculated current of single nanopore by different size at 400 mV

| Pore size | 36 nm | 45 nm | 54 nm |
|--|--------|--------|--------|
| Current of single nanopore | 126 pA | 180 pA | 239 pA |
| Reduced current caused by a 27 nm polystyrene bead | 58 pA | 42 pA | 36 pA |

The test had been examined by using a 1mM Potassium Hydroxide electrolytic solution at 400 mV transmembrane bias. In this test, 27 nm diameter polystyrene beads with negative charges were used. The drop in current corresponding to a single particle passing through a nanopore is 35 pA. Figure 4-5 shows the translocation events of polystyrene nanoparticles, visible as distinct drops in the transmembrane current.

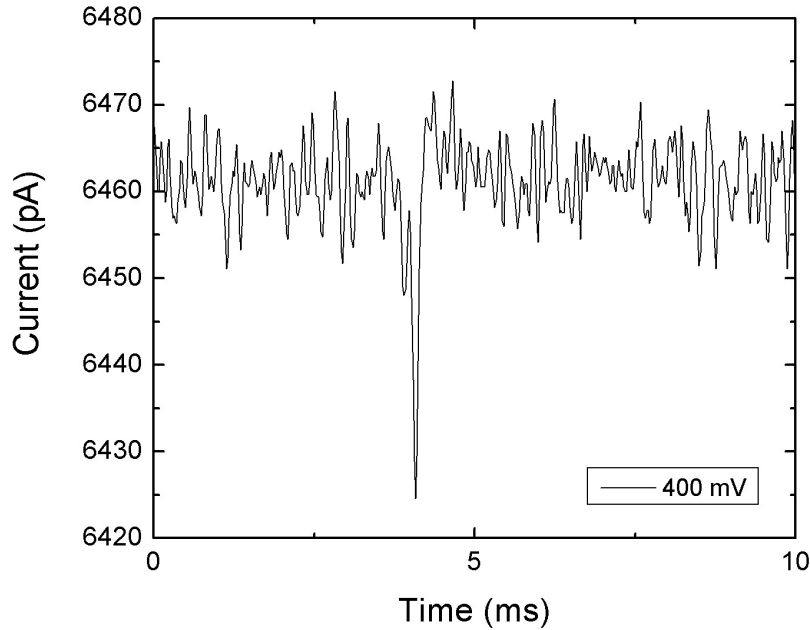


Figure 4-5 Ion current recording indicating translocation of 27 nm diameter polystyrene beads through the diatom nanopore membrane. The dwell time of these negatively charged particles is 0.6 ms. The drop in current corresponding to a single particle passing through a nanopore is ~35 pA.

Based on equation (2), the diameter of nanopore of diatom D can be calculated by the known I_0 , l and d , and the value of D is 55.6 nm, which is very close to the range of 45+/- 9 nm. However, it is difficult to estimate the particle size based on the current drop when particle traveling inside the nanopore, because the nanopores of diatom frustules are not perfect cylinder, and the size of nanopores is not identical either. For this reason, it cannot be used as Coulter counter or particle sizer. Although this platform cannot be used as Coulter counter, it still can be used as filter due to the arrays of nanopores that are a solution to prevent the catastrophic failure of a single pore clogging. It can keep particles size larger than 100 nm at one side, and allow smaller particles pass. The nanopore arrays of 100 or more closely spaced nanopores typically require long serial patterning

processes using electron-beam or ion beam sculpting and also are quite expensive. In the application of filtration and cell-cell communication studies, the size distribution and precision of the nanopores is less of importance compared to the number and maximum diameter of the pores. In these cases the benefit of using biomineralized frustrules as nanopore membranes on silicon microstructures, effectively replacing thin silicon dioxide membranes structured using lithographic techniques is the extremely low cost of the process.

4.4.2 Hybrid Silicon MEMS/Diatom Platform For The Cellular Response To Molecules

Nanoporous membranes are also very useful tools for cellular research. By growing cells in transwell where the chambers were separated by membrane into upper and lower compartments, one can maintain physical separation of the cells while still allowing soluble chemicals and nano particles to pass between chambers. This setup is useful to study the cell-cell communication, and the cell response from the chemicals. [52] The traditional membranes used in transwells are track-etched membranes, which are created by bombarding polycarbonate sheets with atomic particles, followed by chemical etching to open up holes along until pores are about 450 nm in diameter [128]. This pore size can prevent cell from migrating through the membranes, but still can allow chemicals or nano particles passing between compartments. However, the thickness of the track-etched membranes is $\sim 10 \mu\text{m}$ that results in the low permeability of the soluble chemicals. The hybrid silicon MEMS/diatom platform will be employed to address and observe certain populations of cells in a selective manner. The thickness of the thinner layer of

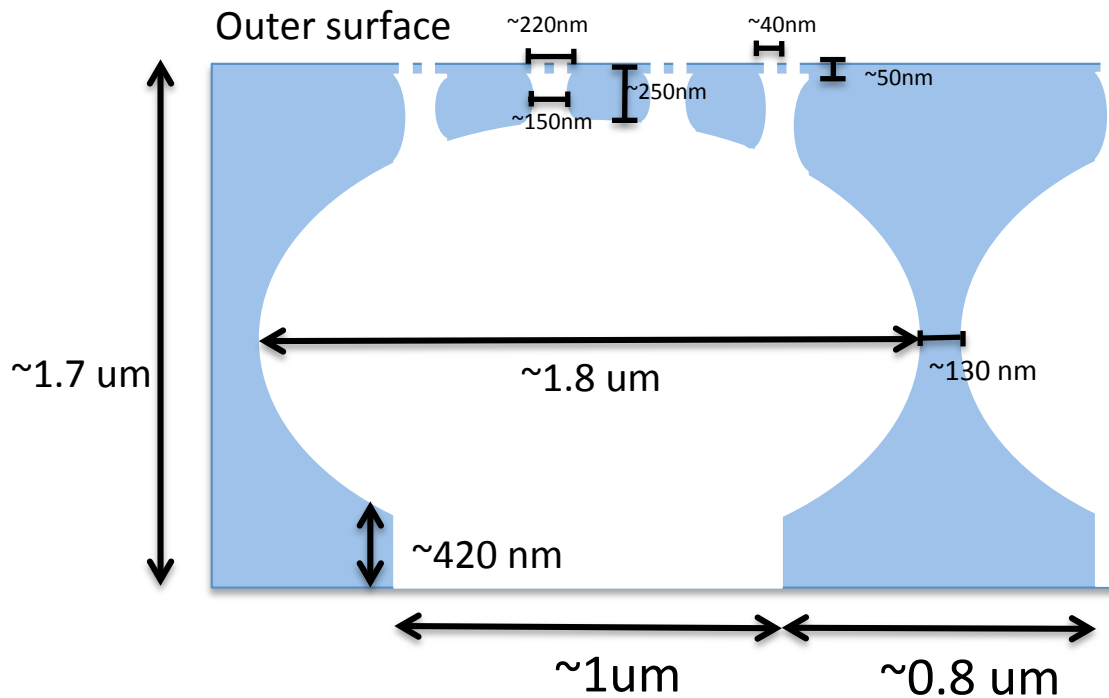


Figure 4-6 Schematic drawing (bottom) of the nanoporous layers of a diatom frustule (*Coscinodiscus wailesii*). The three-tier hierarchical pore structure is visible at the edge of the structure. This structure provides mechanical stability while maintaining high porosity on the nanoscale level.

diatom frustule is ~50 nm (Fig. 4-6), which is ~200 times thinner than commercial polymer membranes. One can expect the permeability will be orders of magnitude higher, and this hybrid MEMS/diatom platform will be expected to have values for cell culture. If different cell types can be grown on diatom frustule, then this platform can also be used as co-culture device to study cell-cell communication. Another possible application is that combine highly permeable membranes with microfluidic to enable time resolved studies of cellular responses to chemicals delivered with temporal and spatial control.

The prostate cancer cell and reporter cell lines were cultured directly on one side of MEMS/diatom platform to test the biocompatibility. Prostate cancer was used because it

is the sixth leading cause of cancer-related death in men and in the United States it is the second [129]. PC3, derived from human prostate cancer, were cultured at 37 C in a 5% CO₂, 90% humidified atmosphere and maintained in DMEM supplemented with 5% heat-inactivated fetal calf serum. 1×10^4 cells were seeded in each well of 24-well cell culture plates and allowed to attach overnight. The silicon chips with diatom mounted on the micropore were placed at the bottom of transwell (Fig. 4-7). After 48h incubation, optical images and fluorescence images were taken to check cell viability (Fig. 4-8).

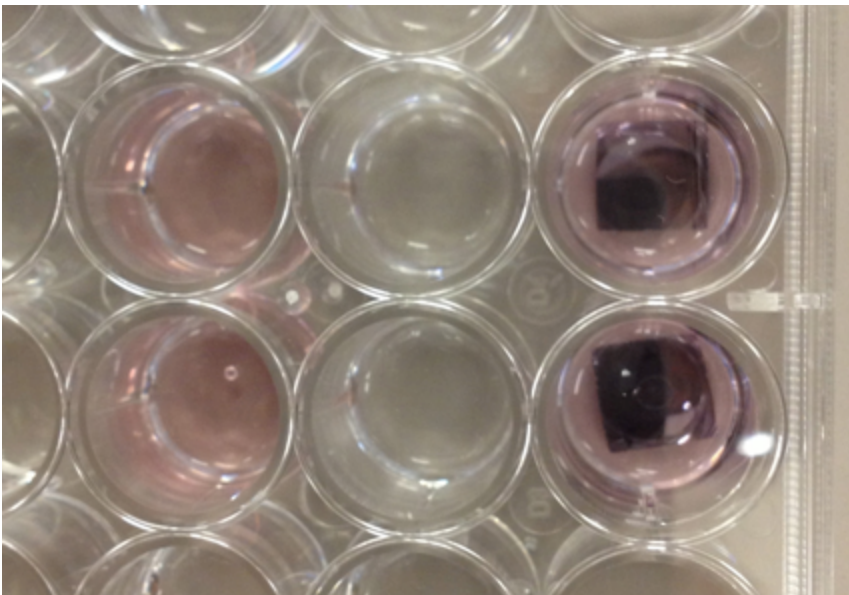


Figure 4-7 The silicon chips with diatom mounted on the micropore were placed at the bottom of transwell.

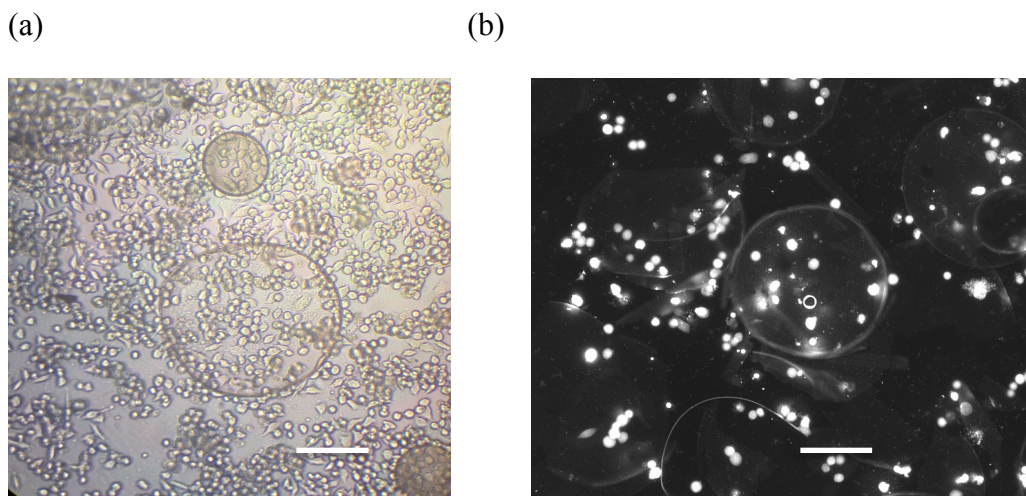


Figure 4-8 Cell spreading on silicon chip and diatom frustules. (a) Optical image captured after 48 hr incubation. (b) Fluorescence image show live cells after 48 hr incubation. Cell morphology was also normal. The 100 μ m scale bar applies to all images.

Cell viability on silicon surface and diatom frustule was examined by staining cells with live/dead fluorescent dyes in fluorescent images. A microscopy-based viability assay showed that after 2 days of culture, PC3 were viable on silicon and diatom frustule surface (Fig. 4-8), and the cell morphologies were normal.

There are a few roles that the nanostructures of the frustule can play in terms of facilitating filtration and sorting based on the type of flow the diatoms experience. In figure 4-9 shows the pore structure and the associated diffusion coefficients and concentration gradient taking into account the nanoscale confining effects [130]. Bhatta et al. did more detailed experiments showing the diffusion coefficient of small molecules like fluoresceine was reduced through a *Coscinodiscus* valve. [131] The diffusion coefficient of a fluorescent dye in a pore was shown to be reduced significantly relative

to the free solution value. This decrease due to confinement is shown schematically in Figure 4-9.

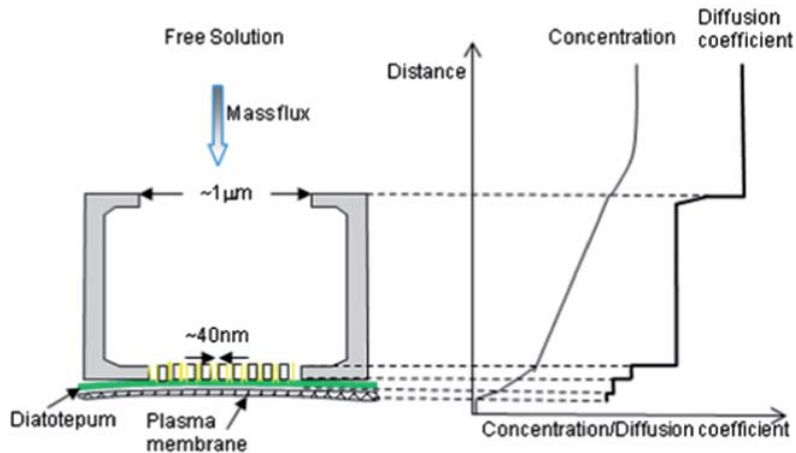


Figure 4-9 Schematic of a diatom valve pore structure (not to scale) and associated diffusion coefficients and concentration through the pore assuming pure diffusion and no advection. [130]

Moreover filtering may also utilize electrostatic interactions via the electric double layer or even Van de Waals forces. If the negatively charged silica frustule was exposed to in salt water with an ionic strength of 0.7 M, the Debye length would be very small relative to the pore size so that it would have little effect on the transport properties. However, with the surface modification, such as a very thin layer of polysaccharides, may change the interaction lengths. One can modify surface properties inside frustule pores to select transport molecules.

While different molecules, (e.g. dyes, drugs), and nanoparticles (e.g. quantum dots, gold nanorods) will be selectively released via microfluidic channels on the opposite side of the diatom membrane. Only cells cultured directly above the diatom surface will be exposed to small-molecule or nanoparticle treatments. This will allow us to interrogate

cellular response to drugs and imaging agents with a focus on how selective manipulation of certain cells influences the fate of surrounding cells (e.g. bystander effect). These studies will also allow us to determine spatial and temporal dependence of cellular microenvironment and probing cell-cell interactions as well as communication. The fluidic transport phenomena through well-characterized hierarchical nanopore structures towards designing hybrid devices for applications in separation, sensor and biomedical device technologies will also be addressed.

4.5 Conclusion

Single cylindrical micropore channels have been manufactured using standard MEMS microfabrication techniques. The diatom frustules have been mounted manually and self-assembled on the oxidized silicon support, and were adhered by poly-L-lysine and UV-curable epoxy, which renders them stable in aqueous solutions. By combining biomineralized nanoporous structures with microfabricated silicon supports, the hybrid platform is workable. The electrical conductance of the hybrid platform has been measured for different KCl electrolyte concentrations. The I-V curves were linear and the slopes of these curves give the conductance of the diatom nanopores according to Ohm's law. This platform also can be used for nanoparticle filtration, translocation detection, featuring high solution throughput, and a low probability for complete clogging. In addition, the small nanopores of diatom frustules are ideally suited for measurements of ion channels that cross lipid membranes which are suspended across the opening pores, and due to

diatom nanopore membrane is thinner than any polymeric membrane, thus lends itself to the application in cell-cell-communication.

CHAPTER 5

USING CONCEPT MAPS TO TEACH NANO SCIENCE AND TECHNOLOGY

5.1 Introduction

In recent years, nano science and technology have attracted interests not only from scientists/engineers but also from the general public. A concept map is a method of representing relationships between ideas, concepts, images, and words. The goal of our efforts to construct concept maps of nano science and technology is to integrate research, education, workforce development and outreach in a meaningful way. The target audiences are teachers and students of grades 7-14 as this is a critical stage for students to plan their career pathways. Using concept maps can help and motivate students to ask questions and explore the key concepts. It also helps students to develop logical thinking when they construct maps.

5.2 What Is Concept Map?

Concept mapping is a technique of visually representing the concepts, their hierarchy and their interconnections. This graphical tool for organizing and representing knowledge was originally developed by Prof. Joseph D. Novak [132] in the late 1960s and early 1970s. Novak outlined the potential uses of concept mapping for the improvement of learning and teaching in science classrooms. These potential uses can be itemized into four categories: (a) as a learning strategy, (b) as an instructional strategy, (c) as a plan curriculum, and (d) as a means of assessing students' understanding of science concepts. Concept mapping tasks have been used in a variety of ways in science and engineering education [133, 134]. This chapter is focused on the strategy for a planning curriculum for teachers, providing a good resource for high school and undergraduate level teachers.

The definition from Novak is a perceived regularity in events or objects, designated by a label, and propositions contain two or more concepts connected using linking words or phrases to form a meaningful statement [135]. There are different components in concept map including: (1) nodes, (2) links, (3) labels, and (4) propositions. Nodes represent concepts, links (or lines) represent relationships between concepts, labels are the linking words signify the relationships between two linked concepts, and propositions are meaningful statements with two or more linked concepts.

Based on the structure, concept map can be divided into two types. One is a hierarchically structured concept map: more general concepts on top, and then break down into sub-concepts or into specific ideas. Figure 5-1 shows a complex example. The hierarchically structured concept maps could also be treated as a thought map, which is used to organize data and represent ideas and relationships as node-link diagrams. It implies taking a list of ideas, events, objects, or tasks, and organizing them in a graphic illustration with ideas and linking propositions.

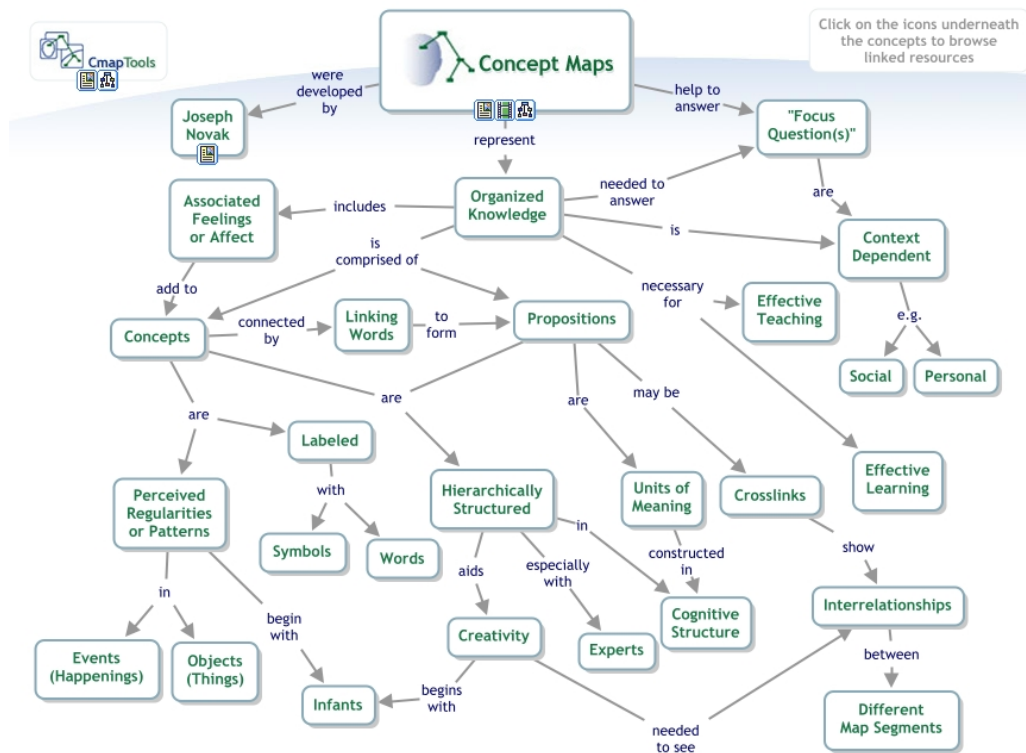


Figure 5-1 An example of hierarchically structured concept map. Source: <http://goo.gl/F96qeb>

The other one is semantic networks map (or mind map), which forms a network with no hierarchical structure. A central concept is at the center of the graphic map and other concepts drawn in a radial way around the central concept. Figure 5-2 is an example of semantic network on Mind map.

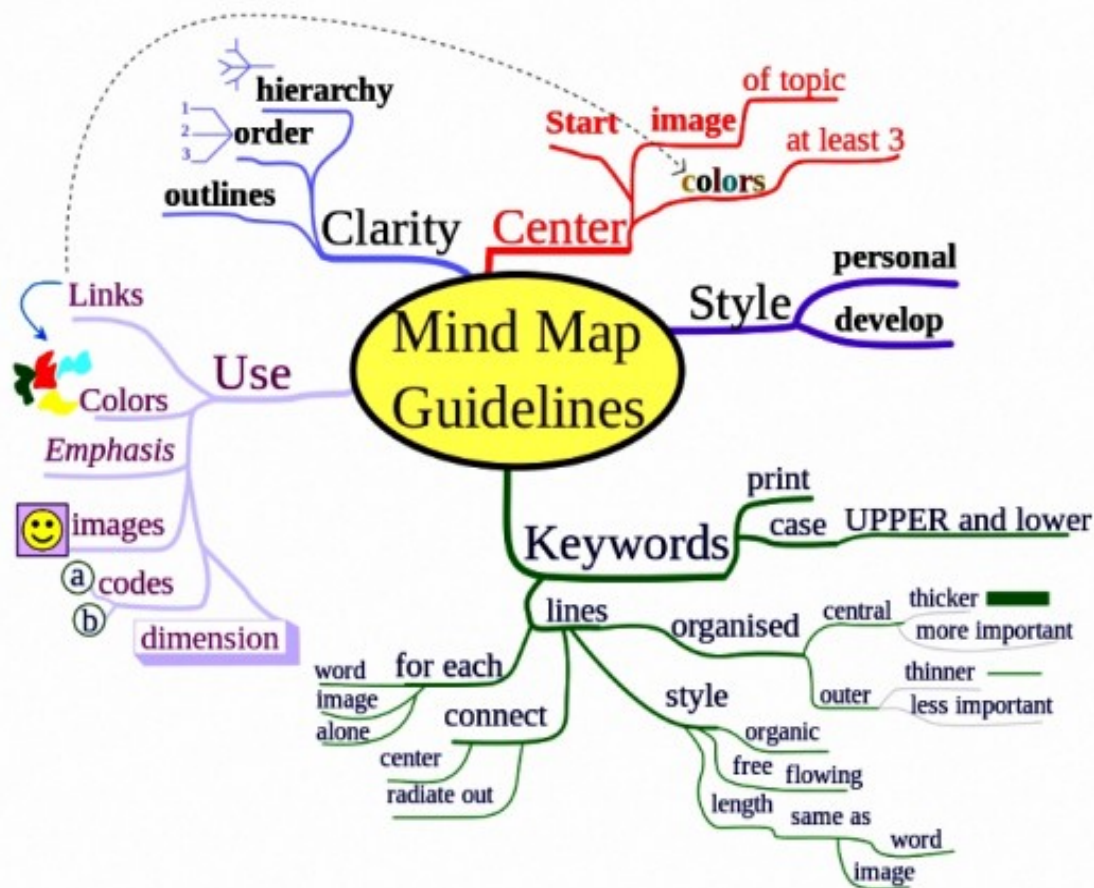


Figure 5-2 An example of semantic network of mind map. Source: <http://commons.wikimedia.org/wiki/File%3AMindMapGuidelines.svg>

The biggest distinction between thought maps and mind maps is that a mind map tends to possess one main thought, whereas a thought map might have many connected and interconnecting concepts, themes or topics [136]. So a mind map usually looks like a tree, whereas a thought map may have complicated networks to represent the concepts.

There are several benefits from the concept mapping exercise. It can help students brainstorm and generate new ideas, and communicate thoughts more clearly. It also encourages them to discover interconnections and even new concepts when they

construct the map. They will integrate new ideas with older concepts quickly and also can evaluate new information.

In this chapter, the goal is to construct a concept map to provide an easy and clear way to explore the concepts of nanoscience for teachers/students, and to illustrate the connection to the grand challenges of engineering. Teachers can find useful resources, lesson plans and hands-on activities in the concept maps.

5.3 Grand Challenges For Engineering

In the 20th century, engineering recorded its grandest accomplishments. The widespread development and distribution of electricity and clean water, automobiles and airplanes, antibiotics and medical imaging, and computers and the Internet are just some of the highlights from a century in which engineering revolutionized and improved virtually every aspect of human life. The National Academy of Engineering (NAE) coordinated the efforts to determine which engineering achievements of the 20th century had the greatest positive effect on mankind.

NAE sought leading thinkers with a wide range of expertise and experience and constituted the Grand Challenges for Engineering committee that brought together a diverse group of people dedicated to improving quality of life around the globe. The committee's task was to identify a select few grand challenges for engineering --- problems and opportunities --- facing those born at the dawn of this new century. The Challenges were announced in 2008 and these examples merely scratch the surface of the challenges that engineers will face in the 21st century. The problems described here merely illustrate the magnitude and complexity of the tasks ahead. The fourteen identified as the grand challenges for the 21st century are:

1. Make solar energy economical
2. Provide energy from fusion
3. Provide access to clean water

4. Reverse-engineer the brain
5. Advance personalized learning
6. Develop carbon sequestration methods
7. Engineer the tools of scientific discovery
8. Restore and improve urban infrastructure
9. Advance health informatics
10. Prevent nuclear terror
11. Engineer better medicines
12. Enhance virtual reality
13. Manage the nitrogen cycle
14. Secure cyberspace

To address these challenges awareness, commitment, and involvement of the research enterprise, graduate and undergraduate education as well as the K12 community will be required. To help achieve the goal of reaching out to the secondary and post-secondary segments of the educational pipeline, this chapter will focus on few topics to develop a representative teaching curriculum. Using these topics as examples, nanoscience concept maps will be constructed and are integrated with the notion of grand challenges for the 21st century. Among fourteen topics, solar energy, clean water, urban infrastructure, and better medicine are chosen as examples to construct concept maps.

5.4 Big Ideas In Nanoscale Science And Engineering

Every scientific domain has some foundational core concepts, which are referred to as “big ideas”. These core concepts help us understand the field, explain relevant phenomena, and connect the field to ideas from other disciplines.

The big ideas of nanoscience are cross-disciplinary and here is a list of key concepts in nanoscale science and engineering from Stevens et al. [Stevens, S. Y., Sutherland, L., Schank, P., & Krajcik, J. (2007). <http://hice.org/projects/nano/index.html>]

1. Size & Scale
2. Surface to volume ratio
3. Size-dependent properties
4. Dominant forces
5. Particulate nature of matter
6. Quantum phenomena
7. Self-assembly
8. Tools and characterization
9. Modeling and simulations
10. Societal impact

These big ideas will be used to construct concept maps, and the connection between the grand challenges and nano science will be made.

5.5 Construct grand challenges concept map

As mentioned in section 5.4, four areas were chosen from fourteen topics of grand challenges to construct map because a) there are plenty of research papers that are fairly understandable for the non-expert and b) the underlying concepts are quite relevant to the curriculum in grade 7-14.

These topics are:

1. Solar energy
2. Clean water
3. Better medicine
4. Urban infrastructure

From the ten big ideas listed above, the following six important concepts were chosen:

1. Size dependent properties

2. Self assembly
3. Surface dominate behavior
4. Size and scale
5. Surface to volume ratio
6. Force and interaction

The next step is to make connection between the grand challenges and big ideas of nanoscale science and engineering (Fig. 5-3).

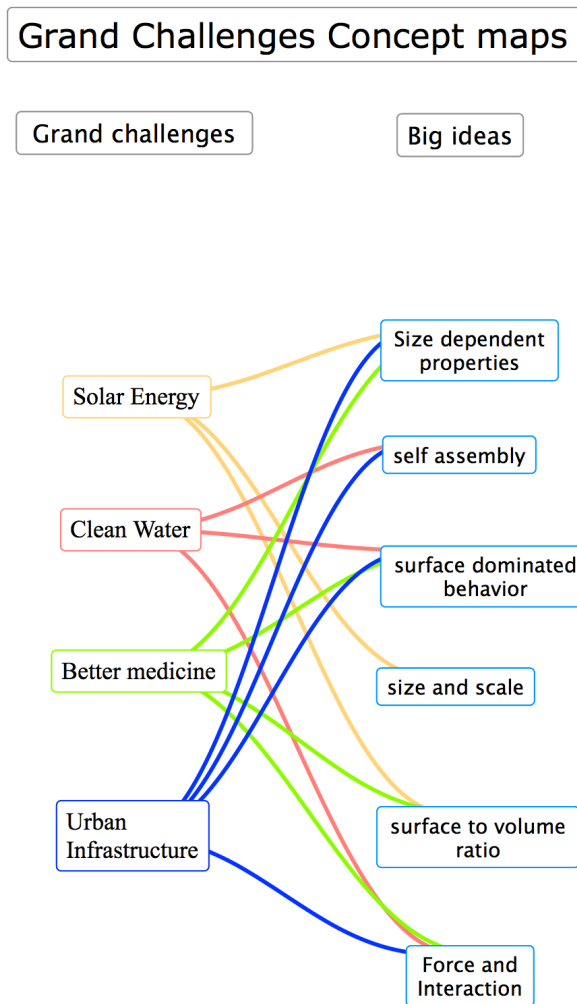


Figure 5-3 Concept map connection between grand challenges and big ideas.

The four selected grand challenges are then connected to different big ideas of nanoscale science. Nanotechnology research papers related to these 4 areas were collected to support the idea of nanotechnology as an enabling technology to address the grand challenges. In order to build up a database and useful resource, several nano-enabled research papers, which are related to the areas of grand challenges are gathered. If learners or teachers are interested in the current research from this area, they could quickly follow the citations in listed papers and conduct further literature search to identify other cutting edge research. (Figure 5-4)

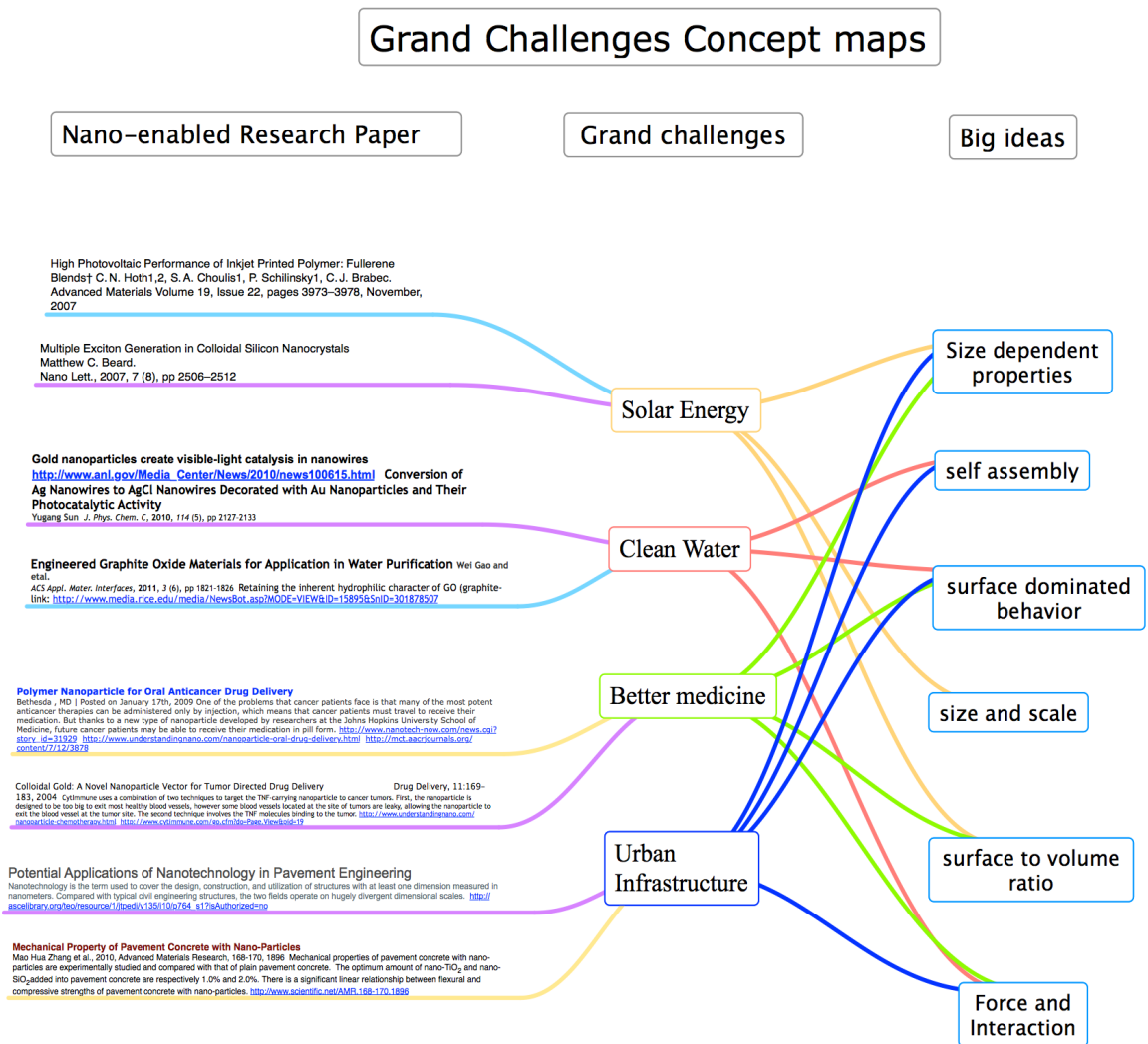


Figure 5-4 Grand Challenge Nano Concept Maps

Here, solar energy is used as an illustrative case. There are many big ideas underlying the development of economical solar energy. For example, if one wanted to develop an efficient solar cell, he had to use appropriate systems that absorb a significant fraction of the sunlight. He can also exploit the different sizes of particles as they have different properties, especially in the nanoscale. In addition, a high surface area would be advantageous. Therefore, the concept of size dependent properties, size & scale, and surface to volume ratio are important.

It can start from an idea of photovoltaic solar cells, and then at the next level different systems can be added, such as single crystal silicon and dye-sensitized cell. Following are some of the ideas, topics, and systems that are collected to place in this map:

1. The techniques needed to make solar cells
2. The advantages and drawback of these techniques
3. Issues and challenges with energy conversion
4. Conventional sources of energy
5. Alternative energy

Figure 5-5 is the mind map of solar energy.

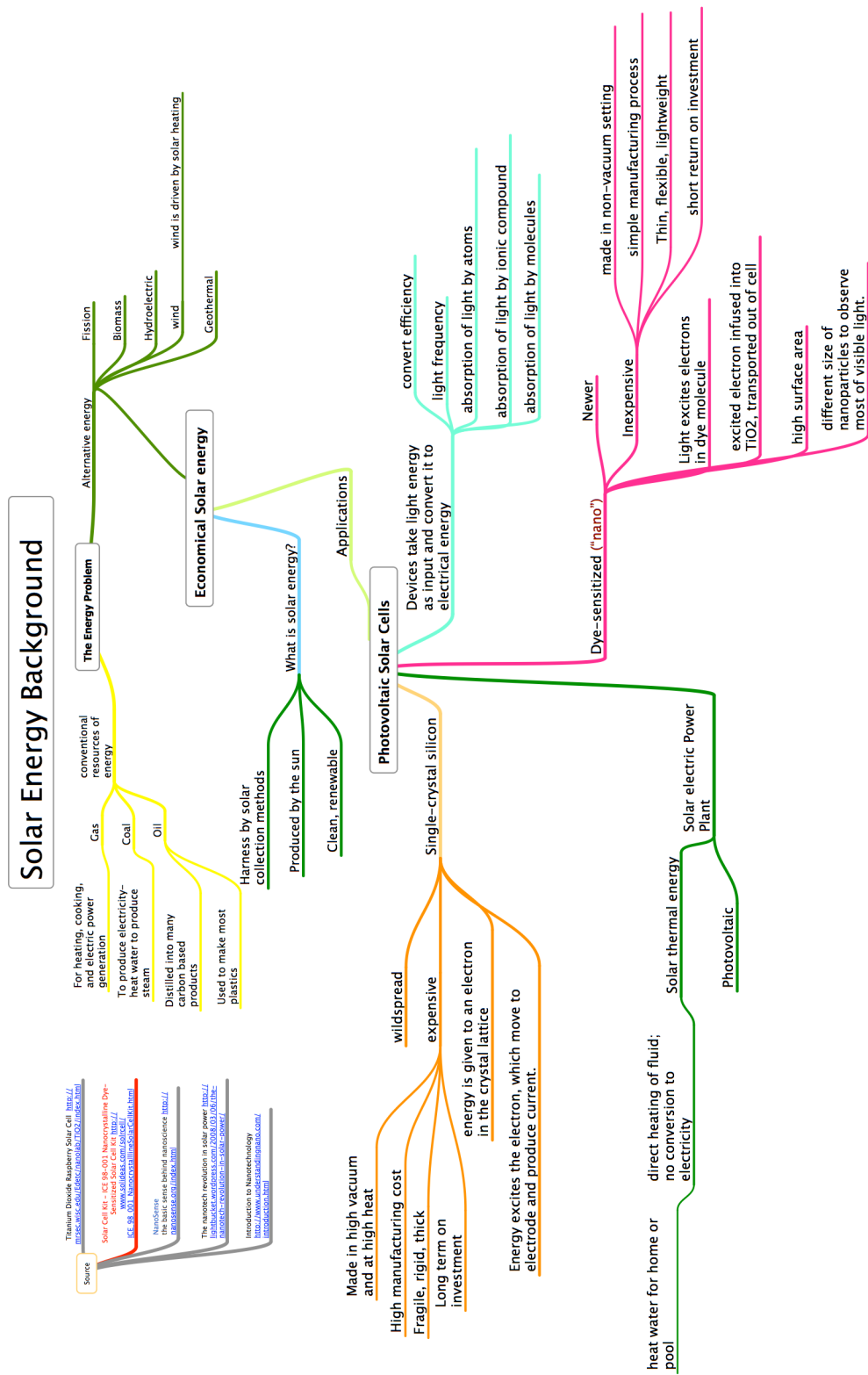


Figure 5-5 Solar energy mind map

Using the same procedure, one also can create another concept map for the background of clean water.

Here are some of the ideas and topics that could be included:

1. The issues contributing to the water crisis
2. The properties of water
3. Quality of water
4. The methods to filter water

Figure 5-6 is the mind map of clean water.

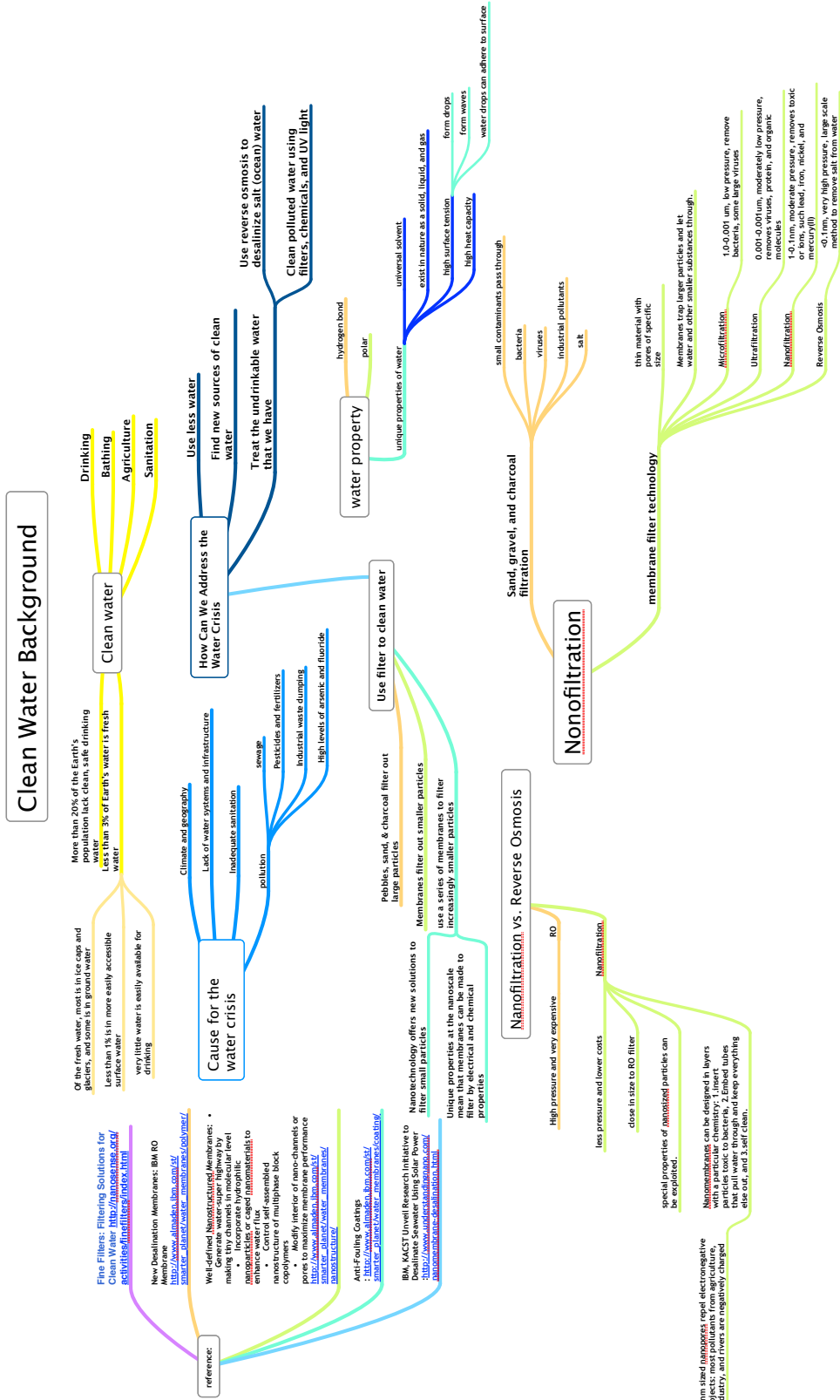


Figure 5-6 Clean water mind map

The next step is to add more information to these maps to enrich their content and make them valuable tools for teachers and learners. Many hands-on activities and teaching materials from textbooks, Internet, previous publications and our own work were collected. The idea is to provide as many resources as we can on this map for the users, so that they can get appropriate teaching and learning materials in short time. Behind each activity, there will be at least one nano concept to teach. For example, the main idea of nano solution activity is to illustrate the idea of “nano” or “one billionth”, through decreasing concentrations of a solution. This activity is also connected to one of the big ideas on the concept map, which is size and scale.

5.6 New Interface For Users To Retrieve Content From Maps

From the Figure 5-7, there are lots of information, such as ideas, concepts, and connecting lines in this map. It is difficult for a user to translate this abundance of information and retrieve valuable knowledge from such a map. Therefore, it is better to have a good interface for users to navigate, especially one has little knowledge of nano science, but wants to use this tool to learn and get useful information quickly.

Such a user-friendly interface, which is a free web-based concept map tool, is available from Spicynodes (<http://www.spicynodes.org/>). It organizes information in a logical way and let visitors quickly drill down to the information they seek. It is easy to author to construct interactive site map, and it is also a fresh way to display information for various creative and educational uses.

Figure 5-8 shows one screenshot of the interactive concept map that we have constructed with Spicynodes.

<http://www.spicynodes.org/a/e01717e9a8c248ed930e6208c50c28c0>

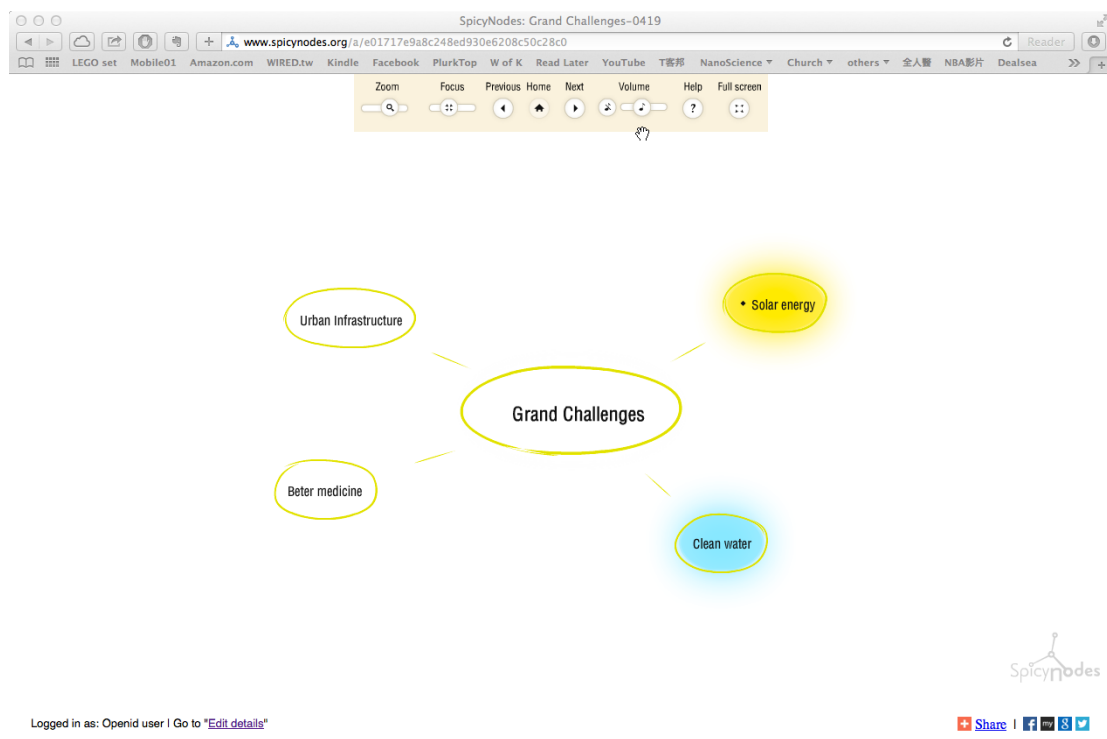


Figure 5-8 The home interface of Grand Challenges, including four areas: Solar energy, Clean water, Better medicine, and Urban infrastructure.

5.7 Two Ways To Use Grand Challenge Nano Concept Map

In this section, two different scenarios for teachers to use the resources from this map will be introduced.

1. Starting from concept guideline relevant to grade 7-14:

One can design a lesson of surface tension, which is an important concept from the curriculum. It also relates to one or more concepts of nano science. In figure 5-9 shows the road map for such a strategy.

First, explore the mentioned activities related to the concept of surface tension, namely (1) molecular self-assembly, (2) subcellular self-assembly, (3) Lego self-assembly activity, and (4) bubbles self-assembly. All these activities have the same central idea: self-assembly, which is one of the important big ideas of nanoscience. Based on the concept map, there are three grand challenges - solar energy, clean water, and urban infrastructure, which are connected to the concept of self-assembly. If a teacher is interested in clean water, the figure provides an example of a research paper that can be provided to students to increase their motivation by connecting to cutting edge research.

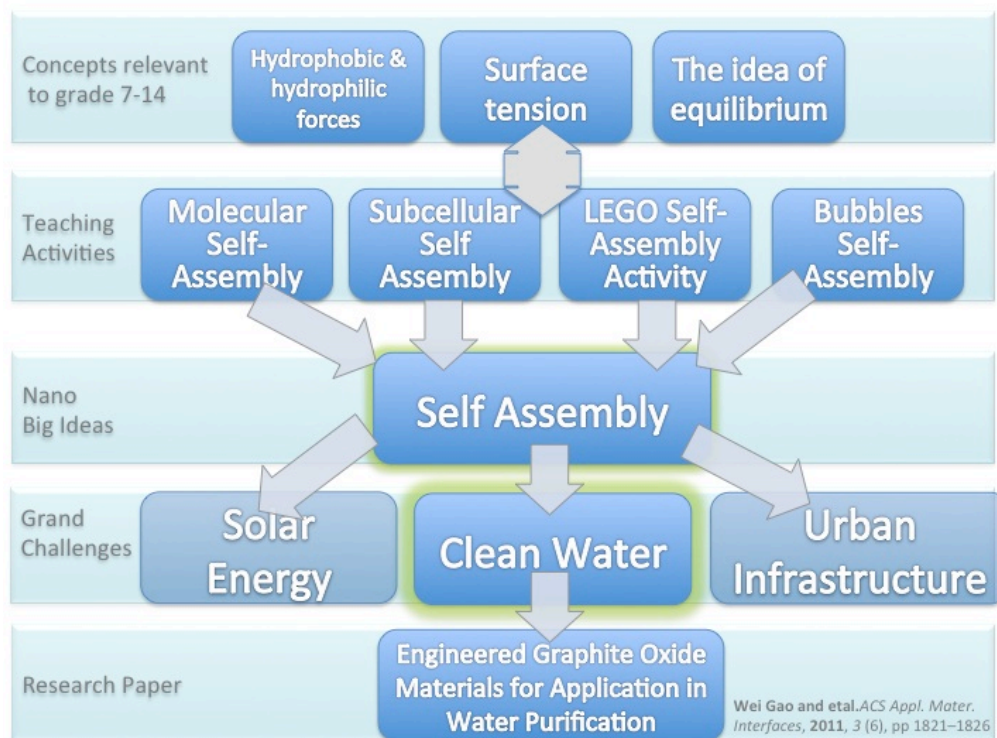


Figure 5-9 Starting from concepts to grand challenges and interested research paper.

2. Starting from interested research paper and current study in the lab

If one finds out few interested articles related to the grand challenges, then he can choose one main area of grand challenges to focus on. Here solar energy was used as an example. From solar energy there are three different nano big ideas: (1) size dependent properties, (2) size and scale, and (3) surface to volume ratio. From these three big ideas, he can choose one idea to expand it and start to design lesson. After expanding the activities from the size and scale, he can find out eight different hands-on experiments. Here shows only four of them: (1) scale of objects, (2) cutting it down to nano, (3) serial dilution lab, and (4) nano sugar. All of these activities have the same concepts relevant to grade 7-14 for teacher to follow the teaching standard and guideline, which is structure-properties correlation and measurement. Figure 5-10 shows the road map for this strategy.

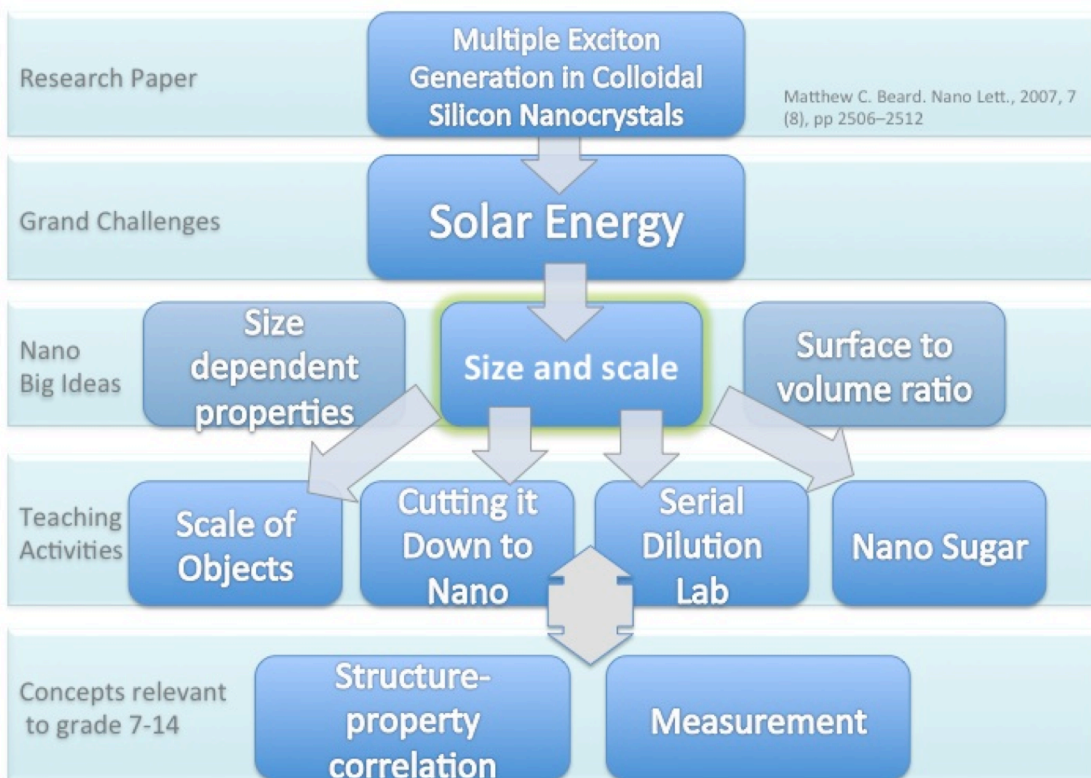


Figure 5-10 Starting from interested research paper to teaching activities.

5.8 Conclusion

In this chapter the theoretical foundations of concept maps was discussed, and the practical way to construct and how to use these concept maps were also presented. In the beginning one may think concept maps are another kind of graphic representation of information. But after understanding the original concept of this tool will lead the user to find out this is truly a powerful tool. Concept mapping has been shown to help students learn, teachers to better design lessons, and researchers create new knowledge. A grand challenges concept map was also demonstrated, which includes nano big ideas and teaching activities. Teachers can use this tool to design lessons, and inspire students to think of the new solution for the grand challenges.

REFERENCES

1. Round, F., R. Crawford, and D. Mann, *The Diatoms*. Cambridge University Press, Cambridge, UK 1990.
2. Kroeger, N. and N. Poulsen, *Diatoms—From Cell Wall Biogenesis to Nanotechnology*. Annual Review of Genetics, 2008. **42**: p. 83-107.
3. Theriot, E.C., *Diatoms*, in *eLS*. 2001, John Wiley & Sons, Ltd.
4. Mann, D.G. and S.J.M. Droop, *Biodiversity, biogeography and conservation of diatoms*. Hydrobiologia, 1996. **336**(1-3): p. 19-32.
5. Umemura, K., et al., *Controlled nanoporous structures of a marine diatom*. Journal of Nanoscience and Nanotechnology, 2007. **7**(8): p. 2842-6.
6. Werner, D., *The Biology of Diatoms*. 1977: University of California Press.
7. Sánchez Mirón, A., et al., *Comparative evaluation of compact photobioreactors for large-scale monoculture of microalgae*. Journal of Biotechnology, 1999. **70**(1-3): p. 249-270.
8. Hildebrand, M., *Diatoms, biomineralization processes, and genomics*. Chem Rev, 2008. **108**(11): p. 4855-74.
9. Frigeri, L.G., et al., *Identification of Proteins from a Cell Wall Fraction of the Diatom Thalassiosira pseudonana : Insights into Silica Structure Formation*. Molecular & Cellular Proteomics, 2006. **5**(1): p. 182-193.
10. Gordon, R., et al., *The Glass Menagerie: diatoms for novel applications in nanotechnology*. Trends in Biotechnology, 2009. **27**(2): p. 116-127.
11. Bozarth, A., U.G. Maier, and S. Zauner, *Diatoms in biotechnology: modern tools and applications*. Applied Microbiology and Biotechnology, 2009. **82**(2): p. 195-201.
12. Wee, K.M., et al., *Engineering and medical applications of diatoms*. Journal of Nanoscience and Nanotechnology, 2005. **5**(1): p. 88-91.
13. Kroeger, N. and N. Poulsen, *Diatoms-From Cell Wall Biogenesis to Nanotechnology*, in *Annual Review of Genetics*. 2008. p. 83-107.

14. Round, F., R. Crawford, and D. Mann, *The Diatoms*. 1990, Cambridge, UK: Cambridge University Press.
15. Losic, D., et al., *Pore architecture of diatom frustules: potential nanostructured membranes for molecular and particle separations*. *Journal of Nanoscience and Nanotechnology*, 2006. **6**(4): p. 982-9.
16. Losic, D., et al., *Rapid fabrication of micro- and nanoscale patterns by replica molding from diatom biosilica*. *Advanced Functional Materials*, 2007. **17**(14): p. 2439-2446.
17. Aldersey-Williams, H., *Towards biomimetic architecture*. *Nat Mater*, 2004. **3**(5): p. 277-9.
18. Hamm, C.E., et al., *Architecture and material properties of diatom shells provide effective mechanical protection*. *Nature*, 2003. **421**(6925): p. 841-843.
19. Almqvist, N., et al., *Micromechanical and structural properties of a pennate diatom investigated by atomic force microscopy*. *J Microsc*, 2001. **202**(Pt 3): p. 518-32.
20. Losic, D., et al., *AFM nanoindentations of diatom biosilica surfaces*. *Langmuir*, 2007. **23**(9): p. 5014-21.
21. *Elastic Properties and Young Modulus for some Materials*. Available from: http://www.engineeringtoolbox.com/young-modulus-d_417.html.
22. Vanierland, E.T. and L. Peperzak, *SEPARATION OF MARINE SESTON AND DENSITY DETERMINATION OF MARINE DIATOMS BY DENSITY GRADIENT CENTRIFUGATION*. *Journal of Plankton Research*, 1984. **6**(1): p. 29-44.
23. Lettieri, S., et al., *The gas-detection properties of light-emitting diatoms*. *Advanced Functional Materials*, 2008. **18**(8): p. 1257-1264.
24. Chauton, M., et al., *Titanium uptake and incorporation into silica nanostructures by the diatom *Pinnularia* sp. (Bacillariophyceae)*. *Journal of Applied Phycology*, 2014: p. 1-10.
25. Zhang, D.Y., et al., *Separation of diatom valves and girdle bands from *Coscinodiscus* diatomite by settling method*. *Journal of Materials Science*, 2010. **45**(21): p. 5736-5741.
26. Morse, D.E., *Silicon biotechnology: harnessing biological silica production to construct new materials*. *Trends in Biotechnology*, 1999. **17**(6): p. 230-232.

27. Parkinson, J. and R. Gordon, *Beyond micromachining: the potential of diatoms*. Trends in Biotechnology, 1999. **17**(5): p. 190-196.
28. Bothara, M., et al., *Nanomonitors: electrical immunoassays for protein biomarker profiling*. Nanomedicine (Lond), 2008. **3**(4): p. 423-36.
29. Biocompare-Manual, *C-Reactive Protein ELISA Kits From Helica Biosystems, Inc.*, 2008.
30. Gale, D.K., et al., *Photoluminescence Detection of Biomolecules by Antibody-Functionalized Diatom Biosilica*. Advanced Functional Materials, 2009. **19**(6): p. 926-933.
31. De Stefano, L., et al., *Marine diatoms as optical biosensors*. Biosensors & Bioelectronics, 2009. **24**(6): p. 1580-1584.
32. De Stefano, L., et al., *Interfacing the nanostructured biosilica microshells of the marine diatom *Coscinodiscus wailesii* with biological matter*. Acta Biomaterialia, 2008. **4**(1): p. 126-130.
33. Rusling, J.F., G. Sotzing, and F. Papadimitrakopoulou, *Designing nanomaterial-enhanced electrochemical immunosensors for cancer biomarker proteins*. Bioelectrochemistry, 2009. **76**(1-2): p. 189-194.
34. Gordon, R., *The Chemical Basis for Diatom Morphogenesis - Instabilities in Diffusion-Limited Amorphous Precipitation Generate Space Filling Branch Patterns*. Federation Proceedings, 1981. **40**(3): p. 827.
35. Soler-Illia, G.J., et al., *Chemical strategies to design textured materials: from microporous and mesoporous oxides to nanonetworks and hierarchical structures*. Chem Rev, 2002. **102**(11): p. 4093-138.
36. Payne, E.K., et al., *Sacrificial biological templates for the formation of nanostructured metallic microshells*. Angewandte Chemie-International Edition, 2005. **44**(32): p. 5064-5067.
37. Rosi, N.L. and C.A. Mirkin, *Nanostructures in biodiagnostics*. Chemical Reviews, 2005. **105**(4): p. 1547-1562.
38. Haes, A.J. and R.P. Van Duyne, *A unified view of propagating and localized surface plasmon resonance biosensors*. Analytical and Bioanalytical Chemistry, 2004. **379**(7-8): p. 920-930.
39. Bolotin, K.I., et al., *Metal-nanoparticle single-electron transistors fabricated using electromigration*. Applied Physics Letters, 2004. **84**(16): p. 3154-3156.

40. Rosei, F., *Nanostructured surfaces: challenges and frontiers in nanotechnology*. Journal of Physics: Condensed Matter, 2004. **16**(17): p. S1373.
41. Losic, D., J.G. Mitchell, and N.H. Voelcker, *Fabrication of gold nanostructures by templating from porous diatom frustules*. New Journal of Chemistry, 2006. **30**(6): p. 908-914.
42. Rorrer, G.L., et al., *Biosynthesis of silicon-germanium oxide nanocomposites by the marine diatom Nitzschia frustulum*. Journal of Nanoscience and Nanotechnology, 2005. **5**(1): p. 41-49.
43. Gaborski, T.R., et al., *High-Performance Separation of Nanoparticles with Ultrathin Porous Nanocrystalline Silicon Membranes*. ACS Nano, 2010. **4**(11): p. 6973-6981.
44. Adhangale, P. and D. Keffer, *Single-file motion of polyatomic molecules in one-dimensional nanoporous materials*. Molecular Physics, 2002. **100**(16): p. 2727-33.
45. Uram, J.D., et al., *Label-free affinity assays by rapid detection of immune complexes in submicrometer pores*. Angewandte Chemie-International Edition, 2006. **45**(14): p. 2281-2285.
46. Snyder, J.L., et al., *An experimental and theoretical analysis of molecular separations by diffusion through ultrathin nanoporous membranes*. Journal of Membrane Science, 2011. **369**(1-2): p. 119-129.
47. Kim, M.J., et al., *Rapid fabrication of uniformly sized nanopores and nanopore arrays for parallel DNA analysis*. Advanced Materials, 2006. **18**(23): p. 3149-+.
48. Gatimu, E.N., J.V. Sweedler, and P.W. Bohn, *Nanofluidics and the role of nanocapillary array membranes in mass-limited chemical analysis*. Analyst, 2006. **131**(6): p. 705-709.
49. Wanunu, M., et al., *Rapid electronic detection of probe-specific microRNAs using thin nanopore sensors*. Nature Nanotechnology, 2010. **5**(11): p. 807-814.
50. Garaj, S., et al., *Graphene as a subnanometre trans-electrode membrane*. Nature, 2010. **467**(7312): p. 190-U73.
51. Evenou, F., et al., *Micro-patterned porous substrates for cell-based assays*. Lab Chip, 2012. **12**(9): p. 1717-22.

52. Agrawal, A.A., et al., *Porous nanocrystalline silicon membranes as highly permeable and molecularly thin substrates for cell culture*. *Biomaterials*, 2010. **31**(20): p. 5408-5417.
53. Sammet, B., C. Steinkuhler, and N. Sewald, *Antibody-drug conjugates in tumor therapy*. *Pharm Pat Anal*, 2012. **1**(1): p. 65-73.
54. Bothara, M., et al., *Nanomonitors: electrical immunoassays for protein biomarker profiling*. *Nanomedicine*, 2008. **3**(4): p. 423-436.
55. Sotiropoulou, S., et al., *Biotemplated nanostructured materials*. *Chemistry of Materials*, 2008. **20**(3): p. 821-834.
56. Cao, Y.W.C., R.C. Jin, and C.A. Mirkin, *Nanoparticles with Raman spectroscopic fingerprints for DNA and RNA detection*. *Science*, 2002. **297**(5586): p. 1536-1540.
57. Hurst, S.J., et al., *Multisegmented one-dimensional nanorods prepared by hard-template synthetic methods*. *Angewandte Chemie-International Edition*, 2006. **45**(17): p. 2672-2692.
58. Striemer, C.C., et al., *Charge- and size-based separation of macromolecules using ultrathin silicon membranes*. *Nature Letters*, 2007. **445**: p. 749-753.
59. Ward, R.K., et al., *Evaluation of tissue culture insert membrane compatibility in the fluorescein leakage assay*. *Toxicology in Vitro*, 1997. **11**(6): p. 761-768.
60. Takoh, K., et al., *Localized chemical stimulation of cellular micropatterns using a porous membrane-based culture substrate*. *Sensors and Actuators B-Chemical*, 2005. **108**(1-2): p. 683-687.
61. Li, J.L., et al., *Electrical characterization of protein molecules by a solid-state nanopore*. *Applied Physics Letters*, 2007. **91**(5).
62. Rant, U., et al., *Electrically Facilitated Translocations of Proteins through Silicon Nitride Nanopores: Conjoint and Competitive Action of Diffusion, Electrophoresis, and Electroosmosis*. *Nano Letters*, 2010. **10**(6): p. 2162-2167.
63. Yusko, E.C., et al., *Controlling protein translocation through nanopores with bio-inspired fluid walls*. *Nature Nanotechnology*, 2011. **6**(4): p. 253-260.
64. Xie, P., et al., *Local electrical potential detection of DNA by nanowire-nanopore sensors*. *Nature Nanotechnology*, 2012. **7**(2): p. 119-125.

65. Venkatesan, B.M. and R. Bashir, *Nanopore sensors for nucleic acid analysis*. Nature Nanotechnology, 2011. **6**(10): p. 615-624.
66. Ivanov, A.P., et al., *DNA Tunneling Detector Embedded in a Nanopore*. Nano Letters, 2011. **11**(1): p. 279-285.
67. Wanunu, M., J. Sutin, and A. Meller, *DNA Profiling Using Solid-State Nanopores: Detection of DNA-Binding Molecules*. Nano Letters, 2009. **9**(10): p. 3498-3502.
68. Lo, C.J., T. Aref, and A. Bezryadin, *Fabrication of symmetric sub-5 nm nanopores using focused ion and electron beams*. Nanotechnology, 2006. **17**(13): p. 3264-7.
69. Tong, H.D., et al., *Silicon nitride nanosieve membrane*. Nano Letters, 2004. **4**(2): p. 283-287.
70. Darain, F., et al., *Development of an immunosensor for the detection of vitellogenin using impedance spectroscopy*. Biosensors & Bioelectronics, 2004. **19**(10): p. 1245-1252.
71. Hahm, J. and C.M. Lieber, *Direct ultrasensitive electrical detection of DNA and DNA sequence variations using nanowire nanosensors*. Nano Letters, 2004. **4**(1): p. 51-54.
72. Nam, J.M., C.S. Thaxton, and C.A. Mirkin, *Nanoparticle-based bio-bar codes for the ultrasensitive detection of proteins*. Science, 2003. **301**(5641): p. 1884-1886.
73. Niwa, O., M. Morita, and H. Tabei, *Electrochemical-Behavior of Reversible Redox Species at Interdigitated Array Electrodes with Different Geometries - Consideration of Redox Cycling and Collection Efficiency*. Analytical Chemistry, 1990. **62**(5): p. 447-452.
74. Abeloff, M.D., et al., *Clinical Oncology*. 2nd ed. 2000, New York: Churchill Livingstone.
75. Chou, S.F., et al., *Development of an immunosensor for human ferritin, a nonspecific tumor marker, based on surface plasmon resonance*. Biosensors & Bioelectronics, 2004. **19**(9): p. 999-1005.
76. Danesh, J., et al., *Association of fibrinogen, C-reactive protein, albumin, or leukocyte count with coronary heart disease - Meta-analyses of prospective studies*. Jama-Journal of the American Medical Association, 1998. **279**(18): p. 1477-1482.

77. Biocompare-Manual. *C-Reactive Protein ELISA Kits From Helica Biosystems, Inc.* 2008; Available from: <http://www.biocompare.com/review/1106/C-Reactive-Protein-ELISA-Kits-From-Helica-Biosystems-Inc.html>.
78. Suni, I.I., *Impedance methods for electrochemical sensors using nanomaterials.* *Trac-Trends in Analytical Chemistry*, 2008. **27**(7): p. 604-611.
79. Willner, I., A.N. Shipway, and B. Willner, *Layered nanoparticle architectures on surfaces for sensing and electronic functions.* *Molecules as Components of Electronic Devices*, 2003. **844**: p. 88-105.
80. Zheng, G.F., F. Patolsky, and C.M. Lieber, *Multiplexed electrical detection of cancer marker proteins and single viruses by nanowire fet arrays.* *Abstracts of Papers of the American Chemical Society*, 2005. **229**: p. U782-U782.
81. Takhistov, P., *Electrochemical synthesis and impedance characterization of nano-patterned biosensor substrate.* *Biosensors and Bioelectronics*, 2004. **19**(11): p. 1445-1456.
82. Popat, K.C., et al., *Surface modification of nanoporous alumina surfaces with poly(ethylene glycol).* *Langmuir*, 2004. **20**(19): p. 8035-8041.
83. Benesi, H.A. and B.H.C. Winquist, *Surface Acidity of Solid Catalysts*, in *Advances in Catalysis*. 1978, Academic Press. p. 97-182.
84. Townley, H.E., A.R. Parker, and H. White-Cooper, *Exploitation of diatom frustules for nanotechnology: tethering active biomolecules.* *Advanced Functional Materials*, 2008. **18**(2): p. 369-374.
85. Baldus, S., et al., *Myeloperoxidase serum levels predict risk in patients with acute coronary syndromes.* *Circulation*, 2003. **108**(12): p. 1440-1445.
86. Mach, F., et al., *C-reactive protein as a marker for acute coronary syndromes*, 1997. p. 1897-1902.
87. Reddy, R.K., et al., *Nanomonitor: Protein biosensors for rapid analyte analysis.* *Ieee Sensors Journal*, 2008. **8**(5-6): p. 720-723.
88. Yang, W.S., et al., *Direct electrical detection of antigen-antibody binding on diamond and silicon substrates using electrical impedance spectroscopy.* *Analyst*, 2007. **132**(4): p. 296-306.
89. Desilva, M.S., et al., *Impedance Based Sensing of the Specific Binding Reaction between Staphylococcus Enterotoxin-B and Its Antibody on an Ultra-Thin Platinum Film.* *Biosensors & Bioelectronics*, 1995. **10**(8): p. 675-682.

90. Katz, E. and I. Willner, *Probing biomolecular interactions at conductive and semiconductive surfaces by impedance spectroscopy: Routes to impedimetric immunosensors, DNA-Sensors, and enzyme biosensors*. *Electroanalysis*, 2003. **15**(11): p. 913-947.
91. Pei, R.J., et al., *Amplification of antigen-antibody interactions based on biotin labeled protein-streptavidin network complex using impedance spectroscopy*. *Biosensors & Bioelectronics*, 2001. **16**(6): p. 355-361.
92. Gomez, R., et al., *Microfluidic Biochip for Impedance Spectroscopy of Biological Species*. *Biomedical Microdevices*, 2001. **3**: p. 201-209.
93. Lasseter, T.L., W. Cai, and R.J. Hamers, *Frequency-dependent electrical detection of protein binding events*. *Analyst*, 2004. **129**(1): p. 3-8.
94. Gabay, C. and I. Kushner, *Acute-Phase Proteins and Other Systemic Responses to Inflammation*. *New England Journal of Medicine*, 1999. **340**(6): p. 448-454.
95. Balamurugan, S., et al., *Surface immobilization methods for aptamer diagnostic applications*. *Analytical and Bioanalytical Chemistry*, 2008. **390**(4): p. 1009-1021.
96. Riepl, M., et al., *Optimization of capacitive affinity sensors: drift suppression and signal amplification*. *Analytica Chimica Acta*, 1999. **392**(1): p. 77-84.
97. Krishnamoorthy, S. and M. Himmelhaus, *Confinement-induced enhancement of antigen-antibody interactions within binary nanopatterns to achieve higher efficiency of on-chip immunosensors*. *Advanced Materials*, 2008. **20**(14): p. 2782-2788.
98. Daiguji, H., et al., *Electrochemomechanical Energy Conversion in Nanofluidic Channels*. *Nano Letters*, 2004. **4**(12): p. 2315-2321.
99. Keshishian, H., et al., *Quantification of Cardiovascular Biomarkers in Patient Plasma by Targeted Mass Spectrometry and Stable Isotope Dilution*. *Molecular & Cellular Proteomics*, 2009. **8**(10): p. 2339-2349.
100. Bao, Z.H., et al., *Chemical reduction of three-dimensional silica micro-assemblies into microporous silicon replicas*. *Nature*, 2007. **446**(7132): p. 172-175.
101. Hurst, S.J., et al., *Multisegmented one-dimensional nanorods prepared by hard-template synthetic methods*. *Angew Chem Int Ed Engl*, 2006. **45**(17): p. 2672-92.

102. Liao, H. and J.H. Hafner, *Gold Nanorod Bioconjugates*. Chemistry of Materials, 2005. **17**(18): p. 4636-4641.
103. Geddes, C.D. and J.R. Lakowicz, *Metal-enhanced fluorescence*. Journal of Fluorescence, 2002. **12**(2): p. 121-129.
104. Zin, M.T., et al., *Surface-plasmon-enhanced fluorescence from periodic quantum dot arrays through distance control using biomolecular linkers*. Nanotechnology, 2009. **20**(1).
105. Bruchez, M., et al., *Semiconductor nanocrystals as fluorescent biological labels*. Science, 1998. **281**(5385): p. 2013-2016.
106. Esteve-Turrillas, F.A. and A. Abad-Fuentes, *Applications of quantum dots as probes in immunosensing of small-sized analytes*. Biosensors & Bioelectronics, 2013. **41**: p. 12-29.
107. Zhang, Y.X., A. Dragan, and C.D. Geddes, *Metal-enhanced fluorescence from tin nanostructured surfaces*. Journal of Applied Physics, 2010. **107**(2).
108. Pompa, P.P., et al., *Fluorescence enhancement in colloidal semiconductor nanocrystals by metallic nanopatterns*. Sensors and Actuators B-Chemical, 2007. **126**(1): p. 187-192.
109. Levi, S.A., et al., *Fluorescence of dyes adsorbed on highly organized, nanostructured gold surfaces*. Chemistry-a European Journal, 2002. **8**(16): p. 3808-3814.
110. Aslan, K., et al., *Metal-enhanced fluorescence: an emerging tool in biotechnology*. Current Opinion in Biotechnology, 2005. **16**(1): p. 55-62.
111. Zhang, L., et al., *Large Enhancement of Quantum Dot Fluorescence by Highly Scalable Nanoporous Gold*. Advanced Materials, 2014. **26**(8): p. 1289-1294.
112. Hung, Y.J., et al., *Fluorescence enhancement by surface gratings*. Optics Express, 2006. **14**(22): p. 10825-10830.
113. Goldys, E.M., et al., *Fluorescence amplification by electrochemically deposited silver nanowires with fractal architecture*. Journal of the American Chemical Society, 2007. **129**(40): p. 12117-12122.
114. Zhou, L.C., et al., *Enhancement of Immunoassay's Fluorescence and Detection Sensitivity Using Three-Dimensional Plasmonic Nano-Antenna-Dots Array*. Analytical Chemistry, 2012. **84**(10): p. 4489-4495.

115. Li, X., Y. He, and L. Que, *Fluorescence Detection and Imaging of Biomolecules Using the Micropatterned Nanostructured Aluminum Oxide*. Langmuir, 2013. **29**(7): p. 2439-2445.
116. Matsui, S. and Y. Ochiai, *Focused ion beam applications to solid state devices*. Nanotechnology, 1996. **7**(3): p. 247-258.
117. Xia, Y.N., et al., *Replica molding using polymeric materials: A practical step toward nanomanufacturing*. Advanced Materials, 1997. **9**(2): p. 147-149.
118. Srinivasarao, M., *Nano-optics in the biological world: Beetles, butterflies, birds, and moths*. Chemical Reviews, 1999. **99**(7): p. 1935-1961.
119. Weiner, S. and L. Addadi, *Design strategies in mineralized biological materials*. Journal of Materials Chemistry, 1997. **7**(5): p. 689-702.
120. Petrou, P., et al., *Fluorescence enhancement from plasmonic Au templates*. Microelectronic Engineering, 2011. **88**(8): p. 1845-1848.
121. Vlassioug, I., et al., *Versatile ultrathin nanoporous silicon nitride membranes*. Proceedings of the National Academy of Sciences of the United States of America, 2009. **106**(50): p. 21039-21044.
122. Wilk, S.J., et al., *Teflon (TM)-coated silicon apertures for supported lipid bilayer membranes*. Applied Physics Letters, 2004. **85**(15): p. 3307-3309.
123. Wilk, S.J., et al., *Integrated electrodes on a silicon based ion channel measurement platform*. Biosensors and Bioelectronics, 2007. **23**: p. 183-190.
124. Wang, W., et al., *Self-Assembly of Nanostructured Diatom Microshells into Patterned Arrays Assisted by Polyelectrolyte Multilayer Deposition and Inkjet Printing*. Journal of the American Chemical Society, 2009. **131**(12): p. 4178-+.
125. Fukushima, T., et al., *Multichip-to-Wafer Three-Dimensional Integration Technology Using Chip Self-Assembly With Excimer Lamp Irradiation*. Ieee Transactions on Electron Devices, 2012. **59**(11): p. 2956-2963.
126. Deblois, R.W., C.P. Bean, and R.K.A. Wesley, *Electrokinetic Measurements with Submicron Particles and Pores by Resistive Pulse Technique*. Journal of Colloid and Interface Science, 1977. **61**(2): p. 323-335.
127. Escobedo, C., *On-chip nanohole array based sensing: a review*. Lab on a Chip, 2013. **13**(13): p. 2445-2463.

128. C., v.R., *Nano and micro engineered membrane technology*. . 2004: Amsterdam: Elsevier.
129. Siegel, R., et al., *The Impact of Eliminating Socioeconomic and Racial Disparities on Premature Cancer Deaths*. *Ca-a Cancer Journal for Clinicians*, 2011. **61**(4): p. 212-236.
130. Yang, W., P.J. Lopez, and G. Rosengarten, *Diatoms: self assembled silica nanostructures, and templates for bio/chemical sensors and biomimetic membranes*. *Analyst*, 2011. **136**(1): p. 42-53.
131. Bhatta, H., J. Enderlein, and G. Rosengarten, *Fluorescence correlation spectroscopy to study diffusion through diatom nanopores*. *J Nanosci Nanotechnol*, 2009. **9**(11): p. 6760-6.
132. Novak, J.D., *Learning How to Learn*. 1984: Cambridge University Press.
133. Clara Barroso, R.C. *CONCEPT MAPS: TOOLS FOR UNDERSTANDING COMPLEX PROBLEMS*. in *Proc. of the Third Int. Conference on Concept Mapping*. 2008. Tallinn, Estonia & Helsinki, Finland
134. T. Y. Chen, T.C.H., S. J. Su, P. Y. Hsieh, J. F. Lin, M. L. Chung, *The effect of concept map and teaching aid on the learning achievements of students having different background in teaching white-light interferometry*, in *Annual International Conference on Education & e-Learning (EeL)2011*.
135. Cañas, J.D.N.A.J., *The Theory Underlying Concept Maps and How to Construct Them*, in *Technical Report IHMC CmapTools 2006*, Florida Institute for Human and Machine Cognition.
136. Alberto J. Cañas, M.C.a.M.A. *Mining the Web to Suggest Concepts during Concept Mapping: Preliminary Results*. in *XIII Simpósio Brasileiro de Informática na Educação*. 2002.